ABC Effect and d^* Resonance in Double-Pionic Fusion to ^{3}He

DISSERTATION

der Mathematisch-Naturwissenschaftlichen Fakultät

der Eberhard Karls Universität Tübingen

zur Erlangung des Grades eines

Doktors der Naturwissenschaften

(*Dr. rer. nat.*)

vorgelegt von

Elena Pérez del Río

aus Guadalajara (Spanien)

Tübingen

2014

Tag der mündlichen Qualifikation:	28.05.2014
Dekan:	Prof. Dr. Wolfgang Rosenstiel
1. Berichterstatter:	Prof. Dr. Heinz Clement
2. Berichterstatter:	Prof. Dr. Gerhard J. Wagner

Kurzfassung

Der ABC-Effekt bezeichnet eine ausgeprägte Überhöhung bei niedrigen Massen im Spektrum der invarianten Masse zweier Pionen, die in der doppelt-pionischen Fusion zu einem gebundenen nuklearen System erzeugt wurden. Kürzlich wurde erkannt, dass dieser Effekt mit einer Resonanzstruktur in der Energieabhängigkeit des totalen Wirkungsquerschnitts derartiger Fusionsprozesse korreliert ist. Untersuchungen der doppelt-pionischen Fusion zu Deuterium und ^{4}He mit kinematisch kompletten Hochstatistik-Messungen waren ausschlaggebend für das neue Verständnis des ABC Effekts, der ein Puzzle für mehr als ein halbes Jahrhundert darstellte.

In dieser Arbeit wird die doppelt-pionische Fusion zu ^{3}He untersucht, also die historisch erste Reaktion, in der der ABC-Effekt beobachtet wurde. Erstmals wird nun diese Reaktion durch exklusive und kinematisch komplette Experimente über den gesamten Energiebereich vermessen, in dem dieser Effekt auftritt. Um die Energieabhängigkeit des Wirkungsquerschnitts zu untersuchen, wurde die Reaktion $pd \rightarrow {}^3\mathrm{He}\pi^0\pi^0$ mit dem WASA-Detektor an COSY unter zwei kinematisch unterschiedlichen Bedingungen untersucht: zum einem mit pd-Kollisionen bei einer Protonenstrahlenergie von $T_p = 1.0$ GeV und zum anderen mit einer Messung der quasifreien Reaktion $dd \rightarrow {}^3\mathrm{He}\pi^0\pi^0(n_{spect})$ bei einer Deuteronstrahlenergie von $T_d = 1.7$ GeV.

Ähnlich wie bei früheren Messungen in der fundamentalen Fusionsreaktion $pn \rightarrow d\pi^0\pi^0$ sowie der Reaktion $dd \rightarrow {}^4\mathrm{He}\pi^0\pi^0$ wird auch hier eine resonanzartige Energieabhängigkeit des totalen Wirkungsquerschnitts beobachtet. Der ABC-Effekt ist auch hier mit der Anregung einer Resonanz d^* in pn- und $\Delta\Delta$-Systemen verbunden. Diese Resonanz wird im Fall von ^{3}He bei einer Masse von $M_{d^*}({}^3\mathrm{He}) \approx 2.37$ GeV mit einer effektiven Breite von $\Gamma_{d^*}({}^3\mathrm{He}) = 85$ MeV beobachtet. Das ABC-Resonanzmodell, das diese dibaryonische Resonanz beinhaltet, beschreibt erfolgreich die in dieser Arbeit erhaltenen Daten.

Während der Experimente wurde auch ein in Tübingen entwickelter DIRC-Detektor getestet, der als Prototyp für das zukünftige PANDA-Experiemt an FAIR dient.

Abstract

The ABC effect denotes a pronounced low-mass enhancement in the invariant mass spectrum of two pions generated in double-pionic fusion processes to bound nuclear systems. Recently it has been found to be correlated to a resonance structure in the energy dependence of the total cross section of such processes. Investigations of the double-pionic fusion to deuteron and ^{4}He with kinematically complete high-statistics measurements have been crucial for the understanding the ABC effect, which has been a puzzle for half a century.

The double-pionic fusion to ^{3}He, the first reaction where the ABC effect was observed, has been studied in the present work by exclusive and kinematically complete experiments for the first time over the whole energy region, where the effect takes place. To investigate the energy dependence of the cross section the $pd \to {}^3\mathrm{He}\pi^0\pi^0$ reaction was measured with the WASA detector at COSY under two kinematically different regimes: measurement of single-energy pd collisions at a proton beam energy of $T_p = 1.0$ GeV and measurement of the quasi-free $dd \to {}^3\mathrm{He}\pi^0\pi^0(n_{spect})$ reaction at a deuteron beam energy of $T_d = 1.7$ GeV.

Similar to the observations in the basic $pn \to d\pi^0\pi^0$ reaction and in the $dd \to {}^4\mathrm{He}\pi^0\pi^0$ reaction, a resonance-like energy dependence in the total cross section is observed. The ABC effect is connected to the excitation of a resonance, called d^*, in pn and $\Delta\Delta$ systems. The resonance is observed, in the ^{3}He case, with a mass of $M_{d^*}(^3\mathrm{He}) \approx 2.37$ GeV and an effective width of $\Gamma_{d^*}(^3\mathrm{He}) = 85$ MeV. The ABC resonance model, which includes this dibaryonic resonance, also describes successfully the present data.

During the experiment also a DIRC detectorwas tested, which was constructed at Tübingen and which served as prototype for the future PANDA experiment at FAIR.

"Didn't you know that manuscripts don't burn?"

(Mikhail Bulgakov, *The master and Margarita*.)

Contents

List of Figures

LIST OF FIGURES

LIST OF FIGURES

List of Tables

LIST OF TABLES

1

Introduction

The Standard Model (SM) of particle physics is able to account for all fundamental particles and their interactions very well . Three fundamental interactions, electromagnetic, weak and strong mediate between the basic constituents of matter: quarks and leptons. These forces are carried by gauge bosons such as the photon in the case of the electromagnetic force or the Z^0 and $W^{\pm}$ for the weak interaction. In the case of the strong interaction the correspondent mediator between the quarks is the gluon and this interaction is described by Quantum-Chromo-Dynamics (QCD). Nuclear matter is made up of strongly interacting hadrons, which are composites of three quarks (qqq), called baryons, or pairs of quark and anti-quark ($q\bar{q}$), called mesons.

QCD is proven to be successful in making predictions at high energies, where quarks and gluons can be treated as quasi-free particles (partons). However, in the low-energy regime, where the quarks bind together, QCD becomes non-perturbative due to quark confinement and the theory fails to find analytical solutions. Hadron physics becomes then a very useful tool to help to understand low-energy QCD, e.g. studying non-ordinary compositions of quarks. Mesonic molecules, pentaquarks and dibaryons are examples of such exotic particles.

The case of dibaryons, particles made up of six quarks, is a peculiar ones. These exotic baryonic species have been searched since many decades. They were proposed back in 1964 by F. J. Dyson and N. Xuong, Ref. [1], and later on, in 1977, by R. L. Jaffe, who suggested the existence of a strange six-quark particle called H-dibaryon, made of two Λ-hyperons, Ref. [2]. Jaffe's suggestion initiated a world-wide rush for dibaryons - both experimentally and theoretically. In 1989, T. Goldman and others proposed the

existence of a non-strange dibaryon, the so called "inevitable dibaryon", as a bound state of two Δs with quantum numbers $I(J^P) = 0(3^+)$ or $3(0^+)$, Ref. [3]. The possibility of finding one of these exotic particles has motivated many searches in the past and again in the recent years due to new theoretical calculations, see Refs. [4, 5, 6, 7, 8].

From the experimental side, one of the most remarkable causes for the recent interest in the exotic dibaryons has been the new experimental results for a long-time puzzle, the ABC effect (Ref. [9]), a low-mass enhancement observed in the invariant mass of the $\pi\pi$ system in the $pd \to {}^3\mathrm{He}\pi^0\pi^0$ reaction. Originally discovered in 1960, it remained without explanation for more than 50 years until recently.

Experiments on double-pionic fusion, more specifically the study of the basic fusion reaction $pn \to d\pi^0\pi^0$, Ref. [10], revealed that the ABC was related to the excitation of a resonance, called d^*. The studies of the discovered resonance in the pn system continued within our group by studying the reaction channel $pn \to pn\pi^0\pi^0$ and in particular pn elastic scattering. These investigations have been further completed by also analyzing other possible decay channels of the resonance, see e.g. Ref. [11].

The present work considers the reaction $pd \to {}^3\mathrm{He}\pi^0\pi^0$ under two different kinematic regimes: direct production in pd collisions at a proton beam energy of $T_p = 1.0$ GeV and quasi-free production via $dd \to {}^3\mathrm{He}\pi^0\pi^0(n_{spect})$ at a deuteron beam energy $T_d = 1.7$ GeV.

Additionally, within the scope of this thesis, a DIRC (Detection of Internally Reflected Cherenkov light) detector prototype for the WASA experiment was built and tested. The planned upgrade was motivated by the possibility of increasing the energy resolution of WASA as well as to test the DIRC performance for the future PANDA experiment at the Facility for Antiproton and Ion Research (FAIR).

The structure of the thesis is as follows: in the next chapter the ABC effect is explained following a historical review from its discovery in 1960 to the present experiments carried out with the WASA detector. Chapter 3 describes the WASA detector setup and the COSY facility, where the data for this work was taken. The construction and tests of the DIRC prototype will be covered in Chapter 4. Chapters 5 and 6 deal with the experimental conditions, calibration of the detector and analysis of the reaction. In Chapter 7 the results are presented, together with the model used to understand them. Finally, a chapter with a summary and outlook, as well as the Appendixes with additional information complete this work.

2

The ABC Effect Revisited

2.1 ABC Effect

The ABC effect was discovered in 1960 by Alexander Abashian, Norman E. Booth and Kenneth M. Crowe, Ref. [9], when they measured the inclusive ^{3}He spectra for the reaction $pd \to {}^3\mathrm{He} + X$ with a single arm magnetic spectrometer.

The measurement was done at Berkeley with a proton beam and a deuteron gas target at four different proton energies (624 MeV, 648 MeV, 695 MeV and 743 MeV). They recorded the ^{3}He ions at a single polar angle of 17°, being able to reconstruct the system X from the measured momentum of the ^{3}He.

The reconstructed invariant mass spectra of the system X showed an unexpected enhancement close to the threshold for two-pion production, which was seen at all four beam energies at roughly the same position. The result of this experiment, for one of the measured energies, is shown in Fig. 2.1. In addition to this four energies, three years latter, the authors published a new measurement at $T_p = 750$ MeV, adding a new angle (13.5°) which showed the same phenomenon. Lacking a physics interpretation, the effect was then named after the initials of the three authors.

In the following years other laboratories carried out similar experiments: Birmingham in 1969 [12]: $pd \to d(p_{spect}) + X$; Saclay in 1970 [13]: $pd \to d(p_{spect})X$ and $dp \to {}^3\mathrm{He} + X$; Saclay in 1973 [14]: $pd \to {}^3\mathrm{He} + X$; Saclay in 1976 [15]: $dd \to {}^4\mathrm{He}X$; and Saclay in 1978 [16]: $np \to d + X$.

All the previous experiments mentioned above were done in the same energy range,

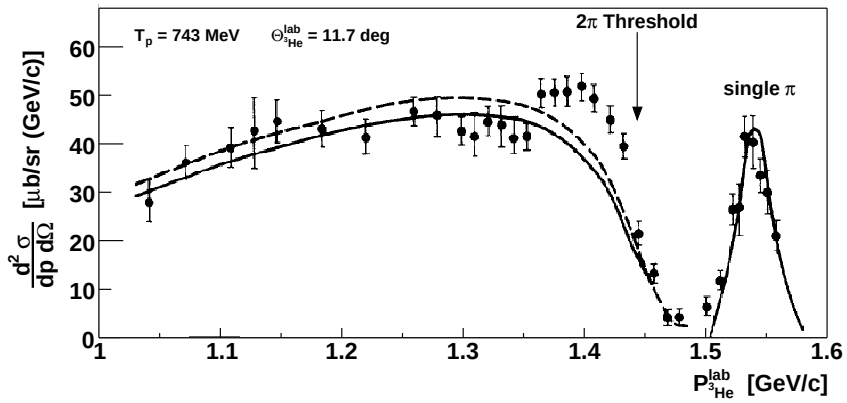

Figure 2.1: Double-differential cross section as a function of the ^{3}He laboratory momentum. First experimental result of the ABC effect for the reaction $pd \rightarrow {}^3\mathrm{He}X$. The solid and dashed lines correspond to phase space expectation with different normalizations. The enhancement, relative to phase space, at about 1.4 GeV/c^2 is the so-called ABC effect. The peak at high momentum corresponds to single pion production. From Ref. [9]

150-400 MeV above the $\pi\pi$ threshold in the center of mass system[1]. They all correspond to single-arm spectrometer measurements, where only the heavy recoil particle was detected and used to reconstruct the invariant mass of the system X.

The results of all experiments show a similar low-mass enhancement close to $\pi\pi$ threshold when the system X is electrically neutral and isoscalar[2] (I=0), with the nucleons in the outgoing channel being fused.

Trying to explain this effect, the original authors [17] already proposed several possible explanations such as: a new meson state, a final state interaction between the pion and the ^{3}He or a strong $\pi\pi$ interaction. The latter, being the most plausible one, lead them to derive the S-wave $\pi\pi$ scattering length from a fit to the data, resulting in a value of $a_{I=0} = 2.5$ fm, which is an order of magnitude larger than the result from other experiments ($a_{I=0} = 0.2$ fm, Ref. [18, 19, 20, 21]).

A decade later, after the first experiment carried out at Berkeley, an alternative explanation was proposed. The two participating nucleons would be excited to their first excited state, the Δ resonance as a cause for the ABC effect [22]. This process is

[1] In the following the center of mass will be abbreviated as c.m.

[2] an isoscalar state is a singlet state with total isospin and the isospin z-projection equal zero, $I_{\pi\pi} = 0$ and $I_z = 0$

depicted in the Fig. 2.2.

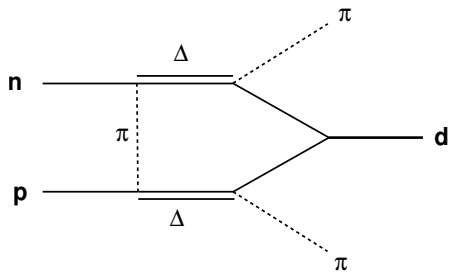

Figure 2.2: Feynman diagram for the ΔΔ t-channel process for the basic reaction $pn \to d\pi\pi$.

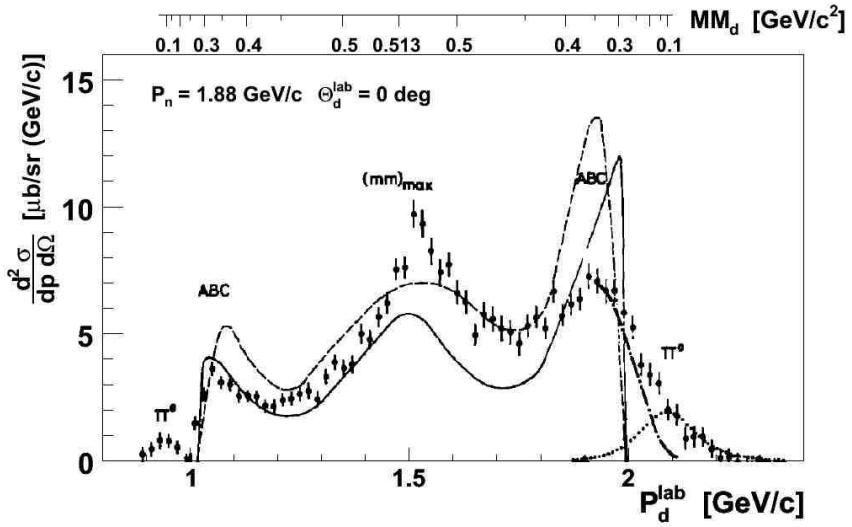

Figure 2.3: Experimental result for the momentum of the deuteron in laboratory frame for the reaction $np \to dX$ (points) compared to two calculations of the t-channel ΔΔ model. The scale on top represents the translation of the momentum into missing mass of the deuteron (equivalent to invariant mass of the system X). Figure taken from Ref. [16]

In their calculation in [22], Risser and Shuster showed that in the case of a final state with bound nucleons the excitation of two Δs leads to maxima in the invariant mass distribution of the $\pi\pi$-system of the reaction for two preferred configurations of the $\pi\pi$ system:

- Pions are emitted in parallel (low relative momentum of the two Δs) and thus, an enhancement at low $M_{\pi\pi}$ will be present.

- Pions are emitted anti-parallel (high relative momentum of the Δs) leading to an enhancement at high $M_{\pi\pi}$.

According to this, for c.m. energies $\sqrt{s}$ below the $\Delta\Delta$ mass , the low-mass enhancement is preferred, above this value, the high-mass enhancement becomes prominent and at $\sqrt{s} \approx 2M_{\Delta}$ both peaks should be equivalent. In terms of the momentum of the heavy recoil particle, three peaks are present. Two peaks at low and high momentum, which correspond to low masses of the $\pi\pi$ system, when the heavy particle is scattered in forward or backward direction in the c.m. system (large and small momentum correspondingly); and a third peak at intermediate values of the momentum corresponding to high $\pi\pi$ masses. This is seen in Fig. 2.3.

Up to this point in the history of the ABC effect most experiments were inclusive measurements, only the heavy nuclear recoil particle was detected and the system X was reconstructed. This, as noted in Ref. [23], implies that also other particles might contribute to the enhancement at high invariant masses of the $\pi\pi$ system (middle peak of the deuteron in Fig. 2.3), particularly 3π or η production could be included. In 1999 [24] and 2000 [25] two exclusive measurements were conducted, however they were performed far below the ABC region.

To clarify the situation, in 2005 CELSIUS/WASA carried out a new kinematically complete, exclusive measurement, [26]. The experiment recorded the reaction $pd \rightarrow {}^3\mathrm{He}\pi\pi$ identifying both, $\pi^0\pi^0$ and $\pi^+\pi^-$ channels. That way the ABC effect in ^{3}He double-pionic fusion was, for the first time, measured exclusively by fully identifying the isoscalar pion pair.

The measurement was performed with a proton beam with a kinetic energy[3] of 0.895 GeV. The result provided a surprise in the history of the ABC effect: The high mass enhancement observed in the system X of the inclusive measurements did not result from $\pi\pi$ production; the ABC effect corresponds only to the observed enhancement at low $\pi\pi$ masses, and thus, the t-channel $\Delta\Delta$ model proposed by Risser and Shuster [22] could no longer explain the effect.

In Fig. 2.4 the invariant mass of the $\pi^0\pi^0$ system obtained from the exclusive measurement of the reaction $pd \rightarrow {}^3\mathrm{He}\pi^0\pi^0$ is shown. Only the enhancement at low invariant masses is observed. As a possible explanation, Ref. [26] suggested that the Δs may

[3] At this energy the ABC effect was expected to be at maximum

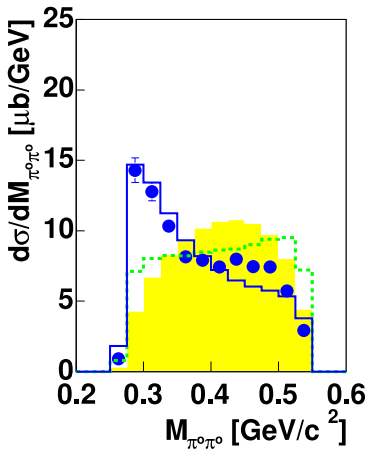

Figure 2.4: Invariant mass of the produced $\pi^0\pi^0$-pair measured with CELSIUS/WASA in the reaction $pd \rightarrow {}^3\mathrm{He}\pi^0\pi^0$ at $T_p = 0.895$ GeV. The yellow area represents the phase space expectation. The blue solid line corresponds to a model calculation and the dashed green line to the t-channel $\Delta\Delta$ process. The data points exhibit a clear low mass enhancement [26].

form a quasi-bound system. This would suppress the configurations with high relative momentum of the Δs and, thus, the high-mass enhancement in the invariant mass of the $\pi\pi$ system.

2.2 ABC Resonance: the d^* Resonance

Such an unexpected result motivated further experiments on the nature of the ABC effect by investigating the basic fusion reaction to the deuteron. The experiments for this reaction where done over the entire kinematic region where the ABC effect was expected, first with CELSIUS/WASA in Uppsala and more recently with higher statistics, with WASA-at-COSY [10, 27], at Jülich.

In both experiments the invariant mass spectrum of the $\pi\pi$ system exhibited, like it was seen previously, only the low-mass enhancement, instead of the double hump structure expected from the conventional $\Delta\Delta$ excitation process. In addition, the total cross section in dependence of the c.m. energy was measured.

In the 2008 experiment, the fusion reaction $pd \rightarrow d\pi^0\pi^0 + (p_{spect})$ was measured at three different energies of the proton beam (T_p =1.0, 1.2 and 1.4 GeV). The nucleons

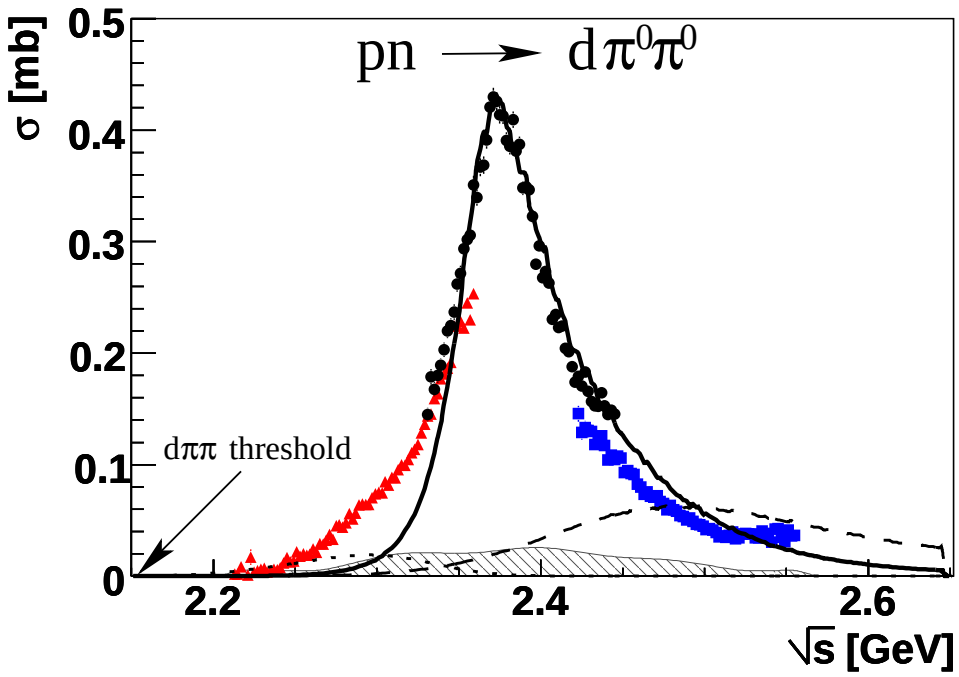

Figure 2.5: Total cross section vs $\sqrt{s}$ for the basic fusion process $pd \to d\pi^0\pi^0 + (p_{spect})$ for the beam energies $T_p = 1.0$ GeV (red triangles), 1.2 GeV (black dots), and 1.4 GeV (blue squares) normalized independently. The hatched area indicates systematic uncertainties. The drawn lines represent the expected cross sections for the Roper ($N^*(1440)$) excitation process (dotted) and the t-channel $\Delta\Delta$ contribution (dashed) as well as a calculation for a s-channel resonance (solid). From Ref. [10]

within the deuteron are not at rest but experience a motion described by a Fermi distribution. Because of the effect of this Fermi motion, the quasi-free kinematics imply not a single beam energy but an effective range, due to the smearing of the beam energy according to the Fermi momentum of the nucleon involved in the collision. Hence, the quasi-free kinematics allowed to explore a wide range of c.m. energies.

In Fig. 2.5 the total cross section in dependence of $\sqrt{s}$ is shown as obtained by the experiment carried out with WASA-at-COSY, Ref. [10]. The striking result from this study is the resonance structure observed in the total cross section. This resonance structure, called d^* in the following, has a mass of 2.37 GeV, about 80 MeV lower than $2m_\Delta$, and a width of approximately 70 MeV. These values are in conflict with those from the conventional $\Delta\Delta$ excitation (dashed line in the plot) and $\Delta\Delta$-FSI assumptions, see Ref. [26].

Moreover, from the study of the whole kinematic region a connection between this resonance d^* and the ABC effect in $M_{\pi\pi}$ was established, see Fig. 2.6. At low c.m. energies just above threshold, the $M_{\pi\pi}$ distribution develops as expected according to phase space distribution. As the resonance d^* gets more and more excited, the ABC effect, the low-mass enhancement in $M_{\pi\pi}$, starts to become more apparent until it reaches the maximum just at the peak of the resonance structure, fading away as the resonance structure decreases and the energies approach the t-channel $\Delta\Delta$ region, see Fig. 2.6.

This structure is consistent with the formation of an unconventional intermediate s-channel resonance, which decays into two Δs [Fig. 2.7]. The quantum numbers of the resonance can be established from the final state, which demands total isospin to be zero, and from the angular distributions, resulting in $I(J^p) = 0(3^+)$ [10].

In 2007 [28], another experiment in the context of the ABC investigations was performed with WASA-at-COSY. On this occasion the reaction of interest was the double-pionic fusion to ^{4}He. The reaction $dd \to {}^4\mathrm{He}\pi^0\pi^0$ was measured at nine different deuteron beam energies ($T_d = 0.8, 0.9, 1.0, 1.05, 1.117, 1.2, 1.25, 1.32, 1.4$ GeV) with complete kinematics (i.e. identifying all reaction products) and high statistics. The beam energies were selected to cover the full region where the ABC effect, and thus the resonance d^*, is expected.

Again the ABC effect, which exhibits a narrower and more pronounced enhancement than in the basic $pn \to d\pi^0\pi^0$ case, see Fig. 2.8, is observed to be correlated with the

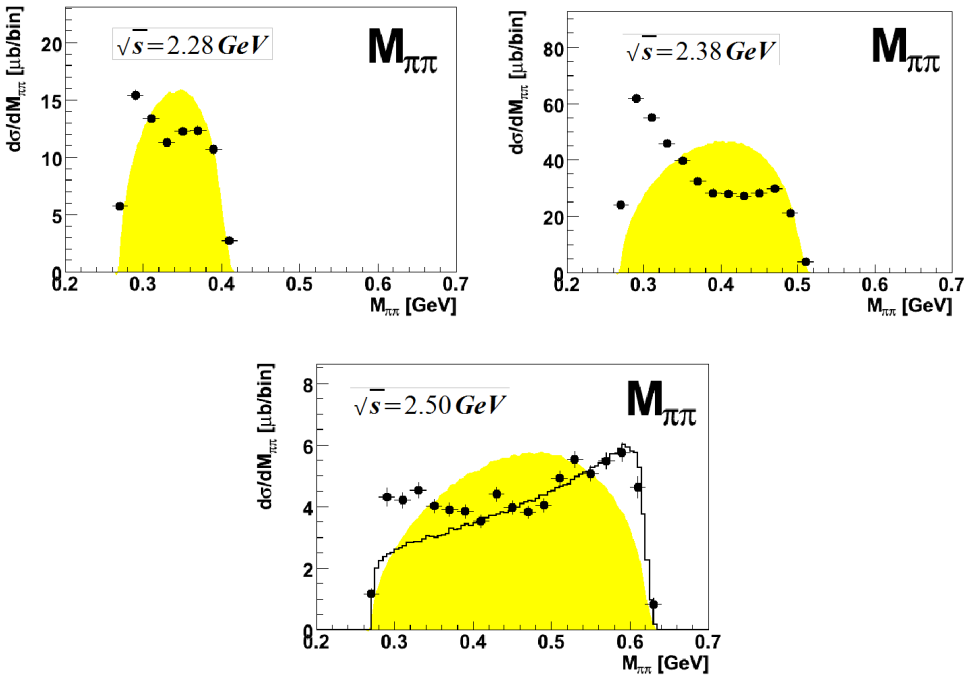

Figure 2.6: Invariant Mass of the $\pi^0\pi^0$-system in dependence with $\sqrt{s}$. **Top left**: $M_{\pi^0\pi^0}$ for $\sqrt{s} = 2.28$ GeV. The data (solid black circles) exhibit a similar behavior to that expected from phase space simulation (yellow area). **Top right**: $M_{\pi^0\pi^0}$ at the maximum of the resonance ($\sqrt{s} = 2.38$ GeV). The ABC effect enhancement at low invariant mass is at maximum. **Bottom**: $M_{\pi^0\pi^0}$ for $\sqrt{s} = 2.50$ GeV. The ABC effect has nearly vanished at this energy and the t-channel $\Delta\Delta$ gets prominent. The solid line corresponds to the t-channel $\Delta\Delta$ calculation.

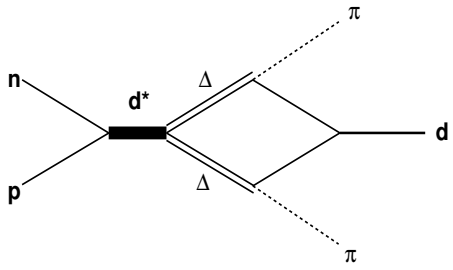

Figure 2.7: Feynman diagram of the ABC resonance model for $pn \to d\pi^0\pi^0$. The d^* intermediate resonance decays into two Δs, which subsequently decay into two pions and two nucleons, which bind to a deuteron.

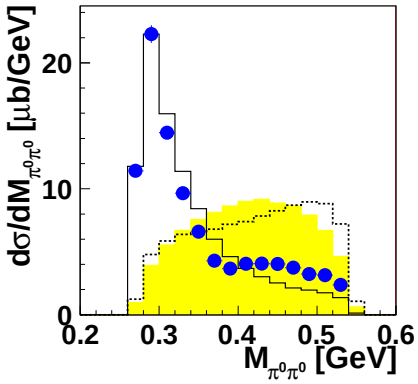

Figure 2.8: Invariant mass of the $\pi^0\pi^0$-system in the $dd \to {}^4\mathrm{He}\pi^0\pi^0$ reaction at $T_d = 1.117$ GeV kinetic energy. The yellow area represents the phase-space distribution. The dotted histogram corresponds to the t-channel $\Delta\Delta$ calculation, whereas the solid histogram represents a calculation of a pn s-channel resonance. From Ref. [28, 29]

appearance of a resonance structure in the total cross section at the same excess energy, however, with an increased width, which might be explained due to Fermi motion in initial and final nuclei as well as due to collision damping [28, 29], see Fig. 2.9.

To summarize, the ABC effect known for more than fifty years is strictly correlated with a narrow resonance structure in the total cross section. For the purely isoscalar $pn \to d\pi^0\pi^0$ reaction this phenomenon is interpreted as a s-channel resonance with $I(J^p) = 0(3^+)$. The same situation is found for the double-pionic fusion to the ^{4}He nuclei, thus this isoscalar pn resonance structure is obviously strong enough to survive even in nuclei.

A dibaryonic nature of the resonance, formed by two Δs bound together, has been suggested. Such dibaryonic states have been proposed in several models, e.g. Ref. [33]. For this reason the d^* nomenclature has been adopted for this ABC resonance, following the notation in Refs. [3, 33], where a resonance with the same quantum numbers was predicted at just about the mass, where the ABC resonance structure is located, see Refs. [34, 35].

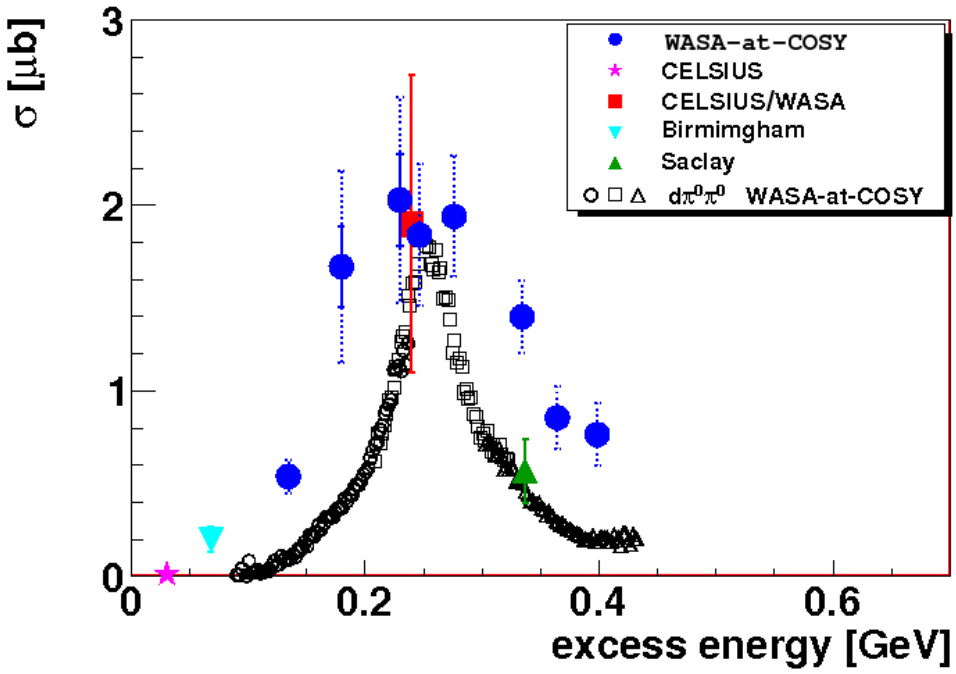

Figure 2.9: Total cross sections of the $pn \to d\pi^0\pi^0$ (black open symbols) and $dd \to {}^4\mathrm{He}\pi^0\pi^0$ reactions (colored solid symbols) in dependence of the excess energy above threshold. The result for the reaction $pn \to d\pi^0\pi^0$ has been scaled down by a factor of 240. The WASA-at-COSY results from Ref. [29] (solid blue circles) are compared to results from a previous exclusive measurement at CELSIUS/WASA [30] (red square) as well as inclusive measurements at CELSIUS [31] (violet star), Birmingham [32] (inverted cyan triangle) and Saclay [15] (green triangle). From Ref. [28, 29]

3

WASA-at-COSY Setup

The WASA-at-COSY setup is a fixed-target experiment to study hadronic interactions, and specifically designed to study rare decays. The experiment has been running at the Cooler Synchrotron (COSY) storage ring at the Jülich Research Center since the installation of the detector in late 2006, after having been moved from the CELSIUS storage ring at the Theodor Svedberg Laboratory in Uppsala, Sweden, were it had being operating before [36].

The WASA (**W**ide **A**ngle **S**hower **A**pparatus) is a detector specially conceived to study the production and decay of light mesons and it is capable to measure all final state particles, including both charged and neutral products [37].

Compared to its previous home, the COSY beam offers higher maximum energies for both, polarized and unpolarized beam, and experiments can be carried out with higher luminosities than in CELSIUS. Because of this, the WASA detector has undergone a series of upgrades that finished with the installation of a new layer (FVH2) in the Forward Detector at the end of 2008.

A brief description of the COSY facility and the detector components of WASA is presented in the following, for reference.

3.1 COSY Storage Ring

The COSY (**CO**oler **SY**nchrotron) is an accelerator and storage ring operated at the IKP (Institute für Kernphysik) at the Forschungszentrum Jülich, which provides polarized and unpolarized protons and deuterons in the momentum range between

0.3 GeV/c and 3.7 GeV/c. The accelerator complex, Fig. 3.1, is composed of an isochronous cyclotron (JULIC), used as injector, a race track shaped ring with 184 m of circumference and internal and external target stations [38, 39]. For unpolarized protons the beam can contain up to 10^{11} particles. This together with the pellet target leads to average luminosities of 10^{-32} cm^{-2}s^{-1}.

COSY is equipped with two different beam cooling systems, electron cooling for proton momenta up to 600 MeV/c and stochastic cooling for high momenta in the range from 1.5 GeV/c to 3.4 GeV/c. These two mechanisms reduce the momentum spread of the beam and increase equilibrium emittance, allowing to store higher beam intensities [40].

The beam delivered by COSY suffers energy losses in each cycle due to the interaction with the internal pellet target. This cannot be compensated by cooling. Thus, to maintain the beam quality, during data taking for WASA-at-COSY, a barrier bucket cavity can be used to keep the energy of the beam constant [41].

3.2 WASA-at-COSY Detector Facility

The WASA-at-COSY Detector is installed in one of the straight sections inside the COSY ring. The system can be subdivided in three main parts: The Pellet Target System, the Central Detector and the Forward Detector, as shown in the cross sectional view of the detector in fig 3.2. In the following, each part will be briefly described.

3.2.1 Coordinate System

To set a reference frame and a common framework to define the detector geometry, a coordinate system with its origin at the interaction point and the Z-axis parallel to the beam direction (horizontal) is defined. The Y-axis runs opposite and parallel to the target stream (vertical) and the X-axis is left with the positive direction defined pointing out of the COSY ring. The polar angle is described as the angle with respect to positive z direction, covering a range $0 \leq \theta \leq \pi$,and the azimuthal angle, ϕ, will be the angle of a vector projection onto the XY plane, with a range $0 \leq \phi \leq 2\pi$, counted from the x-axis in the direction of the y-axis. This is a very convenient geometry, since nearly all detectors are symmetric in ϕ and the x and y components of the beam momentum

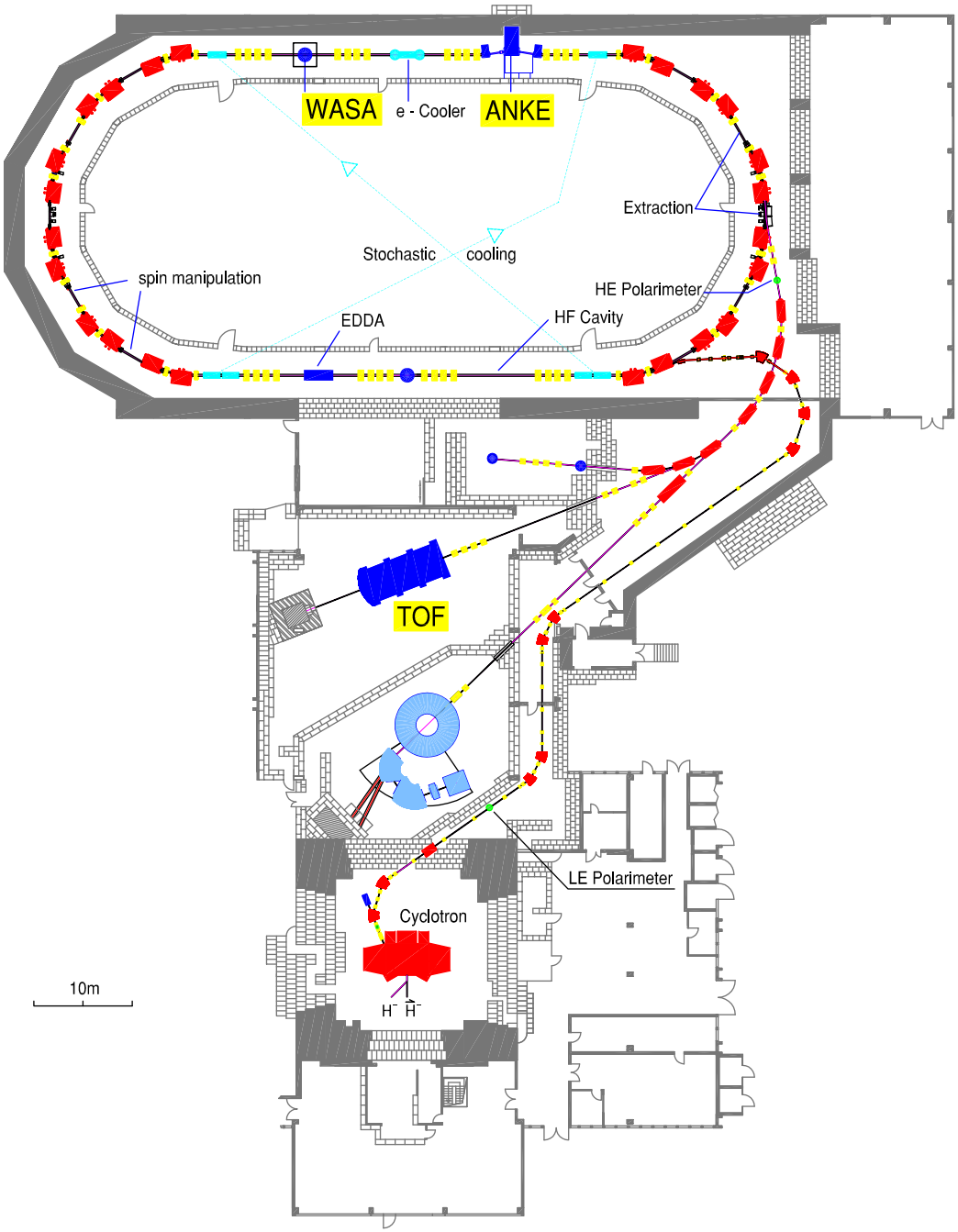

Figure 3.1: Top view of the floor of the COSY ring. From Ref [38].

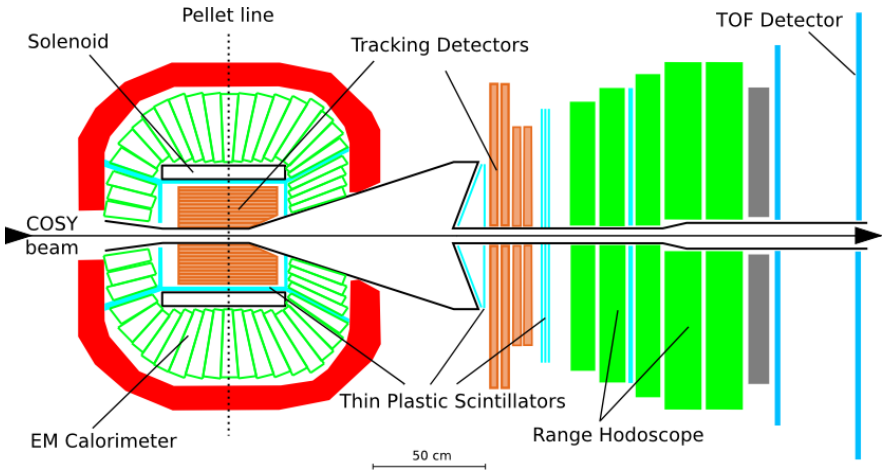

Figure 3.2: Schematic view of the WASA detector setup.

will be zero in the laboratory frame. Fig. 3.3 illustrates the WASA-at-COSY coordinate system.

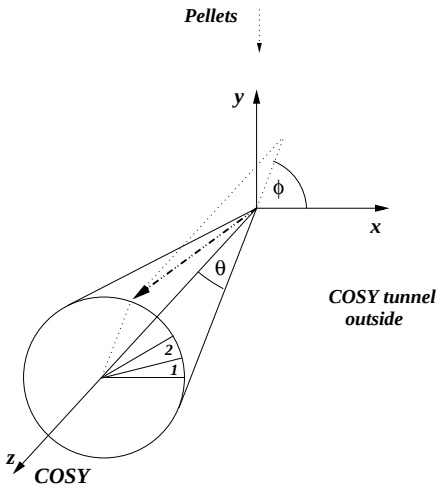

Figure 3.3: WASA coordinate system. The Z-axis.

3.2.2 The Pellet Target

The Pellet Target system used in the WASA experiment was a unique design for the WASA-CELSIUS experiment. It is integrated in the experiment such that a 4π detection around the interaction point is possible.

The main components of the system are shown in Fig. 3.4. The pellet generator delivers a jet of liquid hydrogen or deuterium which is broken up by a vibrating nozzle into equidistant droplets of 20-25 μm diameter. The droplets are frozen by evaporation inside the droplet chamber and form a beam of pellets that is injected into a 7 cm long vacuum injection-capillary. After collimation, the remaining solid droplets pass a 2 m long skimmer with a 1 mm diameter that injects them directly into the scattering chamber. At this stage the pellet stream spread is 3.5 mm [42] in the X-direction. After passing through the beam, pellets are collected in the pellet dump.

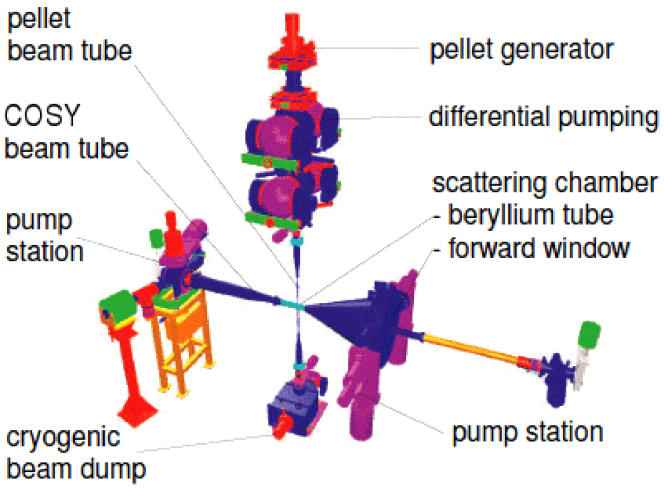

Figure 3.4: Schematic view of the WASA Pellet Target System. From Ref. [43]

The actual performance of the Pellet Target System is summarized in Tab. 3.1. The target thickness of more than 10^{15} atoms/cm^2 gives an acceptable half-life of the circulating beam and luminosities up to $1 \cdot 10^{32}$ cm^{-2}s^{-1}. Further information about the performance can be found in [42, 43].

Pellet diameter(μm)	25-35
Pellet frequency(kHz)	5-12
Pellet-pellet distance(mm)	9-10
Effective target area density(at/cm^2)	$>10^{15}$
Beam diameter(mm)	2-4

Table 3.1: Performance of the Pellet Target System. From Ref. [42]

3.2.3 The Central Detector (CD)

The aim of the central part of WASA is to detect and identify the decay products of mesons created in the reactions. For this purpose a superconducting solenoid to provide a magnetic field for momentum measurements, a tracking detector MDC (Mini Drift Chamber), a thin layer of plastic scintillator PSB (Plastic Scintillator Barrel) and a CsI(Na) calorimeter SEC (Scintillating Electromagnetic Calorimeter) are arranged surrounding the interaction point and covering a solid angle close to 4π rad. These subparts are described in the following subsections starting from the innermost layer to the outside.

Mini Drift Chamber (MDC)

The MDC [44] is the most inner part of the CD. It is a cylindrical drift chamber made of 1738 drift tubes arranged in 17 layers. It measures tracks of charged particles allowing reconstruction of the momentum by curvature in the magnetic field, polar and azimuthal angles. The polar angle coverage of the MDC goes from 24° to 159°. Each tube is made of 25 μm thin mylar coated with aluminum in the inner side and a 20 μm wire of stainless steel. The tubes are filled with a 80%-20% mixture of argon-ethane (C_2H_6). The radius of the tubes increases from 2 mm for the five innermost layers, 3 mm for the following six, to 4 mm for the last six layers. Nine layers are arranged in parallel to the beam axis, while every second layer is skewed by a small angle (6°-9°) in respect to the beam axis, see Fig. 3.5.

Plastic Scintillator Barrel (PS)

The PS [44] is located outside of the MDC and consists of three differentiated parts, a cylindrical main body and two end caps, made of 8 mm thick plastic scintillators. The cylindrical part (PSC), surrounded by the super-conducting solenoid, consists of 50 elements installed in one layer in such a way so the elements overlap on each side by 6 mm with the neighboring bars to prevent particles from escaping unidentified. Two bars on the top and two in the bottom are cut in half to leave space for the pellet tube.

The forward and backward caps (PSF and PSB respectively) close the barrel. The PSF is perpendicular to the z-axis while the PSB has an inclination of 30° in a conical

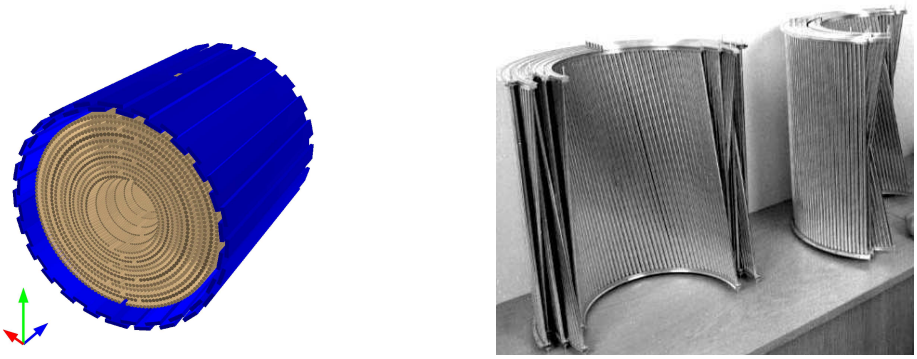

Figure 3.5: Mini Drift Chamber. **Left**: Sketch of the Mini Drift Chambers (MDC). The blue bars represent the PS. The blue arrow shows the beam direction. **Right**: Picture of the Mini Drift Chambers MDC. From Ref. [44]

shape. Each of the end caps is made of 48 cake piece shaped elements aligned to the 48 ϕ sectors form the PSC. Straight elements also overlap at the edges to avoid gaps.

To protect the electronics light-guides couple the bars to the photomultiplier tubes (PMT) located outside the iron yoke. In Fig. 3.6 a sector of the PS with light-guides can be seen.

Together with the MDC and the Calorimeter the Plastic Barrel is used to identify the charged particles by means of ΔE-p and ΔE-E techniques respectively. At trigger level the PS is used to define the number of charge particles in the Central Detector.

Superconducting Solenoid (SCS)

The SCS gives the necessary axial $\vec{B}$ field with a maximum strength of 1.3 T for momentum measurements. The return path of the magnetic flux is achieved by means of a soft iron yoke that also shields the readout electronics and serves as support for the calorimeter crystals. To suppress gamma conversion in the SCS the wall thickness was reduced to 0.18 interaction lengths.

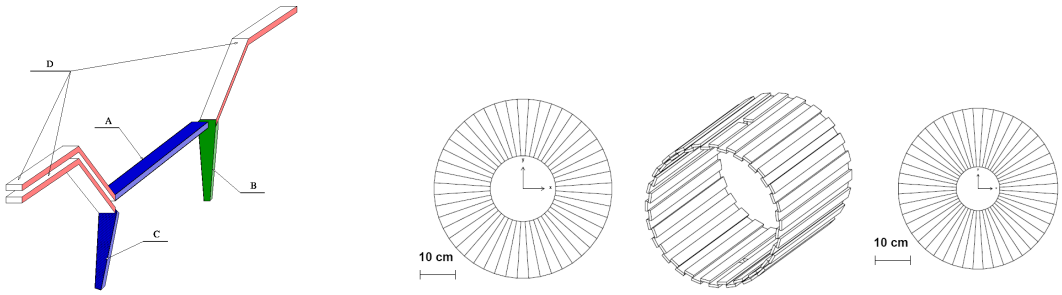

Figure 3.6: Plastic Scintillator Barrel. **Left**: Sketch of one sector of the PS with light-guides. Layout of one section of the PS detector. **A** denotes the rectangular counters of the barrel wall and **B** and **C** are trapezoidal elements in the forward and in the backward caps respectively. **D** are bent light guides. **Right**: Forward(left), center (middle) and backward (right) parts of the Plastic Scintillator Barrel. From Ref. [44]

Scintillating Electromagnetic Calorimeter (SEC)

The most external part of the Central Detector is the SEC. It consists of 1012 CsI crystals doped with Na arranged in 24 rings and serves to reconstruct the energy of photons and charged particles in the CD. The structure is built in three parts with characteristic crystal sizes, fig. 3.7, each one read out by a photomultiplier.

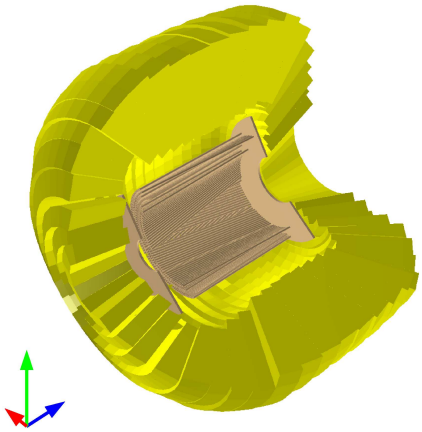

Figure 3.7: Scintillating Electromagnetic Calorimeter. The MDC, PSE, PSC and PSB can be seen placed inside it. The blue arrow shows the beam direction. From Ref. [45].

The SEC covers polar angles from 20° to 169°, which corresponds to 96% of the full

solid angle, with an angular resolution of 5°, both azimuthal and polar angles. It can measure energies up to 800 MeV in case of gammas, e^- and e^+. The energy threshold for gamma detection is as low as 2 MeV. A list of characteristics of the SEC is shown in Tab. 3.2.

Amount of sensitive material	135 g cm^{-2}
radiation lengths	16
nuclear interaction lengths	0.8
geometric coverage (4π)	96%
polar angle	20° - 169°
azimuthal angle	0° - 360°
Maximum stopping kinetic energy	
$\pi^{\pm}$/p/d	190/400/450 MeV
Angular resolution	5°
Time resolution	
photons	40 ns
charged particles	5 ns
Energy resolution	
photons	$\frac{5\%}{\sqrt{E/GeV}}$
charged particles	3%

Table 3.2: SEC list of characteristics. From Ref. [45].

The crystals have a truncated pyramidal shape and are arranged in 24 layers. The layers are split in three sections with 4 crystals in the forward part, 17 in the center and 3 in the backward part. The length of the crystal varies from 30 cm in the central part to 25 cm in the forward and 20 cm in the backward. This corresponds to approximately 16 radiation lengths and 0.8 hadronic interaction lengths. Thus charged particles as well as photons can be measured. The Na doped scintillator has a short decay time. So the SEC delivers fast enough signals to be used on trigger level. A more detailed description can be found in Ref. [45].

3.2.4 The Forward Detector (FD)

For those projectiles scattered in forward direction ($3° \leq \theta \leq 18°$) a series of layers of scintillator and track detectors complete the setup of the WASA detector. This group

of sub-detectors is called Forward Detector (FD) and serves to identify and measure the energy and angles of charged and, to some extent, neutral particles.

As mentioned before, the FD was modified after its installation at COSY and the setup described in the following is the up-to-date configuration used in the present experiment.

The Forward Window Counter (FWC)

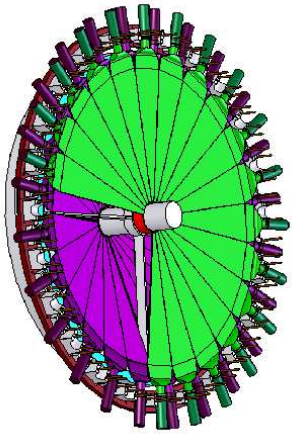

Figure 3.8: Forward Window Counter sketch. The beam axis runs from left to right of the picture. From Ref. [28]

The FWC (Forward Window Counter), Fig. 3.8, is the first detector in down-stream direction. It consists of two layers made of scintillating elements. The first layer is directly positioned at the exit of the vacuum chamber, with an inclination angle of 20° with respect to the xy-plane to be accommodated to the scattering window. The 24 cake-shaped plastic scintillator elements are coupled to the PMTs by adiabatic light guides. The second layer is planar. It is divided in 24 cake-shaped elements which are turned with respect to the first layer by half an element, thus doubling the total granularity of the whole FWC.

A more detailed description can be found in Ref. [28]. The FWC is used in the first level trigger. Together with the Forward Range Hodoscope it can be used for the particle identification by means of the ΔE-E method. After the inclusion of the

new Forward Veto Hodoscope in 2008, Time-Of-Flight measurements became possible utilizing the FWC as start detector [46].

The Forward Proportional Chamber (FPC)

The FPC [47] is a tracking detector made of 16 layers, 122 aluminized Mylar straws each grouped by four layers in one module. The 4 modules are rotated by 45° with respect to the azimuthal angle Φ of the previous module providing precise and complete three-dimensional information.

In the center of the 8 mm diameter straws a sensing wire of 35 μm thick stainless steel is used as anode wire. A 80%-20% admixture of argon and ethane (C_2H_6) fills the drift tubes, the same as for the MDC. Different projections of the modules can be seen in fig. 3.9.

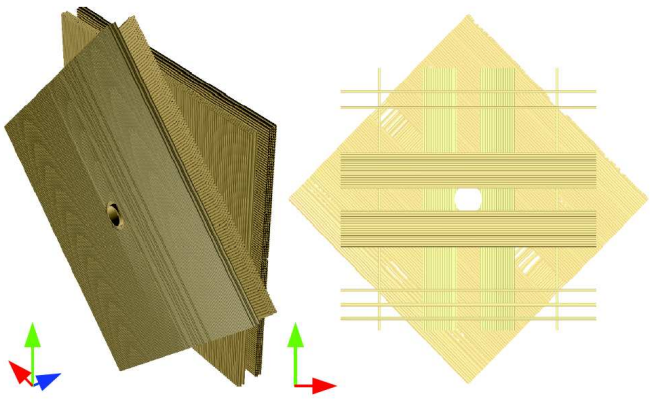

Figure 3.9: Forward Proportional Chamber (FPC) in two different projections, lateral (left), where the coordinate system in the corner of the picture shows the beam-direction as a blue arrow, and as seen in beam direction (right), where some tubes are removed to show the structure of the layers. From Ref. [47]

The Forward Trigger Hodoscope (FTH)

The Forward Trigger Hodoscope (FTH) is the next sub-detector in down-stream direction. It consists of three layers of 0.5 cm thick plastic scintillator. The last two planes are made of 24 Archimedean spiral segments each oriented clockwise and counterclockwise respectively, while the first layer is divided in 48 straight sectors (fig. 3.10)

aligned with the 48 sectors of the PSF and PSB. The superposition of two spiral elements and a straight one forms a *pixel*. The FTH thus gives information about polar and azimuthal angles of charged particles in forward direction. It also defines the charge track multiplicity at the trigger level, and provides energy loss information for particle identification (ID) and kinetic energy reconstruction. More information can be found in Ref. [48].

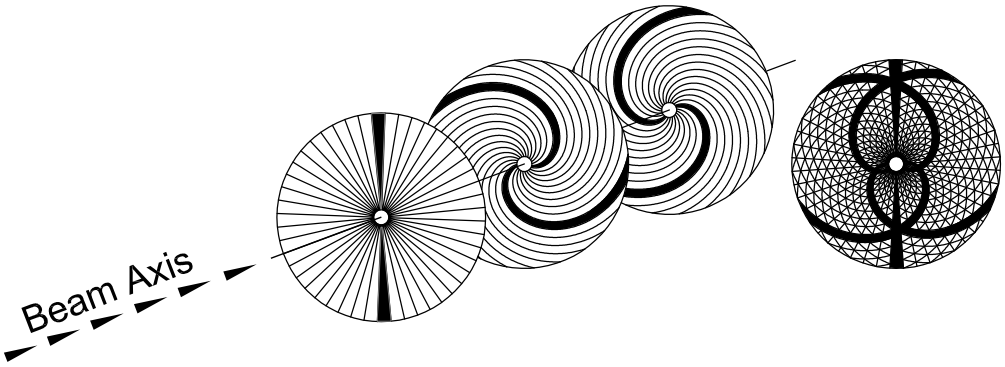

Figure 3.10: Sketch of the Forward Trigger Hodoscope. In the right picture one can see the pixel structure. From Ref. [48]

The Forward Range Hodoscope (FRH)

The FRH, see Fig. 3.11, consist of five layers of thick plastic scintillator cake-shaped elements. The first three layers are 11 cm thick and the last two 15 cm thick. Its main purpose is the kinetic energy reconstruction of forward going charged projectiles. Their identification is done via the ΔE-E technique with the different combinations of layers. The best energy resolution achieved with the FRH corresponds to stopped particles and is about 3%. Tab. 3.3 shows the stopping power for the most common particles identified in the FD at WASA. For larger energies the resolution worsens linearly, reaching 15% at 1 GeV in the case of protons.

A good calibration of this detector is thus mandatory to achieve a good kinetic energy reconstruction. The calibration procedure will be described in Sect. 5.8.

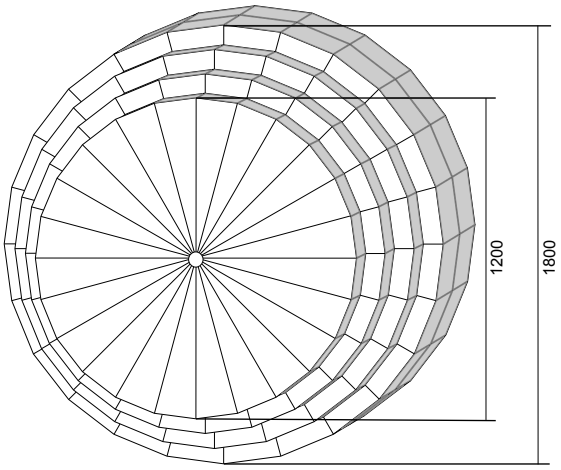

Figure 3.11: Forward Range Hodoscope. The dimensions are in mm.

Particle	Ekin to reach FRH1	Ekin to punch through FRH5
π	25 MeV	200 MeV
p	60 MeV	370 MeV
d	80 MeV	485 MeV
^{3}He	215 MeV	1325 MeV
^{4}He	240 MeV	1475 MeV

Table 3.3: Minimum and maximum kinetic energy for various particles stopped in the FRH.

The Forward Range Intermediate Hodoscope (FRI)

The Forward Range Intermediate Hodoscope is a 2-layer sub-detector located in-between the second and third layers of the FRH. Each layer is made up of 32 rectangular elements, 5.2 mm thick, aligned horizontally and vertically, respectively, in order to allow a two dimensional position determination. Fig. 3.12 shows a sketch of the FRI. More detailed information about the design and performance of this hodoscope can be found in Ref. [49].

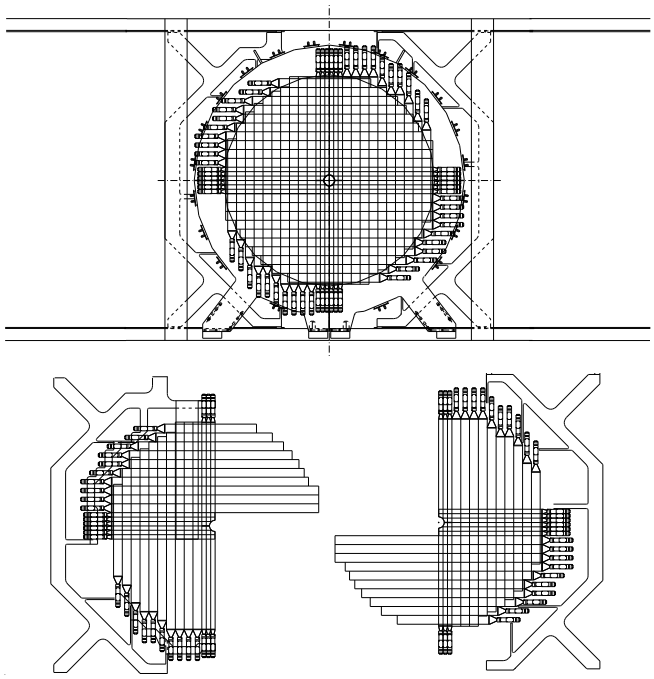

Figure 3.12: Forward Range Intermediate Hodoscope (FRI). From Ref. [49].

The Forward Veto Hodoscopes FVH1 and FVH2

The Forward Veto Hodoscope is the very last detector downstream in forward direction. It was initially constructed as a single layer detector (FVH1 now) which operated already at CELSIUS [50]. The FVH1 consist of 12 horizontal bars of plastic scintillator with dimensions 165 cm x 13.7 cm x 2 cm. The main purpose of this layer is to tag particles energetic enough to punch through the Range Hodoscope. The signal from the FVH can be used as veto increasing thus the trigger efficiency. The bars are equipped with XP2020 photomultipliers at both ends, allowing for the determination of the position of the hit in x-direction with an accuracy of about 5 cm [28]. A schematic view of the FVH1 is shown in Fig. 3.13.

With the modifications applied to the detector after accommodating it at COSY the FVH1 no longer covered the angular range for what the detector was projected. To solve this, a second layer (FVH2), which fully covers the forward scattering angles of WASA from 3° to 18°, was added in 2008. The second layer of the FVH is also equipped with a double readout. The plastic scintillator bars are positioned along the

y axis to create a grid of rectangular pixels together with the FVH1. The FVH2 is made up of 22 scintillator bars with variable sizes and middle bars that fit the beam-pipe by means of a 90° readout. Additionally, two horizontal bars placed at the back, which can be positioned along the Y-axis, can be used for calibration purposes. The design and assembling of this layer is described in Refs. [28, 51]. With the FWC used as start and the FVH2 as stop detector, the WASA setup can be used to perform Time-Of-Flight measurements; in particular, this technique would also allow to identify fast protons and pions originating from η' production reactions [46]. The FVH2 is shown in Fig. 3.14.

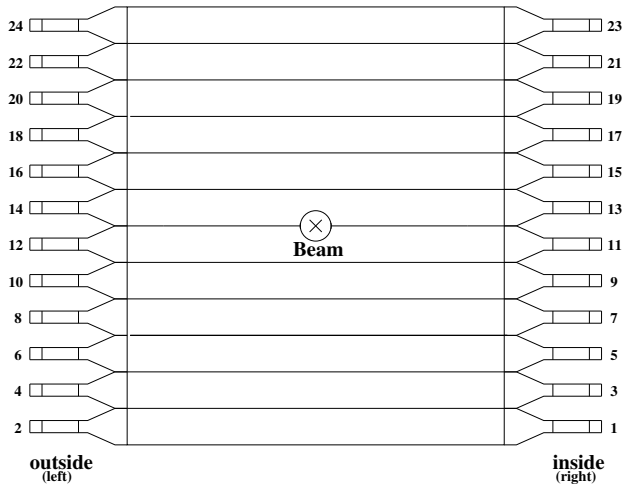

Figure 3.13: Old Forward Veto Hodoscope FVH1. From Ref. [50]

3.3 The Light Pulser Monitoring System (LPS)

For its most part, the WASA detector is made up of modules of scintillators connected to PMTs. The light from the scintillator is passed onto the PM tube, translated into an electric signal and amplified. To correctly and precisely extract the associated deposited energy in the scintillator from the signal one needs to rely on the amplification of the signal. This implies that the gain of the PMTs is stable. A stable gain is only possible in an ideal setup. In order to monitor the gain drifts a Light Pulser System (LP) has been integrated into the WASA setup. The LP works by emitting flashes of

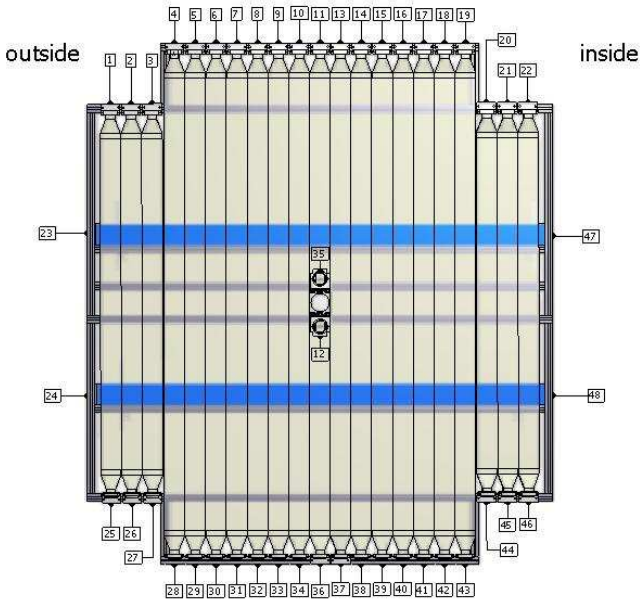

Figure 3.14: New Forward Veto Hodoscope FVH2. From Ref. [51]

light at several kHz by means of a Xenon Light Pulser in case of the CsI(Na) crystals, or LED sources for the case of the plastic scintillators. The pulses are transmitted via a network of optical fibers and the stability of the signal is monitored by photodiodes. These signals are taken as references to which the response of the detector to the light pulse is normalized. This information can be used later-on in the off-line analysis to correct for changes in the gain. A more detailed description of the LP system is found in Ref. [52].

3.4 Data Acquisition System - DAQ

The DAQ system was designed to cope with the desired luminosities at WASA-at-COSY and is based on the third generation of DAQ systems used in experiments at COSY [53]. The signal readout has being optimized by using FPGA boards for digitization and buffering of the data. Signals are stored and saved only if a trigger signal arrives. Synchronization and readout is done in the EMS framework [54], which has been developed at the Forschungszentrum Jülich and is used in several experiments at

COSY. The structure of the data acquisition system is schematically shown in Fig. 3.15.

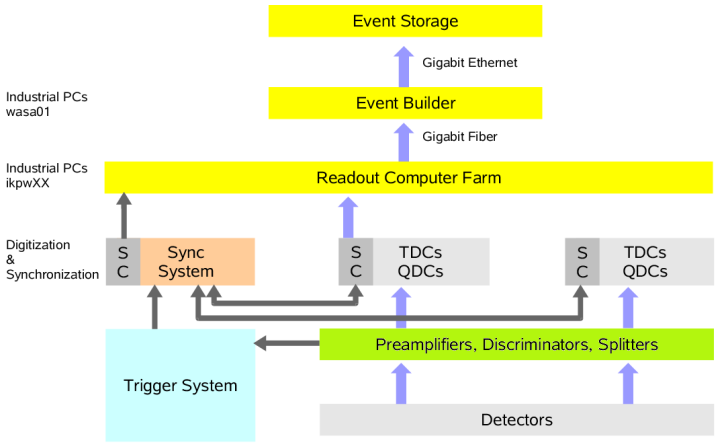

Figure 3.15: Chart of the WASA DAQ system flow from Ref. [55].

The dead time introduced by the system is of about 20 μs. The event size and the writing speed of the hard drive, of about 80 MB/s, are the limiting factors for the system. Trigger rates of 10 kHz with typical event sizes of 8kB are possible at a lifetime of 80% of the system.

The analog signals from the scintillators are sent to Charge-to-Digital Converters (QDC) and discriminators via splitter boxes. The logic signals provided by the discriminators are used in the trigger system and also recorded by Time-to-Digital Converters (TDC). In the case of the FWC, for example, two splitter boxes are used to separate the signal into branches and allowing low and high thresholds to be used in the trigger at the same time. The QDC modules have 16 input channels each and the signals of each channel are continuously sampled by FlashADCs. The evaluation of the digitized signals is done by FPGAs (Field Programmable Gate Arrays). Along with charge integration, double pulse detection, time stamping by zero crossing detection and pedestal subtraction are performed. For debugging purposes the signal amplitude and the baseline can be obtained as well.

The fast signals from the scintillators and the slow signals from the calorimeter have different shapes, reason why two different types of QDCs are used: **SlowQDC** and **FastQDC**, with sample rates of 80 MHz and 160 MHz respectively. The timing

properties of the detectors also demand different types of TDCs to be used. In this case a **FastTDC** based on the GPX ASIC modules [56, 57] is used for the signal from the scintillators and a **SlowTDC** is used for the straw chambers, with modules based on the F1ASIC [58], 64 input channels each.

The synchronization system is used to control and synchronize the data flow. When the trigger system issues a trigger, the synchronization system generates an event number with a time stamp which is delivered to all crates to start the read out of all QDC and TDC modules. The digitized data are sent via high speed optical links to the PC computer farm and further to an event builder to store the data streams in a cluster format for the off-line analysis.

3.5 Trigger System

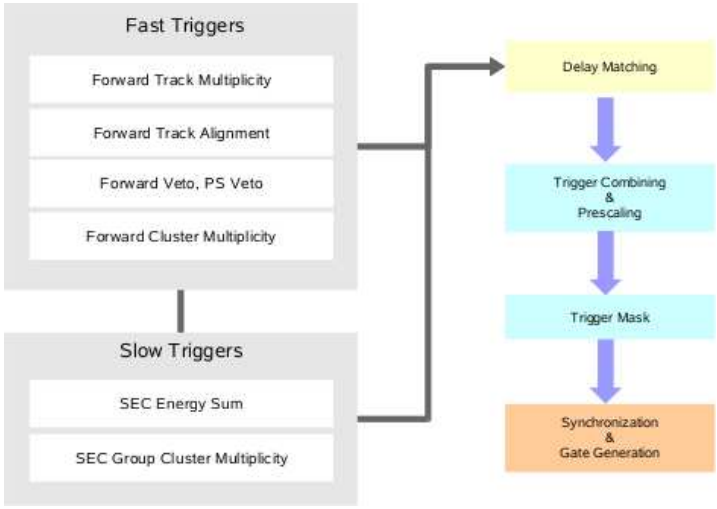

Figure 3.16: Overview of the WASA Trigger System.

Given the design luminosities of the WASA detector of $10^{32}\text{cm}^{-2}\text{s}^{-1}$, the data acquisition system has to deal with event rates of the order of 5 MHz in the case of *pp* reactions. To reduce the initial amount of events a trigger system selects only those events from reactions of interest. Fig. 3.16 sketches the trigger system used in the data acquisition at WASA.

The trigger decisions are based on multiplicities, coincidences and track alignment

in the plastic scintillator detectors and on cluster multiplicities and energy sums in the electromagnetic calorimeter.

In the first stage, hits in neighboring detector elements are treated as a cluster created by one incident particle to produce a set of primary trigger patterns. For this purpose a coincidence window of 20 ns is used as default.

The information from the calorimeter (SEC) takes into account the cluster multiplicity and energy sums. For this aim, the electromagnetic calorimeter is divided into three groups of hardware clusters of 12 crystals in the forward part, 9 in the backward and 16 for the central part. Coincidence of the hits with the Plastic Scintillator Barrel (PS) is used to discriminate between charged and neutral clusters.

The primary signals are combined in coincidence matrices to form more complex trigger expressions, up to 32 different coincidence conditions can be used. To balance the event rates, high rate triggers are prescaled.

4

DIRC Detector for WASA-at-COSY

The DIRC (**D**etection of **I**nternally **R**eflected **C**herenkov Light) detector and prototype was planned to be installed at WASA in order to increase the energy resolution and to allow for a better discrimination of protons and pions in η and η' production experiments. The additional goal was to test the capabilities of several designs for the future PANDA experiment at FAIR [59].

Two Disc DIRC prototype quarters were built, one at Tübingen and another one at Erlangen university. In this chapter the basic concepts of DIRC detectors and the characteristics of the quarter designed by the Tübingen group as well as the latest results from the tests are presented. For more information see Ref. [60].

4.1 DIRC Detectors

The concept of the DIRC is based on the electric polarization of a medium, in this case of a radiator with refractive index n. When a charged particle transverses it with a velocity $\beta = \frac{v}{c} \geq \frac{1}{n}$, it produces Cherenkov photons, which are emitted in a cone with half opening angle $cos\theta_C = \frac{1}{\beta n}$, see Fig. 4.1. In a properly designed setup, the Cherenkov angle of the wave front is conserved through internal reflections along the radiator, until it reaches the focusing elements, see sketch 4.2.

Together with the angle of the track and the momentum, the angle of the emitted Cherenkov radiation allows to calculate the mass of the particle. In the particular

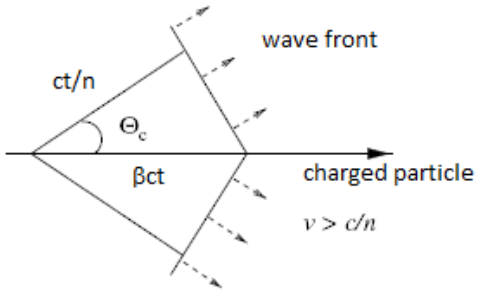

Figure 4.1: Sketch of the propagation of the Cherenkov light in a medium of refractive index n.

case of the WASA detector there is no momentum measurement in the FD, but energy instead. The intensity of the Cherenkov radiation (number of photons per unit length of particle path and per unit of wave length) is given by [61]:

$$\frac{d^2N}{d\lambda dx} = \frac{2\pi z^2 e^2}{hc\lambda^2}(1 - \frac{1}{n^2\beta^2}) = \frac{2\pi z^2}{\lambda^2}\alpha sin^2\theta_C \tag{4.1}$$

where α is the fine structure constant, z the charge of the particle , λ the wavelength of the emitted light. This leads to an approximate number of $\frac{dN_\gamma}{dx} = 490 \cdot z^2 sin^2\theta_C$ photons per cm in the case of an ideal 100% efficient detector for wavelengths of the radiation between 400 and 700 nm[1]. This low intensity makes efficient collection of the light an important issue in the design of a DIRC detector.

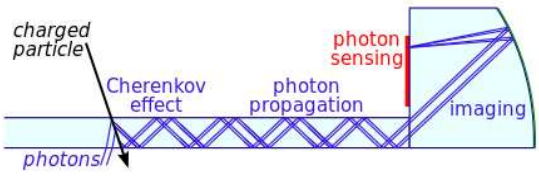

Figure 4.2: Cherenkov light propagation in a DIRC detector. The design corresponds to the Tübingen prototype. From Ref. [62].

[1] typical sensitivity of the PMTs used in these experiments.

4.2 The DIRC Detector for WASA-at-COSY

The implementation of a DIRC detector at WASA was proposed to improve the identification of forward going particles. Of special interest was its use to discriminate protons from the reaction $pp \rightarrow pp\eta'$ against pions and protons from competing pp reactions.

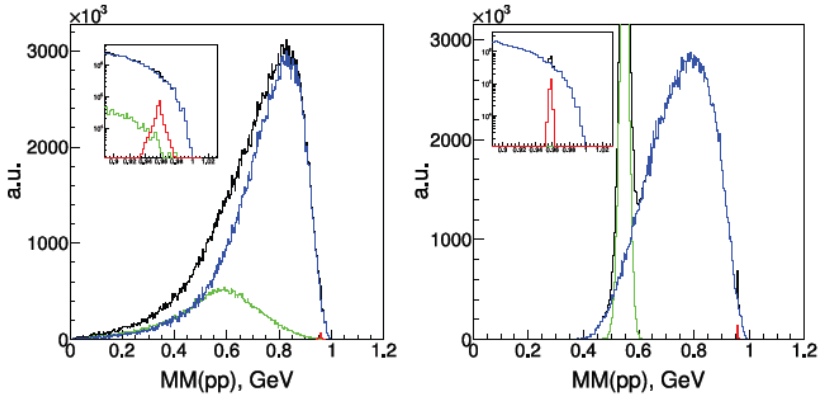

Figure 4.3: MM_{pp} missing mass for simulated events. Red are initial $pp \rightarrow pp\eta'$ events, green are $pp \rightarrow pp\eta$ events and blue corresponds to non-resonant reactions. **Left**: without DIRC, **right**: with inclusion of DIRC. From Ref. [63]

Physic simulations with parameterized energy resolutions were performed to study the impact of the inclusion of a DIRC detector at WASA in the η' missing mass [64]. In Fig. 4.3, the comparison of the missing mass spectra without and with DIRC shows the expected improvement.

The intention was to include the DIRC detector in front of the FRH. Two prototypes were built, each covering a quarter of the forward acceptance. One design was in charge of the Erlangen University and the other one in charge of the Tübingen University. In Fig. 4.4 the schematic view of the WASA detector with the inclusion of both DIRC prototypes is shown.

Both detectors were planned to have a 20° inclination with respect to the XY-plane in order to cover the energy range of protons from η' production reactions. Plexiglas with n=1.1496, was chosen as material for the optical components.

The Tübingen design consisted of radiator quarters with a 645 mm radius and

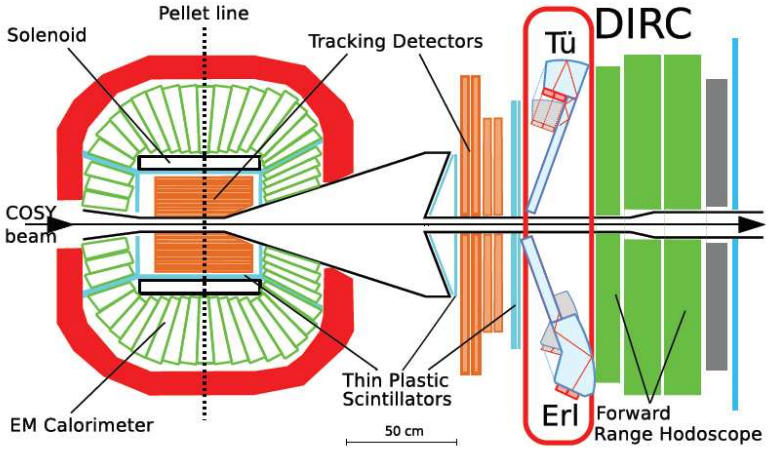

Figure 4.4: Schematic view of the DIRC at the WASA setup. The Tübingen prototype is at the top and the Erlangen one at the bottom. The grey areas show the space needed for the PMTs and readout electronics. From Ref. [63]

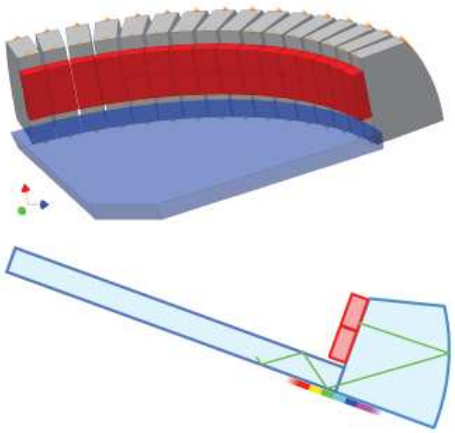

Figure 4.5: Schematic drawing of the Tübingen DIRC prototype. **Top** shows the radiator and focusing elements arrangement. **Bottom** is a cross sectional view. Red denotes the position of the PMTs. From Ref. [63]

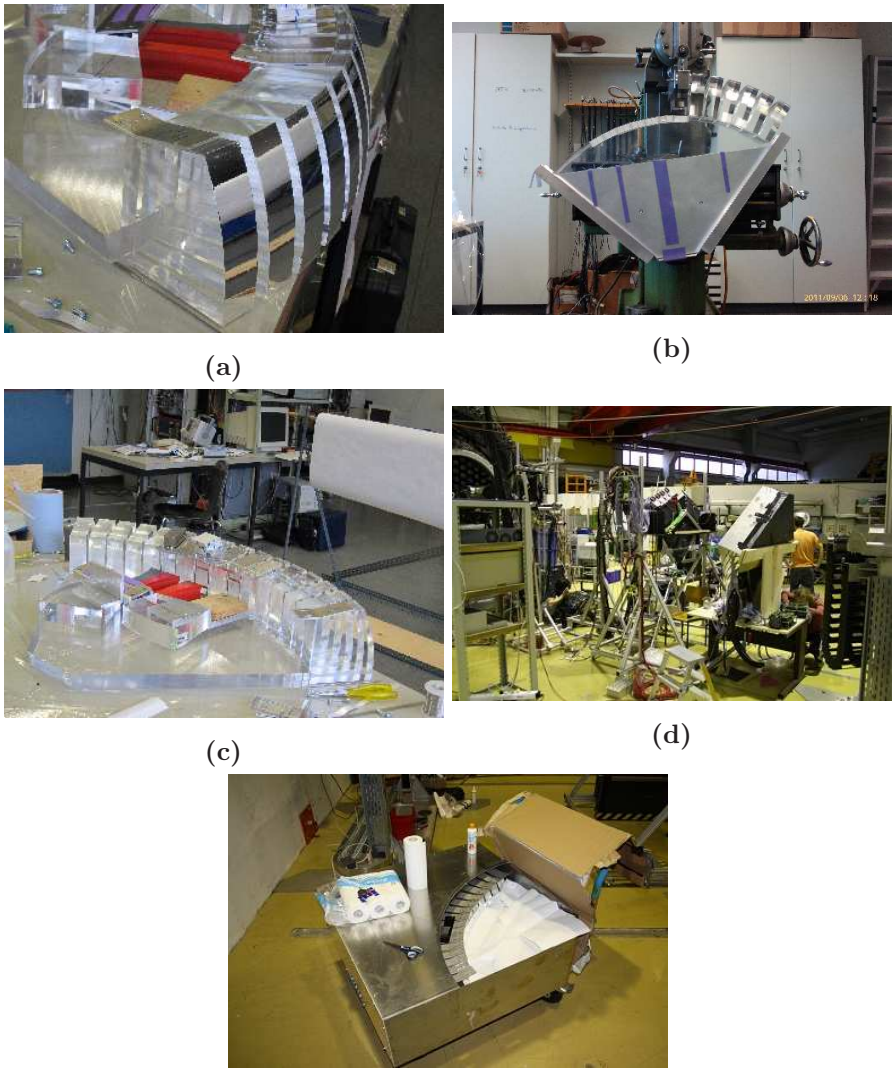

Figure 4.6: The DIRC detector mounting at different stages. From the gluing station in Tübingen, where all focusing elements and holding structures were glued and mounted(a, b and c), to the last stage for the testing in TOF at Jülich Forschungszentrum (d and e).

40 mm width, see Fig. 4.5. The rim of the radiator is covered by Plexiglas focusing elements, 16 per quarter, glued to it with epoxy. The focusing elements are of polynomial shape and coated using the same epoxy with VM2000 reflective foil to reflect the Cherenkov photons from the radiator into the photomultipliers. For the PMTs two models were tested and used: the Hamamatsu 8500 8x8 Multipixel Photomultiplier and the Hamamatsu R8900-100-M16 with 8x8 pixels and a higher quantum efficiency. Details of the design of the focusing elements, radiator, casing and PMTs can be found in Ref. [60]. In Fig. 4.6 different pictures of the DIRC detector at several stages of the assembling in Tübingen are shown.

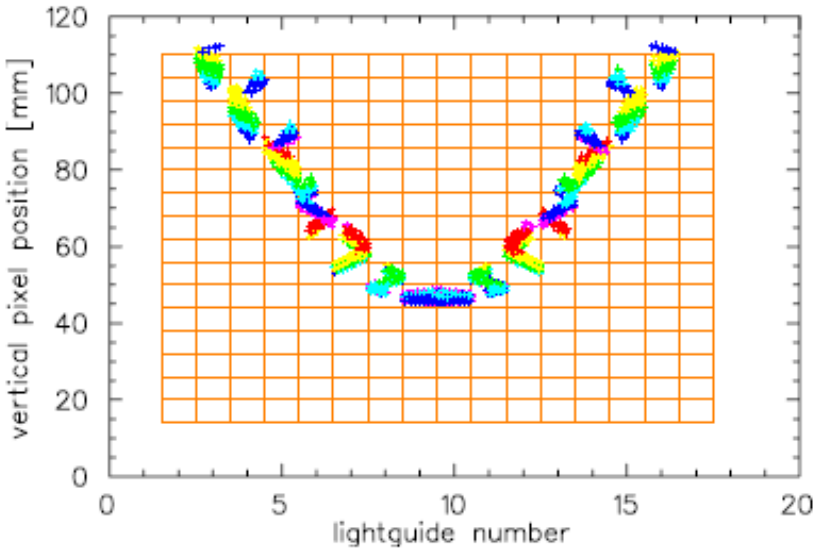

Figure 4.7: Simulated photon hit pattern from the Tübingen prototype at $\theta = 9.5°$ proton emission angle and $\beta = 0.8$ particle velocity. The color represents the position of the last reflection on the flat radiator surface in 20 mm bands, see Fig. 4.5. From Ref. [63].

Single event photon patterns have been also simulated for both detectors. The expectation for the Tübingen prototype is shown in Fig. 4.7 for a given angle and velocity of the incident protons. It depicts the pixel position, if the 8x8 Multipixel PMTs design is used, versus the focusing element number. This is, the radial position of the hit versus the tangential one, see Ref. [63].

4.3 DIRC Tests and Results

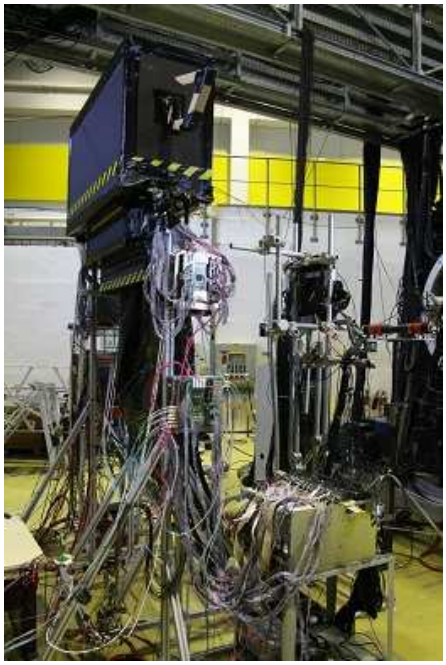

Figure 4.8: DIRC setup in TOF for the test in October 2013. The box on top is the Erlangen quarter prototype. At the bottom is the Tübingen prototype. The TOF beam line is located to the right of the picture.

The last stage was the testing of the prototypes. This was done in conjunction with the Erlangen group on several occasions in 2012/2013. The setup for the tests was mounted behind the TOF experiment at COSY. The PMTs were installed and the two quarters from both groups arranged behind the exit of the TOF detector. Fig. 4.8 shows the disposition of the quarters in the experiment, the Tübingen prototype at the bottom and the Erlangen prototype at the top. The TOF beam line provided protons with momentum $P_p = 3.2$ GeV/c. Two aligned hodoscopes in the beam direction, one as target and the second one to tag the emitting protons and for trigger purposes were located in front of the DIRCs, see scheme in Fig. 4.9.

The preliminary results, provided by A. Zink, show clear hit patterns for single events as shown in Fig. 4.10. The histogram shows the tangential position in the x-axis, this is the focusing element number, and the radial position, or vertical pixel position of the PMTs located at the end of the focusing elements, in the y-axis. The

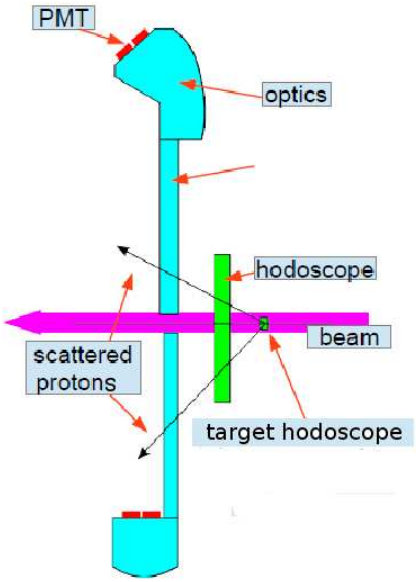

Figure 4.9: Schematic view of the DIRC setup for the test in the TOF experiment area. The pink line shows the beam direction. Taken from Ref. [65]

horizontal line in bright green color corresponds to the signal. This is expected from the simulations, since for protons at this energy the concave pattern, see Fig. 4.10, becomes flatter. In the plot a second line is seen above the signal and with a concave arc-shape. This secondary signal is due to reflections on the sides of the radiator. During the mounting of the prototype the sides were covered with black material to reduce this effect but it was not possible to eliminate it completely.

The second picture, in Fig. 4.11, shows the hit spectra for single events. The extracted mean corresponds to 19 photons per event measured with the Tübingen DIRC, what is in agreement with the simulations [62].

Although the installation in WASA has been suspended, the different tests are very valuable to evaluate the different design features and capabilities. The data collected are being analyzed and will be presented in the doctoral work of Adrian Zink [66]. In the tests, the Tübingen design has proven to be up to the expectations from simulations.

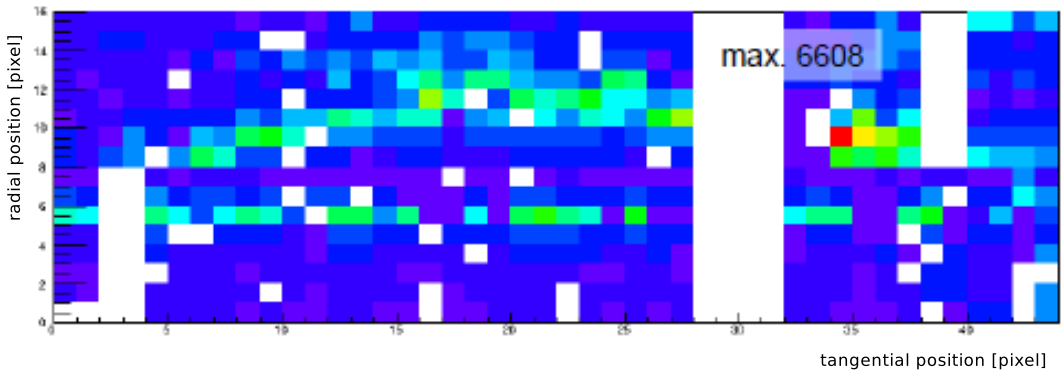

Figure 4.10: Single event hit pattern from Tübingen DIRC. The concave arc is created due to reflections on the sides of the detector. The x-axis show the tangential position whereas the y-axis correspond to radial position. Its gradient goes from dark blue (minimum) to red (maximum) to indicate the number of counts. From Ref. [65]

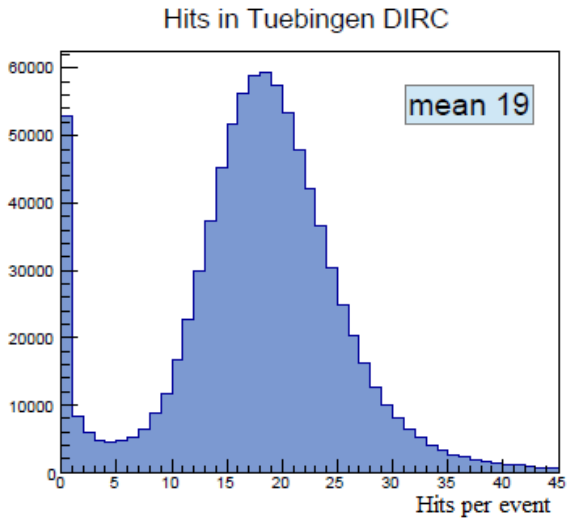

Figure 4.11: Measured hits per event spectra from the Tübingen DIRC. From Ref. [65]

5

Event Analysis: From Signal to Meaningful Data

As described in the previous chapter the signals from the detectors are combined in data streams and stored for the off-line analysis. Preselection, calibration and event selection are some of the many steps that one needs to identify the events from the reaction of interest. Also, Monte Carlo models and detector response simulations need to be carried out. In this chapter some of the programs and methods used with the data and simulations for the analysis of the reaction are presented as well as an overview of the experimental data.

5.1 Experiment

The data presented and analyzed in this work correspond to three different periods of data collection. One of the data sets was taken from the η meson measurements carried out with WASA in August/September 2009, with proton beam at 1.0 GeV kinetic energy and a deuteron target to study rare η decays. The other two sets correspond to measurements with deuteron beam and deuteron target at two different energies, 1.4 GeV and 1.7 GeV, which allows to study proton deuteron collisions with an extra nucleon, which behaves as spectator. These two quasi-free measurements were taken in two different periods, the first one corresponds to the ABC study from December 2007 presented in Ref. [28], the second one corresponds to a two days measurement carried out in December 2010 during the main experiment dedicated to $^4\mathrm{He} - \eta$ bound state

Experiment Date	beam	target	T_{beam}	B Field	No. runs	Run numbers
December 2007	d	d	1.4 GeV	1.0 T	131	5359-5500
August/September 2009	p	d	1.0 GeV	0.85 T	76	13983-14060
December 2010	d	d	1.7 GeV	0.0 T	192	23048-23252

Table 5.1: Summary of the data sets used in this work

and kindly handed over to us by Prof. Pawel Moskal. Tab. 5.1 summarizes the main characteristics of the sets. Due to problems with the liquid helium for the superconducting solenoid the data from December 2010 were taken without magnetic field in the solenoid (SCS).

5.2 Preselection

As the trigger arrives, the data from the buffers are stored for further processing. The file sizes are still extremely large at this stage. To reduce the file size and clean up the data, a preselection based on the experiment interests is done. In this work three different data sets were analyzed and only in one case (Dec. 2010) the preselection was done as part of the work, for the other sets already available preselected data were used.

For the Dec. 2010 experiment data, a preselection based on geometrical and deposited energy demands, similar to the one described in Ref. [28], was applied. Exactly events with one track in FWC, FTH1, FTH2 and/or FTH3 and FRH1 from the main trigger and with some request on the energy deposited in the FRH was selected, also LP (Light Pulser) events were saved. For the particles stopped in the FRH1, a condition on the energy deposited in FRH1, see Fig. 5.1, was applied. If they punch through the first layer of the FRH, the condition lays on the energy deposited in FRH1 versus the sum of all five FRH layers, see Fig. 5.2. With these conditions the ^3He events are saved and events with protons and deuterons, which deposit less energy in the detector, are discarded. In Fig. 5.3 one can see the effects of different selection conditions applied to the data. After the geometrical demands are satisfied, the energy conditions are applied leading to a considerable reduction of the number of events to be saved and

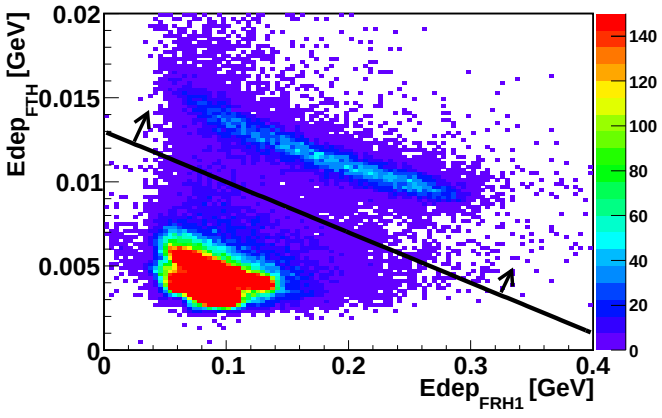

Figure 5.1: Typical deposited energy in FTH1 vs FRH1 for charged particles stopped in the FRH1. Black line shows the energy condition applied in the preselection.

stored for the analysis. The amount of rejected events with these conditions may be as big as 95%. The highest contributions to the rejection of events come from requesting events from the main trigger and also from the energy conditions. This way all fast particles, such as protons and deuterons, can be eliminated.

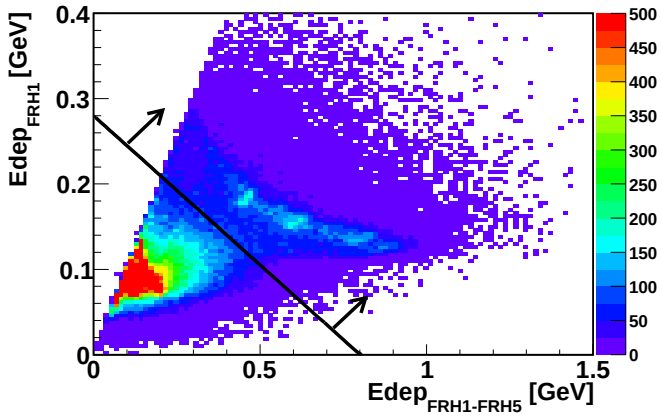

Figure 5.2: Deposited energy in FRH1 vs the sum of all FRH layers for events punching through the FRH1. Black line shows the acceptance condition.

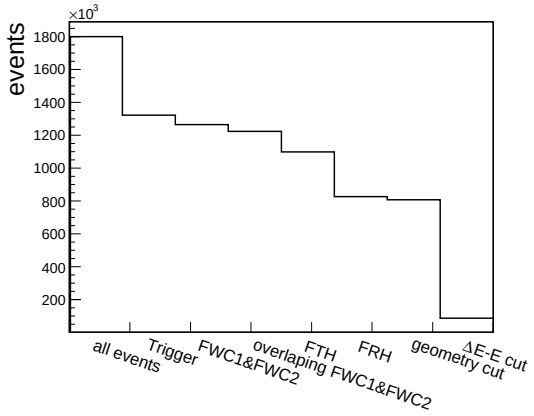

Figure 5.3: Event reduction for the various preselection conditions based on single run analysis.

5.3 *RootSorter*

The analysis of the data is done, both on-line and off-line, with the *RootSorter* framework [28, 67]. It is based on ROOT [68] libraries and organized in modules that are called on-demand. The RootSorter packages were developed for the ANKE experiment at COSY and adapted for the WASA-at-COSY needs. This framework provides low-level modules to be loaded during the on-line analysis for monitoring the experiment as well as more dedicated high level modules that are used for more specific tasks, like calibration, track reconstruction, etc. High-level specialized analysis modules for given reactions are to be designed by the WASA users.

The data from the WASA detector is stored as a bank of hits, containing information about the ADC and TDC from detector, this is the HitBankRaw. This information will then be translated, after calibration, to energy and time and stored in the HitBank. A common Database keeps track of all decoding tables, calibration constants, geometry files and others that are needed to interpret the data. These files can be loaded for the specific beam times via command line. Alternatively they can be called by run number, time of the run or file name.

In the case of Monte Carlo simulations initially a perfect detector is assumed. Thus instead of pre-calibrated information comparable to that in the HitBankRaw the simulations are stored in the HitBankMC and then smeared according to the real detector

resolution.

The hits, when belonging to the same particle, can be grouped into clusters and then put to a ClusterBank. All clusters from a detector module, which can be assigned to a single particle, define a track. Tracks are then stored in a TrackBank. More details about how hits are clustered and combined into tracks in the Forward and Central Detectors of WASA, can be found, e.g. in Refs. [28, 55].

5.4 Event Generator

To simulate the desired reactions for later comparison and correction of the data the TGenPhaseSpace generator is used. This is a n-body reaction generator which produces a set of Lorentz-Vectors uniformly distributed over the kinematically allowed region of the phase space. Every event is assigned a weight or probability. Then the *acceptance-rejection* method is applied to obtain the events. In this method a probability is computed for each event by comparing the weight to a random number in the interval from zero to some value larger than the largest possible weight for the reaction to be simulated. If this random number is larger than the weight, then the event is rejected. This leads to a higher population of the regions for which the weights are larger. With this method the events will have all the same weight as it is in the case of data. The generated weights can just follow a phase space distribution as they are generated by the ROOT package or any other model description by multiplying the initial weights with the desired distribution.

5.5 WASA Monte Carlo (WMC)

The simulation of the detector components and response is done with the WASA Monte Carlo package. It is written in FORTRAN and based on the GEANT3 libraries developed by CERN and accommodated for previous experiments with CELSIUS/WASA. This simulation package reproduces the detector response with the help of geometry parameters, materials, magnetic field, etc. collected in a database and via an input data file with 4-vector information of the decaying particles of a given reaction or by means of an internal generator, used mainly to create single tracks in

the detector. WMC provides an output file with the same format, given by the *.ems* extension, as the experimental data for a posterior analysis.

5.6 EventTree

The *.ems* files obtained from the experiment are still too large even after the preselection, and have a lot of information that is not longer needed for the analysis. That is why a more suitable and compact way to store and further process the data is needed. For the same reason the corresponding files from the simulation obtained from WMC are not well suited for direct work. Hence TTree structures are used. All events, both data and simulation, are processed through the RootSorter packages, tracks are reconstructed, calibrated and the most important observables are stored in Trees. This is done with the EventTree module developed by M. Bashkanov.

5.7 Magnetic Field Correction of Forward Tracks

Due to the influence of the solenoid the charged particles flying in forward direction will follow a helical path as long as they are influenced by the magnetic field and then continue into the Forward Detector in a straight line. Due to this the particles' azimuthal angle measured in the FD will be different from the original one because of the influence of the magnetic field in the tracking. The original angle can be restored by using a correction factor via the formula:

$$\Phi' = \frac{l \cdot 0.3 \cdot q \cdot B}{P \cdot cos\theta} \tag{5.1}$$

where Φ' is the correction angle in radians, l is the length traveled within the field in meters, q is the charge of the particle in units of electron charge, B is the magnetic field in Tesla, P the momentum of the particle in GeV/c and θ the polar angle, also in radians. A detailed derivation of this formula can be found in Ref. [26].

In the case of this work the only particles measured in the FD are Helium ions, thus, the charge is $q = 2$. The momentum, P, is recalculated from the kinetic energy reconstructed from the deposited energy information from the FRH.

5.8 Calibration of the FD

In this work the reaction $pd \rightarrow {}^3\mathrm{He}\pi^0\pi^0$ is measured. The helium particles are detected in the FD of WASA while the pions are reconstructed from their decay products in the CD, see Chap. 6 for more detail. In this section the calibration of the FD of WASA is explained. The CD calibration was not part of this work but taken from the previous experiments.

The measurement and identification of the ^{3}He particles in the WASA FD detector is done based on the reconstructed deposited energy from the FRH. This motivates a very careful and dedicated calibration for all elements of all five FRH layers.

Extracting energy and time information from ADC and TDC channels respectively demands calibration of the detector. In an ideal case the energy calibration is done by assuming a linear relation between the energy deposited by the particles in the detector and the ADC channels. However, the light collection is influenced by various effects that need to be accounted for, such as: non-uniform light collection efficiency, non-linear behavior of the PMT tubes, dependency of the scintillator response on the particle type (quenching), aging of the detector elements, etc. In large detectors the main effects in light collection that need to be corrected are: the non-uniform light collection efficiency, which depends on the detector geometry, quenching and non-linear response of the PMTs.

The deposited energy is reconstructed from the ADC information of the PMTs. In the ideal case the relation is linear, but due to the variation of the light propagation paths the light collection efficiency gets position dependent and shows a non-uniform behavior over the scattering θ angle. Also one needs to keep in mind that a large θ angle also implies a long path inside the scintillator, so the particle will deposit more energy in that element. To account for this θ-dependence we need to multiply the ADC values by $cos\theta$. That way we will obtain the ADC value per width of the element, which is independent of θ, instead of ADC value per path.

To account for non-uniform light collection, $ADC \cdot cos\theta$ vs θ is plotted for minimum-ionizing particles for each element in the FRH. Their energy is approximately 2 MeV per g/cm^2. Thus, assuming all elements to be uniform in width, the deposited energy of such particles should be the same for all θ angles, which however is not the case,

see Fig. 5.4. To extract the correction this plot is fitted to a third order polynomial $f_{NonUn}(\theta)$, see Fig. 5.4.

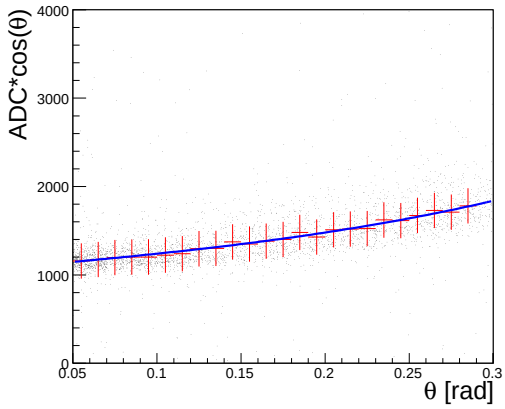

Figure 5.4: $ADC \cdot cos\theta$ vs θ for element 3 of FRH1. The blue line is the corresponding fit with a third order polynomial.

Non-linearities can originate from non-linear effects in the PMTs and from quenching effects in the scintillator material. Since we are interested only in the ^{3}He particles the calibration is done only for these. The non-linearities are corrected with a third order polynomial $f_{NonLin}(ADC)$. The deposited energy is then calculated as:

$$E_{depe} = \frac{f_{NonLin}(ADC)}{f_{NonUn}(\theta)} \tag{5.2}$$

To extract the non-linearity parameters, the deposited energy from the experiment is compared to the MC generated event[1] in the closest θ bin and a χ^2 is defined as the sum of the squares of the difference between the experimental and the simulated deposited energy in each detector layer over σ^2, the square of the error from the Monte Carlo simulation:

$$\chi^2 = \sum_{1}^{5} \frac{(Edep_i^{MC} - Edep_i)^2}{\sigma^2_{MC,i}} \tag{5.3}$$

That way $f_{NonLin}(ADC)$ is calculated by minimizing χ^2 with the help of the TMinuit package from ROOT. The minimization process results in a very good calibration

[1]Since MC events also contain quenching, there is no need to consider extra corrections at the calibration level.

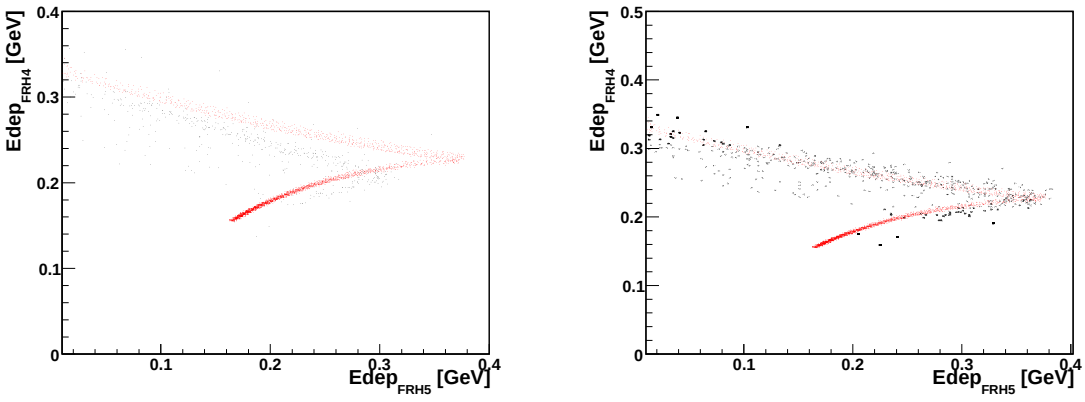

Figure 5.5: Left: Deposited energies in FRH4 vs FRH5 before the calibration. Black points correspond to data and red points to the MC simulation. **Right**: Deposited energies in FRH4 vs FRH5 after the calibration. Black points correspond to data and red points to the MC simulation. The algorithm *CorrectStatistics* was used here.

of all layers in the FRH. The plot in Fig. 5.5 shows the $\Delta E - \Delta E$ distributions for element 2 in the FRH before and after non-linearity calibration, respectively. This plot corresponds to the more upstream layers and thus to those with fewer events and hence harder to calibrate. Some regions of the $\Delta E - \Delta E$ plots had not enough events, this interfered with the calibration procedure. To solve it the algorithm, *CorrectStatistics*, to equally populate them, was prepared. Its description can be found in the Appendix 9.2.

During the calibration, a malfunction of element 22 of FRH2 was discovered and after several checks it was decided to drop this element from the analysis.

5.9 Kinetic Energy Reconstruction

To reconstruct the kinetic energy of the ^{3}He, the deposited energies measured with the FRH are compared to the generated ones. For this purpose, single tracks in the forward detector at several kinetic energies were generated. For each energy and θ bin, the deposited energy distributions are fitted with a Gaussian. The fit parameters of this Gaussian were then stored in ROOT TTrees as translation tables for deposited to kinetic energy conversion.

Then, for each energy the sum of the squares of the difference between the experimental and the simulated deposited energy in each detector layer weighted by the error of the Gaussian fit in each detector is calculated:

$$D = \sum_{detector} \frac{(Edep_i - Edep_i^{MC})^2}{\Delta Edep_i^{MC}} \tag{5.4}$$

For the best value of D, the kinetic energy is taken from the translation tables in the TTree. Only detectors with a hit in both, simulated and reconstructed data, were considered.

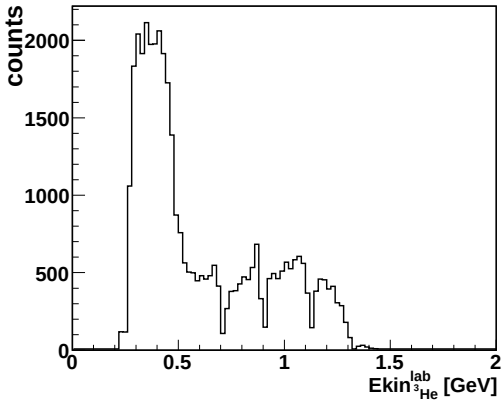

Figure 5.6: Kinetic energy of ^{3}He from the quasi-free measurement at $T_d = 1.7$ GeV. The gaps correspond to the energy boundaries of the FRH.

The sum may run over all detector layers in the FD or only a subset. At the energy boundaries between the FRH layers, the deposited energies of the Helium particles stopping and punching through become very close, resulting in small systematic errors in the reconstruction that lead to a "toothed" spectra in the reconstructed kinetic energies, see Fig. 5.6.

6

Analysis of the $^3He\,\pi^0\pi^0$ Reaction

The present chapter is dedicated to the necessary steps to arrive at final results. On top of the preselection of data presented in the previous chapter, a more detailed selection is performed. To better understand the data and thus the demands we will put on it, a Monte Carlo simulation is needed. Based on it, conditions on different observables are applied. In the last steps, a kinematic fit is carried out to fully identify the reaction events. Monte Carlo simulations are also relevant in order to do the corresponding acceptance and efficiency corrections to the data.

As mentioned in the previous chapter, data were taken in two different regimes: in direct *proton* − *deuteron* collisions and via quasi-free measurements in *deuteron* − *deuteron* collisions.

The first section of the chapter will describe the kinematics of each case. Further sections will present a detailed description of the selection of the events and of the kinematic fit.

6.1 Kinematics

As discussed in Sect. 5.1, the data for this work were obtained from different run periods under different conditions: direct production via *proton* − *deuteron* collisions, where ^{3}He ions and a π^0 pair are produced at a single incident energy and, more recently, measurements in the quasi-free regime, where the reaction of interest is produced in *deuteron* − *deuteron* collisions along with a spectator *neutron*, which influences the kinematics via Fermi motion.

In the $pd \rightarrow {}^3\mathrm{He}\pi^0\pi^0$ reaction the ^{3}He ions are ejected in the forward direction and detected in the FD of WASA. In Fig. 6.1 the kinetic energy of the ^{3}He versus the polar angle in the laboratory frame from simulation for the reaction $pd \rightarrow {}^3\mathrm{He}\pi^0\pi^0$ is plotted. The area limited by the black straight lines shows the FD acceptance.

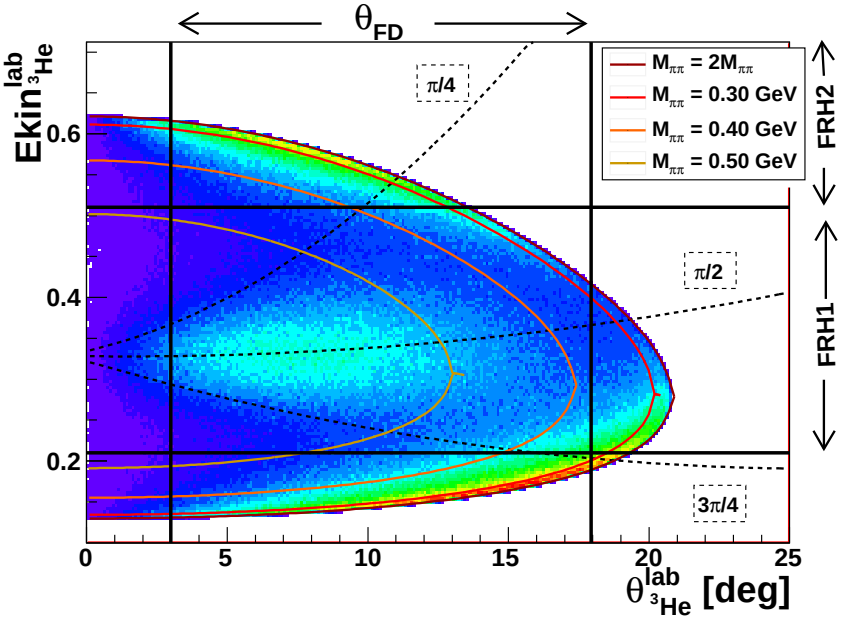

Figure 6.1: The plot shows the MC generated ABC model for $pd \rightarrow {}^3\mathrm{He}\pi^0\pi^0$ at $T_p = 1.0$ GeV. Particles with scattering angle outside the range from 3° to 18° cannot be detected by the FD. The ^{3}He ions with 210 MeV kinetic energy reach the FRH1 and with 510 MeV the FRH2. The ellipses show fixed $\pi^0\pi^0$ invariant mass values and the dashed lines correspond to different scattering angles of ^{3}He in the center of mass frame ($\frac{\pi}{4}$, $\frac{\pi}{2}$ and $\frac{3\pi}{4}$). The colors indicate the number of events from lower (dark blue) to higher (red)

This plot also includes information about the ABC effect. The points with fixed invariant mass of the $\pi^0\pi^0$ system are defined by colored ellipses around the center. Several fixed center of mass scattering angles of the ^{3}He are shown as radial dotted lines.

The neutral pions are reconstructed via their main decay branch $\pi^0 \rightarrow \gamma\gamma$ in the calorimeter of the CD, exploiting the short lifetime of the π^0's, of approximately 10^{-16} s.

When the reaction of interest is measured with deuteron beam and target the for-

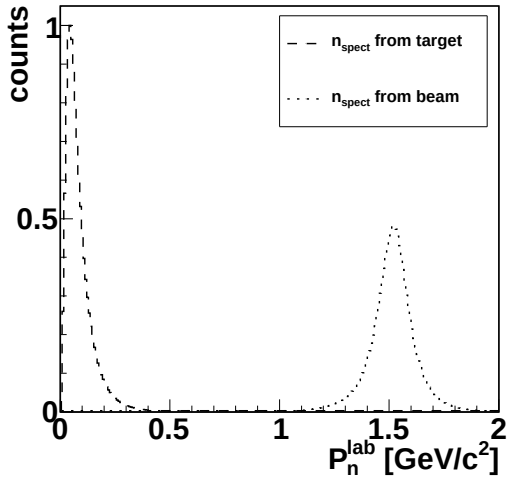

Figure 6.2: Momentum of the neutron spectator in laboratory frame for the cases where it is originated either from the beam (dotted line) or from the target (dashed line). The simulations are done for a deuteron beam with $T_{beam} = 1.7$ GeV ($P_{beam} = 3.044$ GeV/c)

mation of ^{3}He and two π^0 results from the collision of a proton from the beam or target with a deuteron from the other initial particle. The remaining neutron will be ejected. Depending on the role of this neutron one may observe a quasi-free reaction, where the neutron acts as spectator not taking part in the reaction, or a coherent reaction, where it is part of the final products:

- $dd \rightarrow (n)pd \rightarrow {}^3\mathrm{He}\pi^0\pi^0(n^{beam}_{spectator})$
- $dd \rightarrow dp(n) \rightarrow {}^3\mathrm{He}\pi^0\pi^0(n^{target}_{spectator})$
- $dd \rightarrow {}^3\mathrm{He}\pi^0\pi^0 n$

When the reaction proceeds via a quasi-free collision, the kinematics will be influenced by the Fermi motion of the neutron within the deuteron. The simulation of the Fermi momentum of the nucleons inside the deuteron is derived from the Hulthén wavefunction, which gives the momentum probability distribution:

$$|\phi^2| \propto [\frac{p \cdot (k^2 - \beta^2)}{(p^2 + \beta^2)(p^2 + k^2)}] \tag{6.1}$$

with p the momentum, $k = 0.26$ GeV/c and $\beta = 0.0456$ GeV/c [69]. Note that the use of the CD-Bonn potential [70] for the deuteron wavefunction gives practically identical results.

In the case of a quasi-free event two different cases will arise depending on the neutron spectator origin. In the laboratory frame this is identifiable as two well distinguishable distributions, see Sect. 6.2. If the neutron originates from the target, since it is at rest in the laboratory system, the spectator will have a low momentum, derived from equation (6.1). Otherwise, this Fermi momentum will add to that from the beam, which is half of the deuteron beam momentum for each nucleon.

6.2 Experiment Settings: Threshold Simulation

Due to the fact that no dedicated experiment was prepared for this work, the trigger settings during the experimental runs are a crucial point for the simulation and the analysis as well. The trigger condition on the ^{3}He ions was the same for all experimental runs: it requires a track in forward direction, with matching sectors in both layers of FWC, FTH1 and FRH1. The accepted events were demanded to have a high energy deposition in at least one of the FWC layers and also in the FRH1. Thus, for each element of the mentioned detectors a threshold on the signals was set.

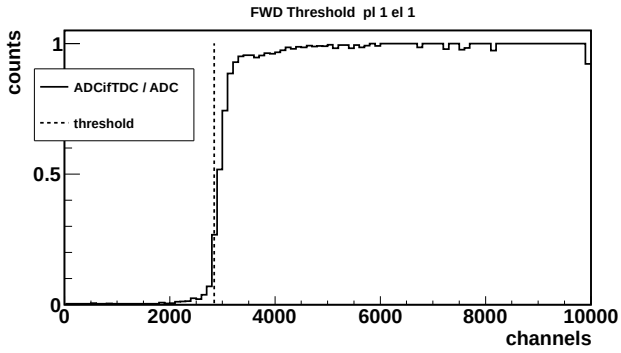

Figure 6.3: "ADC if TDC"/ADC spectra: normalized number of counts with TDC per ADC channel for an element of FWC1. The line shows the approximated ADC value for which the TDC is present, i.e., the threshold.

The thresholds work in such a way that only for signals above a certain value of the amplitude (related to the energy of the event) the TDC value will be recorded. By

looking at the ADC spectra if a TDC signal is present for each element in a detector plane, this is, the normalized number of counts with TDC per channel, one can calculate the corresponding thresholds for each element as seen in Fig. 6.3.

The thresholds can be recalculated in terms of deposited energies and that way be included in the analysis as limiting values for the Monte Carlo reconstructed events to mimic the data and have reliable simulations for further steps in the analysis.

Thresholds have a drastic effect on the measurement as one can see in the Fig. 6.4. Here a MC simulation for the reaction $dd \rightarrow {}^3\mathrm{He}\pi^0\pi^0(n_{spect})$ at $T_d = 1.7$ GeV is presented, the lines show the calculated threshold in terms of deposited energy for the limiting angles in FD acceptance.

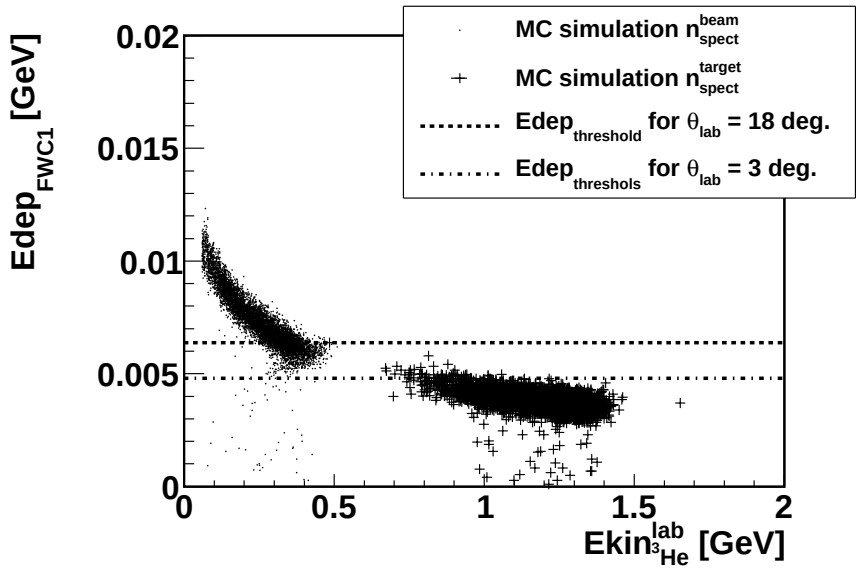

Figure 6.4: Deposited energy in FWC1 vs kinetic energy of ^{3}He for MC simulated events of the $dd \rightarrow {}^3\mathrm{He}\pi^0\pi^0(n_{spect})$ reaction at $T_d = 1.7$ GeV. The dashed dotted line corresponds to the calculated threshold in case the scattering angle is $\theta_{lab} = 3°$. Dashed line corresponds to scattering angle $\theta_{lab} = 18°$

The FWC and FRH threshold values were recalculated in terms of deposited energies for single detector elements and applied during the selection stage. This was done for both quasi-free measurements. The effect is so drastic that leaves the case of n_{spect}^{target} with insufficient statistics to be studied, as well as the December 2007 data ($T_d = 1.4$ GeV) for which no results where calculated in view of the scarce data left.

6.3 Selection of the $pd \rightarrow {}^3\mathrm{He}\pi^0\pi^0$ Reaction

Given the variety of scenarios for the reaction to be investigated a common frame of basic criteria was prepared. For this aim, conditions on deposited energy, number of tracks in FD and CD and others were applied. The purpose is to reduce the statistics to only events of interest for this study. Subsequently a more detailed processing of the events is done.

In general all events are required to have:

- 4 neutral CD tracks
- 1 or more FD tracks

Additionally, the tracks are requested to be within the WASA acceptance and have reasonable deposited energies. Since the FRH is used for the kinetic energy reconstruction, FD tracks must reach at least the first layer of the FRH. Stopping planes and more complex requirements are contained in the last steps. All the selection demands are summarized in Appendix 9.1.

In the case of the 2010 data, *graphic cuts* in the $\Delta E - \Delta E$ plots are applied around the ^{3}He band. This means that for a given histogram a limiting region is defined by eye and only hits inside it are accepted, see Sect. 6.5. This is done for all possible $\Delta E - \Delta E$ combinations [1].

After the pions have been selected (see Sect. 6.3.1 below), all charged tracks in the FD are considered to be ^{3}He particles. Their kinetic energy needs to be reconstructed and then the magnetic field correction is performed.

To reconstruct the kinetic energy, tables with Monte Carlo simulations for the energy losses of ^{3}He in different layers of the FD are used. The reconstruction routine can be found in Sec. 5.9.

At the end of the analysis the system is fully identified and the Lorentz vectors for the events are saved for a further processing with the kinematic fit described in Sect. 6.4. The plots in Fig. 6.6 show the ^{3}He band in the $\Delta E - \Delta E$ plot after all selection has been applied as well as the plot of the kinetic energy of the Helium versus its scattering angle in comparison to the MC simulation with the ABC model. Also, the

[1] They correspond to the deposited energy plots for FRH combinations: FRH1 vs FRH2, FRH2 vs FRH3, FRH3 vs FRH4 and FRH4 vs FRH5.

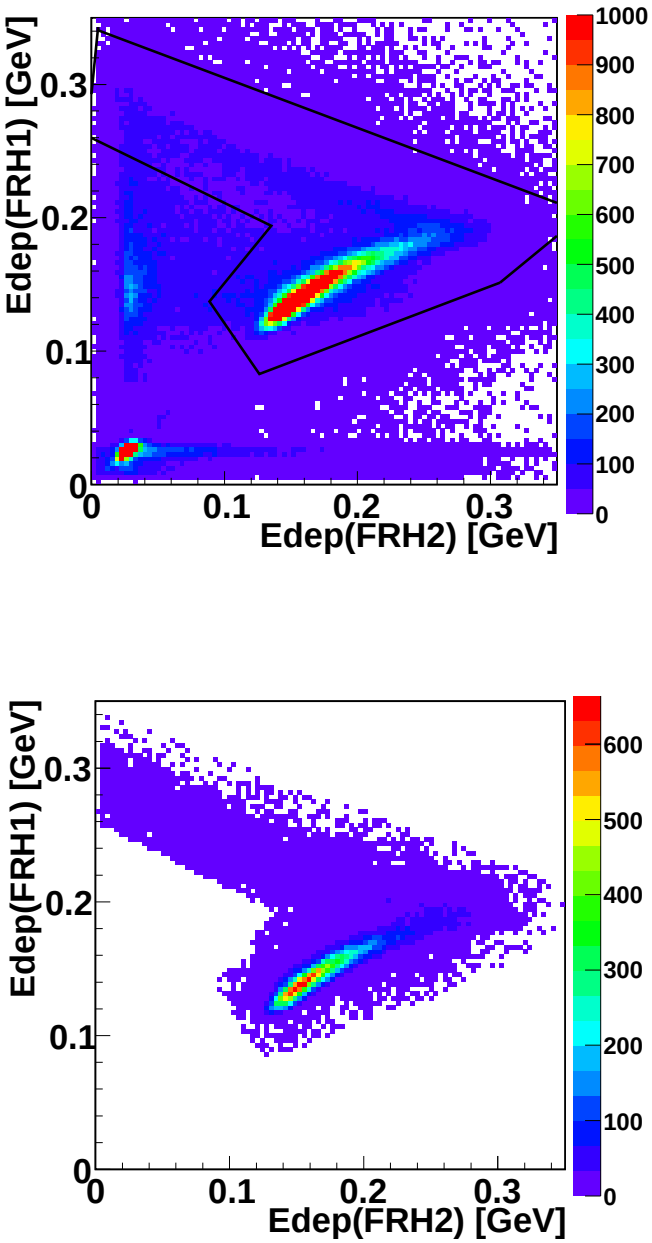

Figure 6.5: Deposited energies in FRH1 vs FRH2 for $T_d = 1.7$ GeV data. **Top**: The black line corresponds to the implemented graphic cut. **Bottom**: In addition to the basic selection the graphic cut has been applied.

missing mass of ^{3}He$\pi^0\pi^0$ can be used to check the selection, especially in the quasi-free process, where it should peak at the mass of the extra neutron involved in the reaction. An additional demand can be put in the right top plot in Fig. 6.6 to take only events closer to the peak. The plots on the bottom in Fig. 6.6 show the kinetic energy of the Helium versus the scattering angle in the laboratory frame. The gaps in the data plot (bottom left) correspond to the energy boundaries between FRH layers, while the gap between n_{spect}^{target} and n_{spect}^{beam} in the MC plot (bottom right) is due to the absence of the $dd \rightarrow {}^3\text{He}\pi^0\pi^0 n$ coherent simulation, which can be seen in the data plot (bottom right).

6.3.1 $\pi^0\pi^0$ Selection in the CD

After the basic selection has been done, the next step in the analysis chain is to reconstruct $\pi^0\pi^0$ events.

All neutral tracks in CD are combined into pairs to check the π^0 candidates. The recombination algorithm accepts up to 10 neutral tracks and checks the best pairs by comparing to the pion mass. The invariant mass of all the combined pairs should peak at about the π^0 mass. Monte Carlo simulation is performed to match the resolution of the peak for the given experiment, see Fig. 6.7a. With no further selection requirements the distributions of the pairs will exhibit a large background, this is clearly seen in the two-dimensional plot of the mass of one gamma pair versus the other one, Fig. 6.7b.

A distance defined as:

$$distance^2 = \sum_{i,j}(M_{\gamma_i\gamma j} - M_{\pi^0})^2 \tag{6.2}$$

is used to reduce the background. The distance squared from MC and data can be seen in Fig. 6.8. Only pairs for which the distance squared is less than a given value are accepted as good combinations, resulting in the selection of the pairs with the closest value to the π^0 mass, see Fig. 6.9.

6.4 Kinematic Fit

Next, the Lorentz vectors of the events saved in the previous steps have to be checked for kinematic requirements from momentum and energy conservation. This is done by a kinematic fit based on the least-squares method with constraints in the

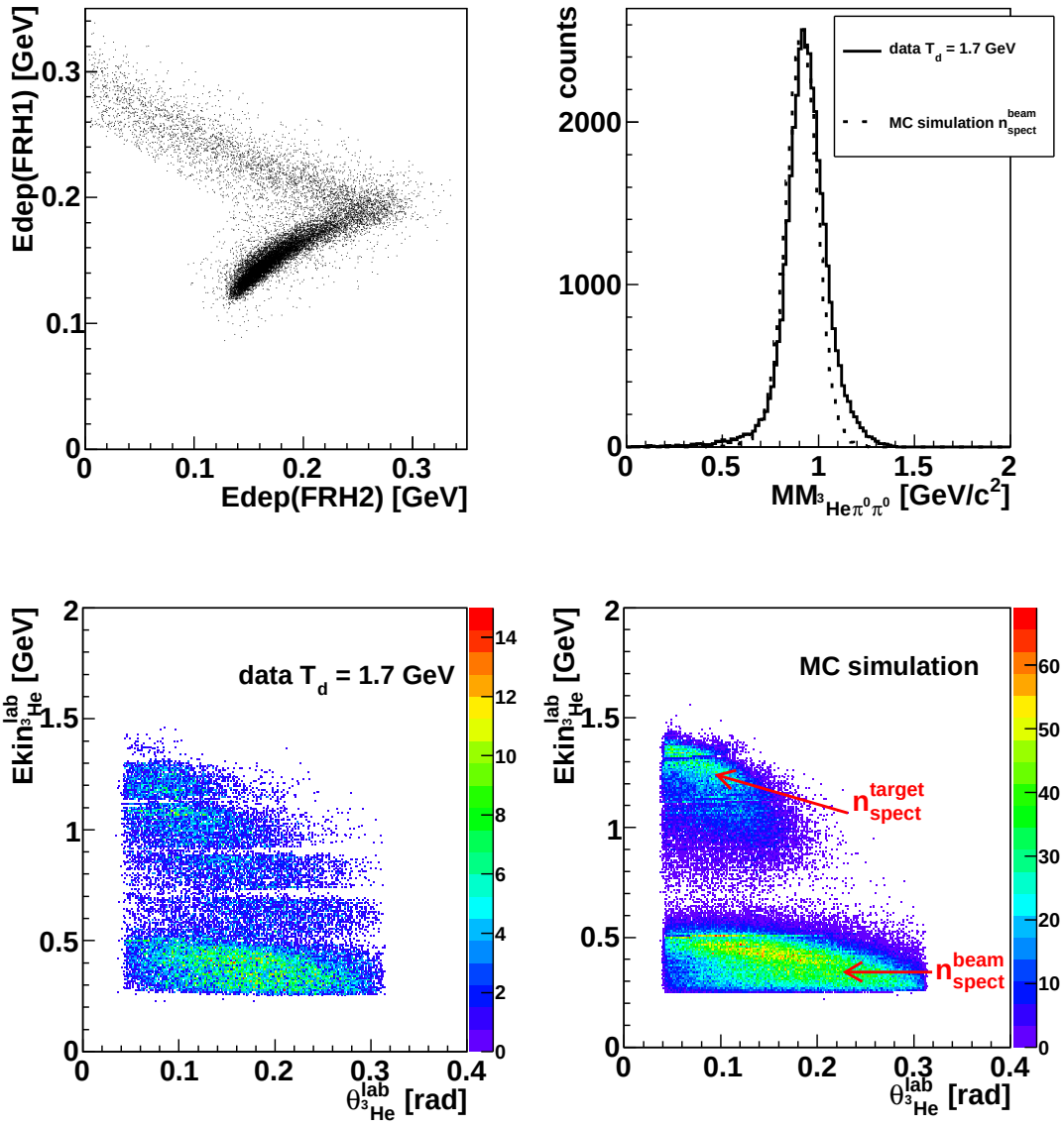

Figure 6.6: **Top**:**Left**:$\Delta E - \Delta E$ plot for ^{3}He in FD after the selection process (experimental data). Background events have been strongly reduced. **Right**:Missing mass of $^3\mathrm{He}\pi^0\pi^0$. The plot shows data (solid line) compared to MC (dotted line) simulation for neutron spectator from the beam. The distributions peak at the mass of the neutron. **Bottom**: Kinetic energy of ^{3}He vs. scattering angle in the laboratory frame for data (**left**) and MC simulation (**right**). The data corresponds to *dd* collisions with $T_d = 1.7$ GeV and the MC simulations are for the same reaction with neutron spectator. The gaps in the data plot correspond to the energy boundaries between the FRH layers.

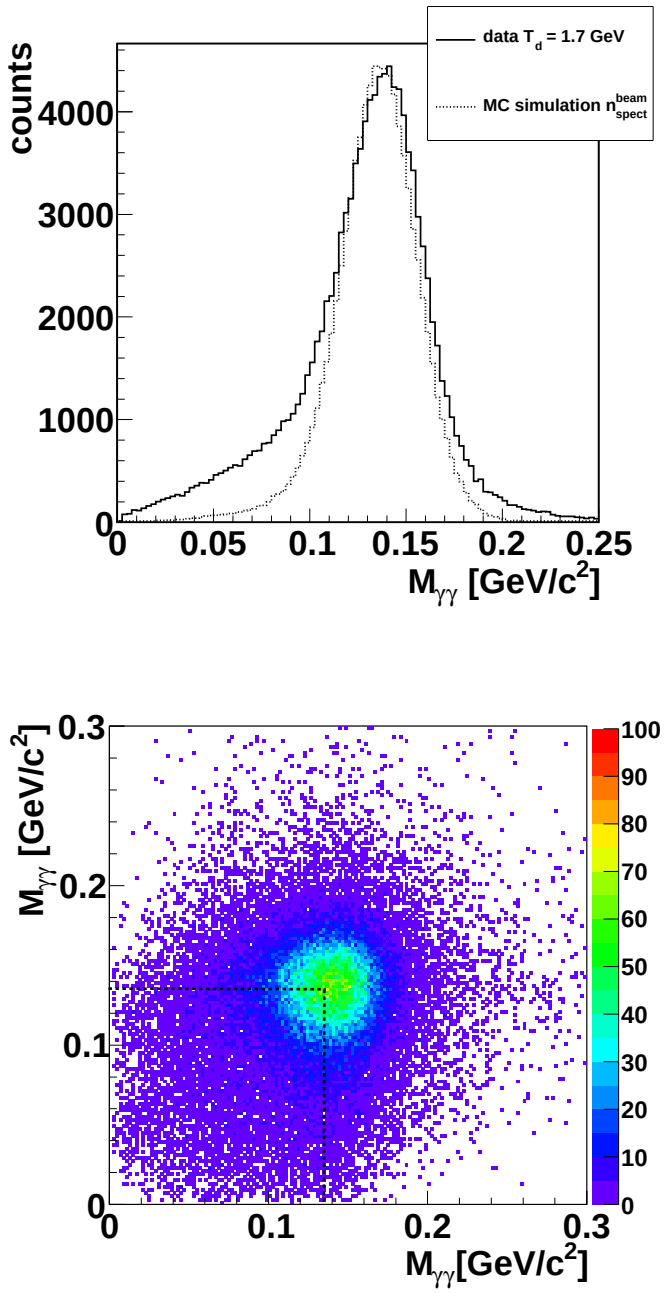

Figure 6.7: **Top**: invariant mass of all combinations of gamma pairs. The solid line corresponds to data and the dotted line to MC simulation. **Bottom**: two-dimensional plot of the invariant mass of one gamma pair versus the other one. The plot peaks at about the $\pi^0\pi^0$ position. The pion mass, m_{π^0}, is shown by the dashed lines.

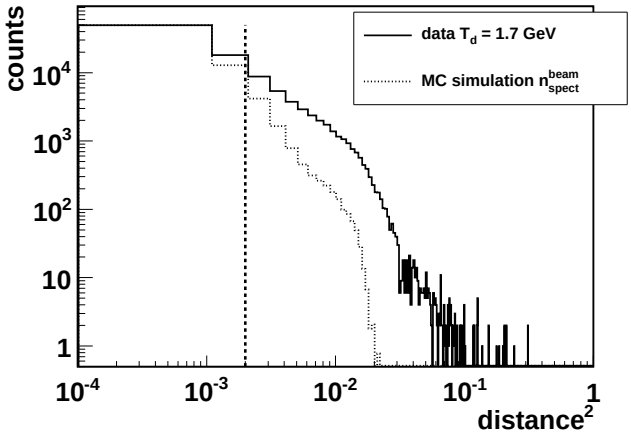

Figure 6.8: Distance squared distribution of the recombined gamma pairs into pion (note the double logarithmic scale). Data (solid line) and MC simulation (dotted line) are shown together with the selection condition (dashed line). Only events to the left of the vertical line are accepted.

form of Lagrange multipliers, as described in Ref. [71]. The goal of the kinematic fit is to improve the resolution of the measured kinematical values and, in addition, to reduce possible sources of background. The basic idea of this method is to vary the measured observables within uncertainties to fulfill the kinematic constraints of the reaction, in the form of energy and momentum conservation. The algorithm used in WASA-at-COSY is described in Ref. [72]

The χ^2 distribution of the fit will be a function of the number of degrees of freedom as long as the errors are Gaussian. The number of degrees of freedom is a function of the number of measured and unmeasured variables and the number of constraints.

In the Tab. 6.1, a summary of the kinematic fit characteristics based on the different reactions is shown. In the case of $pd \rightarrow {}^3\mathrm{He}\pi^0\pi^0$ at $T_p = 1.0$ GeV the kinetic energy of the ^{3}He was set as unmeasured because of the lack of a proper calibration for the FRH[2]. The number of degrees of freedom (N) can be calculated with the formula:

$$N = 4 + n_c - n_u \tag{6.3}$$

The measured values are the kinetic energies, polar angle θ and azimuthal angle ϕ of

[2]The data was devoted to η studies and thus only the first layer of the FRH had been calibrated.

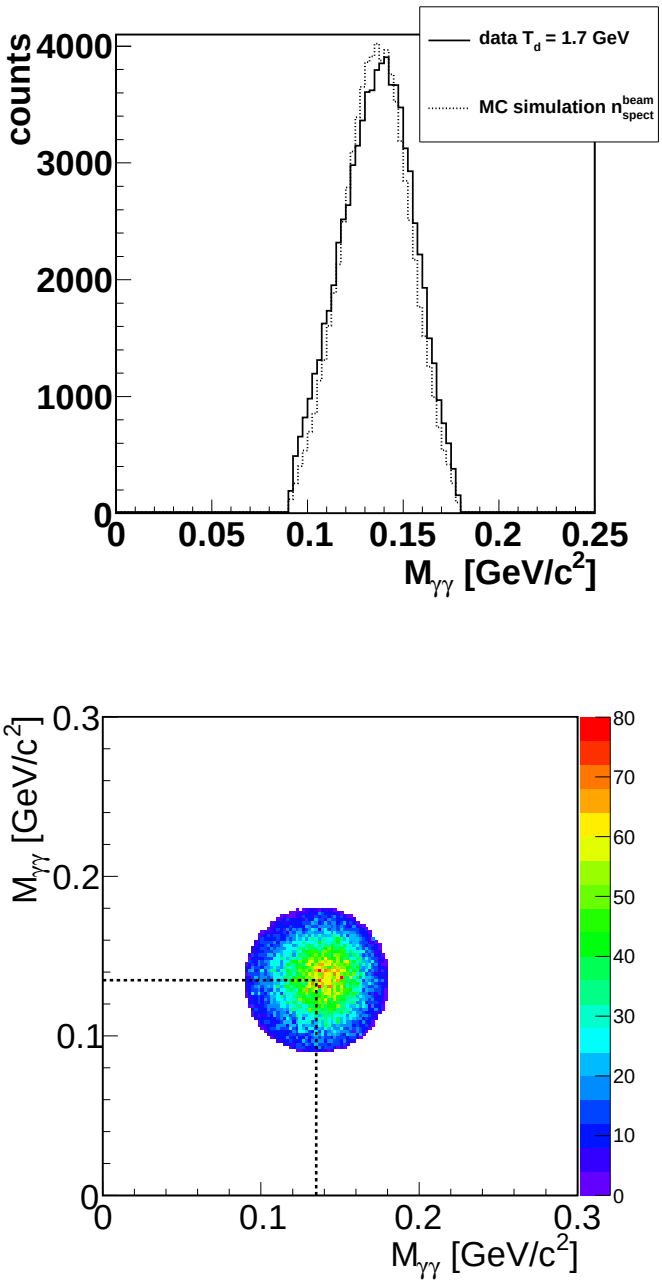

Figure 6.9: Top: invariant mass of all gamma pairs that pass the distance condition. The black line corresponds to data and the dashed one to MC simulation. **Bottom**: two-dimensional plot of the invariant mass of one gamma pair versus the other after they pass the distance condition. The value of the pion mass, m_{π^0}, is shown by the dashed lines.

^{3}He and gammas. Four constraints are related to the energy-momentum conservation, n_c corresponds to the number of constraints applied and n_u represents the number of unmeasured variables. Here, the constraints are set in the gammas, since each gamma pair is required to have $M_{\gamma\gamma} = M_{\pi^0}$.

reaction	constraints	Unmeasured values	No. deg. of freedom
$dd \rightarrow {}^3\mathrm{He}\pi^0\pi^0 n$	$M_{\gamma\gamma} = M_{\pi^0}$: **2**	neutron spect. (P_x, P_y, P_z) : **3**	3
$pd \rightarrow {}^3\mathrm{He}\pi^0\pi^0$	$M_{\gamma\gamma} = M_{\pi^0}$: **2**	Ekin ^{3}He: **1**	5

Table 6.1: Summary of the constraints and degrees of freedom for the kinematic fit.

6.4.1 Error Parameterization

For each of the measured values, $(Ekin, \theta, \phi)$, there are associated errors which depend on the particle type. A set of MC simulated single-track events of ^{3}He and photons are generated matching the experimental resolution. Then the errors are parameterized as:

$$\begin{aligned} \Delta(E) &= \frac{E_{true} - E_{rec}}{E_{rec}} \\ \Delta(\theta) &= \theta_{true} - \theta_{rec} \\ \Delta(\phi) &= \phi_{true} - \phi_{rec} \end{aligned} \tag{6.4}$$

E denotes the kinetic energy in GeV, θ is the polar angle and ϕ the azimuthal angle in the laboratory system, both in degrees. The sub-indexes denote the generated events (true) and the reconstructed ones (rec) through the detector simulation. The kinetic energy is distributed in 25 MeV bins while the scattering angle is plotted in 1° in the FD and 5° in the calorimeter. In Figs. 6.10 and 6.11 one can see the different distributions against the other variables for ^{3}He and photons respectively.

The structures in the distribution of the true minus reconstructed values of the kinetic energy per reconstructed kinetic energy are due to the FRH layer boundaries. For particles punching through one layer to the next, the reconstruction algorithm for the kinetic energy has a large uncertainty due to the difficulty to separate stopping and punching through events which are very close in energy deposition. In the case of the distributions of the polar angle for photon tracks, the large uncertainties correspond to the transition areas between the three differentiated parts in the SEC.

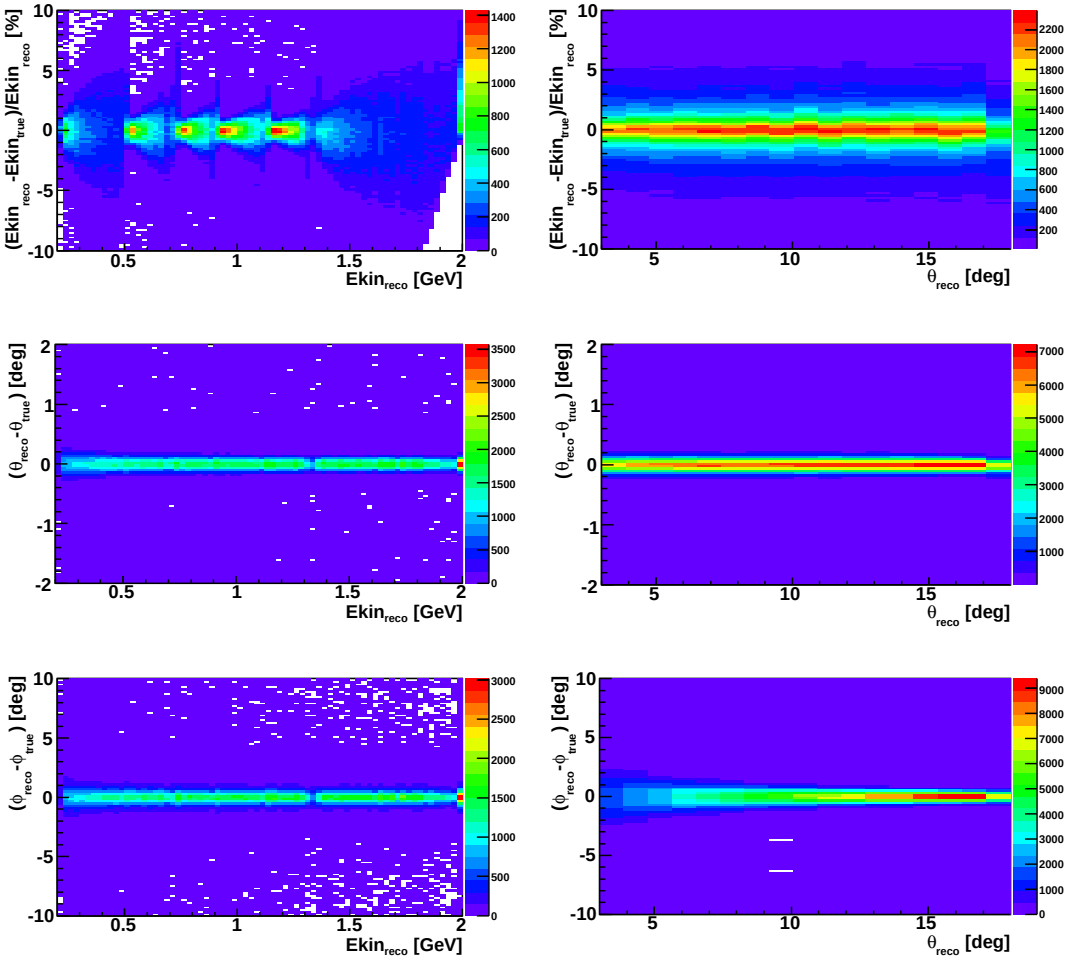

Figure 6.10: Error distributions according to equations (6.4) for kinetic energy (upper row), polar angle θ (middle row) and azimuthal angle ϕ (bottom row) for Monte Carlo simulation of single ^{3}He tracks as a function of the kinetic energy (left column) and the polar angle (right column). On the top-left figure, the vertical structures appear due to the layer design of the FRH.

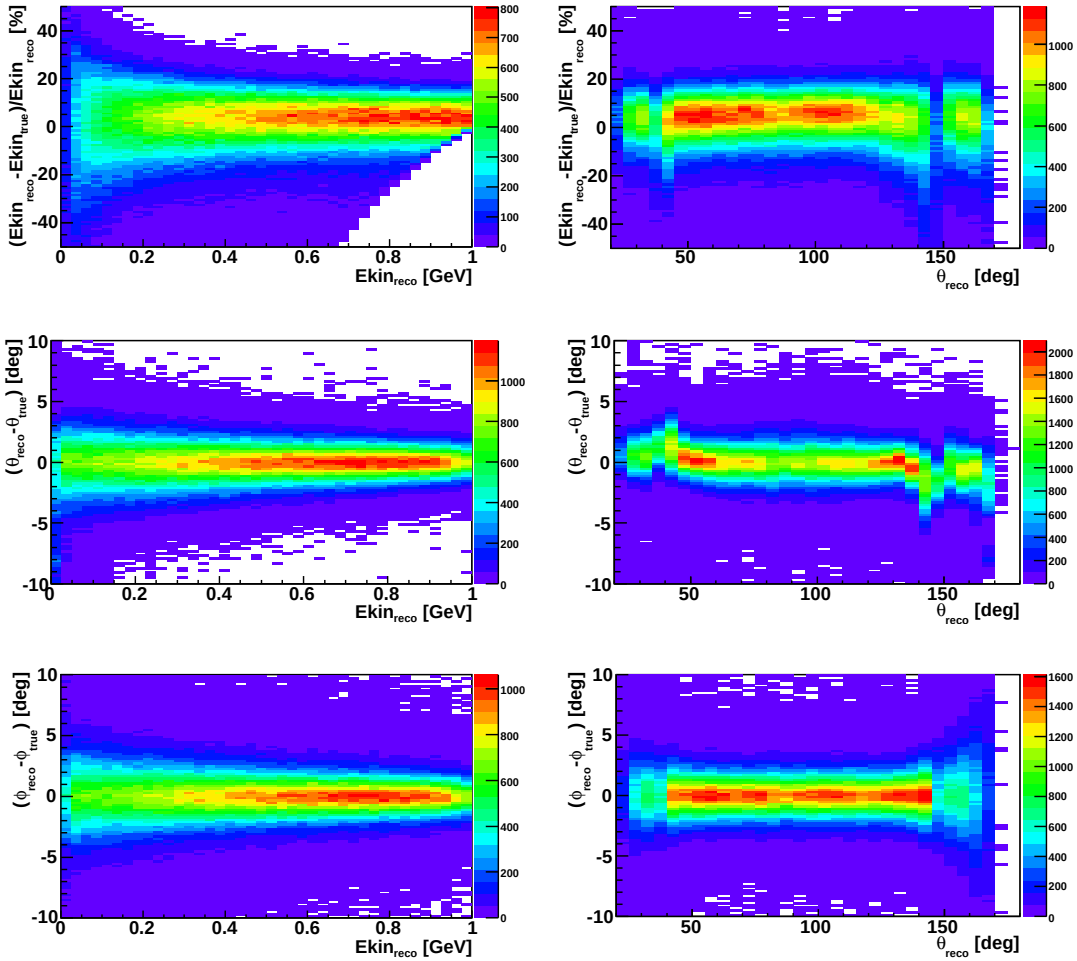

Figure 6.11: Error distributions according to equations (6.4) for kinetic energy (upper row), polar angle θ (middle row) and azimuthal angle ϕ (bottom row) for Monte Carlo simulation of single photon tracks as a function of the kinetic energy (left column) and the polar angle (right column).

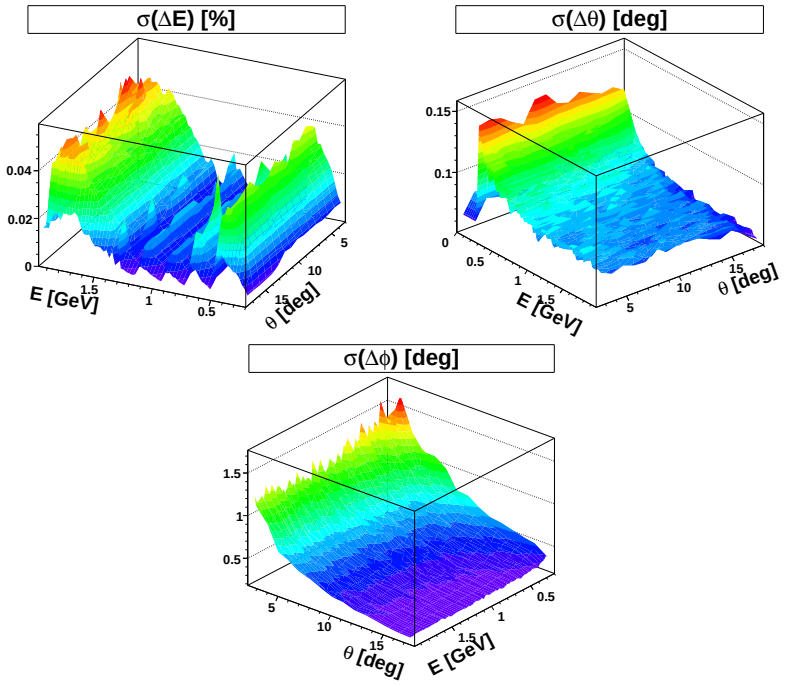

Figure 6.12: Error parameterization for ^{3}He.

To extract the errors, the distributions are fitted to a Gaussian for each energy and θ bin. The σ of the fit is treated as the error of the variable, i.e. $\sigma(\Delta E)$, $\sigma(\Delta\theta)$, $\sigma(\Delta\phi)$. The resulting errors for FD and CD tracks are shown in the Figs. 6.12 and 6.13 in two-dimensional plots.

6.4.2 Kinematic Fit: Results

The goodness of the fit can be checked with the χ^2 probability, which is defined, for N degrees of freedom, as [72]:

$$P(\chi^2|N) = \frac{\mathrm{e}^{-\frac{1}{2}}}{\sqrt{2^N\Gamma(\frac{1}{2}N)}} \int_{\chi^2}^{\infty} \mathrm{t}^{\frac{1}{2}(N-1)}\mathrm{dt} \tag{6.5}$$

This function, by definition, should be uniformly distributed between zero and one. Any deviation could be due to the fact that the errors are not Gaussian, the presence of background or a wrong estimation of the errors. When the errors are not Gaussian, usually, the result is a probability distribution which presents a strong enhancement about zero. In the plot 6.14 the χ^2 and probability distributions are presented for

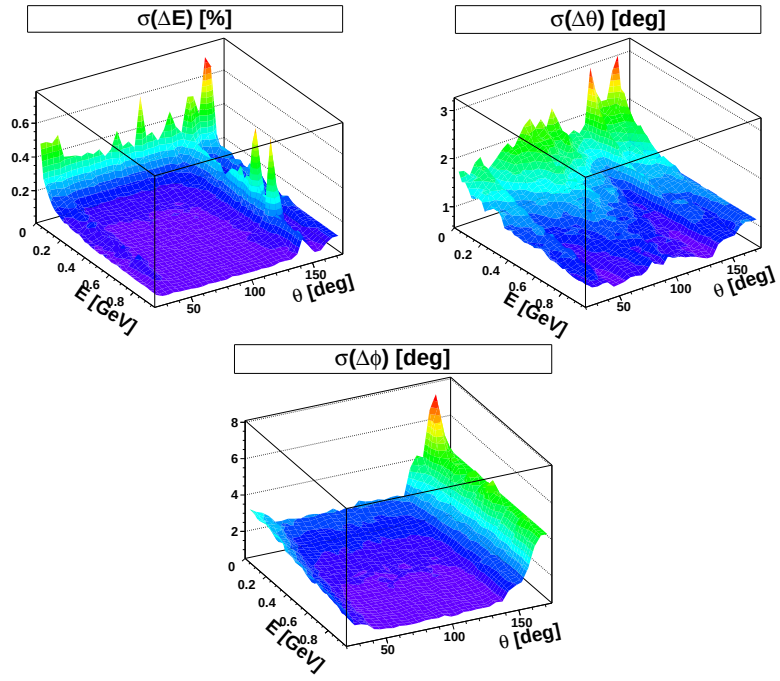

Figure 6.13: Error parameterization for photons.

both reactions: $dd \rightarrow {}^3\mathrm{He}\pi^0\pi^0(n^{beam}_{spect})$ and $pd \rightarrow {}^3\mathrm{He}\pi^0\pi^0$, for both data and MC simulations.

The most characteristic feature is the fact that the χ^2 function, see Figs. 6.14a and 6.14c, in the case of experimental data, does not peak at the theoretical prediction and exhibits a long tail. A possible explanation can be given in terms of *rest gas* contribution. The rest gas is just evaporated gas from the frozen hydrogen or deuterium pellets still present in the interaction region. This affects the interaction vertex position in the beam direction and leads to events with a reconstruction efficiency and resolution different from that for the events originating from the main vertex position at (0, 0, 0). The calculation of this contribution to the data is done by using tracking informations from the MDC. A description of the method can be found in Refs. [73, 74].

Unfortunately there is no vertex information from SEC, which is used in this thesis to measure the photons from the π^0 decay. Since the χ^2 distribution also exhibits long tails mainly due to background and misidentified events during the kinematic fit, the estimation of the rest gas contribution from this distribution is not accurate. Nevertheless, as mentioned before, the rest gas can explain the shift in the peak position

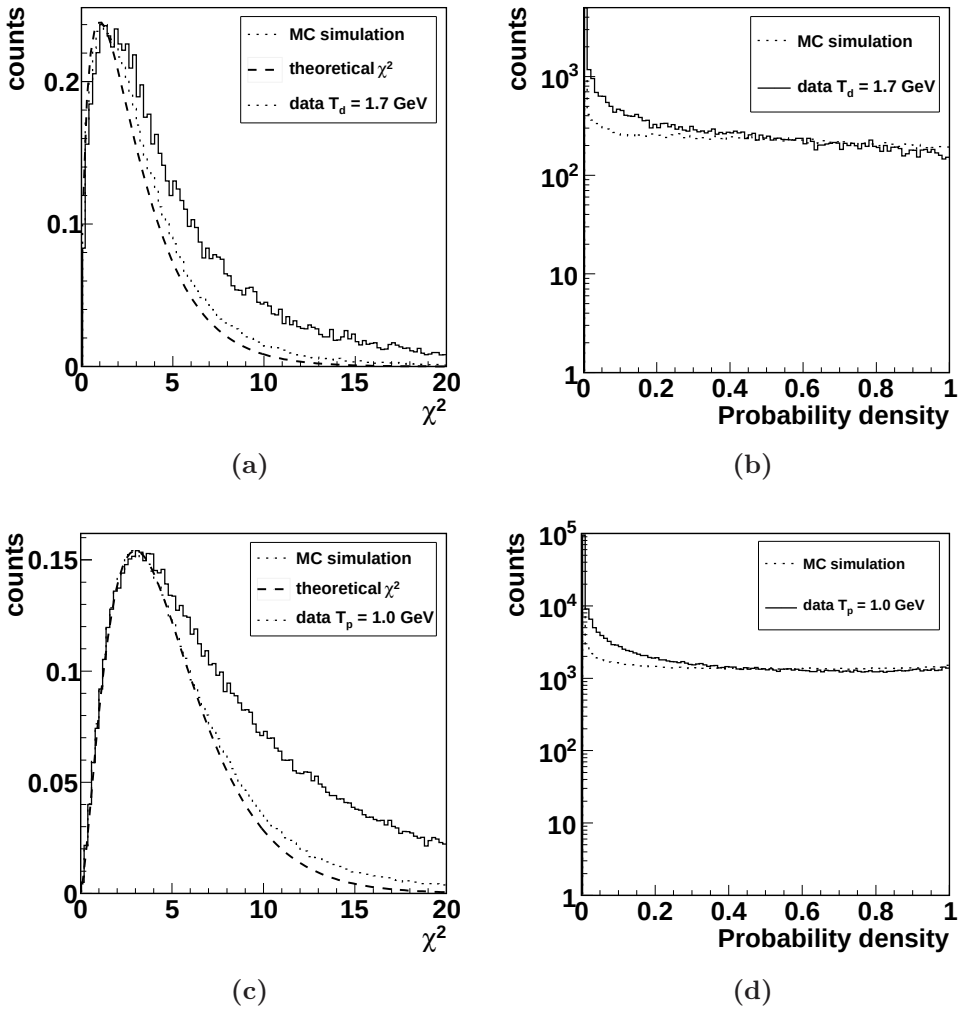

Figure 6.14: χ^2 (**left**) and probability $P(\chi^2|N)$ (**right**) distributions (note the log scale) for $dd \to {}^3\mathrm{He}\pi^0\pi^0(n_{spect})$ (**top**)and $pd \to {}^3\mathrm{He}\pi^0\pi^0$ (**bottom**) for data (solid line) and MC (dotted line). The dashed lines correspond to the theoretical χ^2 distributions for the adequate number of degrees of freedom.

and partly the long tails present in the data. Therefore, MC simulations were prepared, where 100% of the events were originating from this residual interactions and then the χ^2 distributions were fitted with a function like:

$$f(\chi^2_{experiment}) = c_1 \cdot \chi^2_{\mathrm{MC}} + c_2 \cdot \chi^2_{\mathrm{RS}} \tag{6.6}$$

where χ^2_{MC} corresponds to the calculated distribution for MC simulation with all events originating at (0, 0, 0) and χ^2_{RS} is the one with all events from the gas interaction. The percentage of each can be associated to the fit coefficients since $c_1 + c_2 = 100\%$. The results are presented in the Fig. 6.15. The fits show that the rest gas contribution to some extent may account for the shift in the data but it is not the only effect included in the distributions. Hence, it cannot be used as a good estimation of the amount of rest gas contribution. Instead, values from other works, e.g. see Ref. [73], where the rest gas contribution has been calculated to be of about 20% of the total experimental statistics were used. For this reason the rest gas is included as a source of systematic uncertainties.

6.5 Quasi-free Reaction: Selection of the Neutron Spectator

In the case of the quasi-free reaction with a neutron spectator generated from the beam, an extra selection needs to be done. During the kinematic fit the neutron is reconstructed from the initial and final system and treated as an unknown variable in the process. Additional conditions on its observables can be demanded in order to fully identify the reaction.

The three different situations described in Sect. 6.1 are clearly seen in the momentum distribution of the reconstructed neutron in the laboratory frame, see Fig. 6.16a. Here we can observe three distinct areas that correspond to the three mechanisms: the two spectator cases plus the coherent reaction.

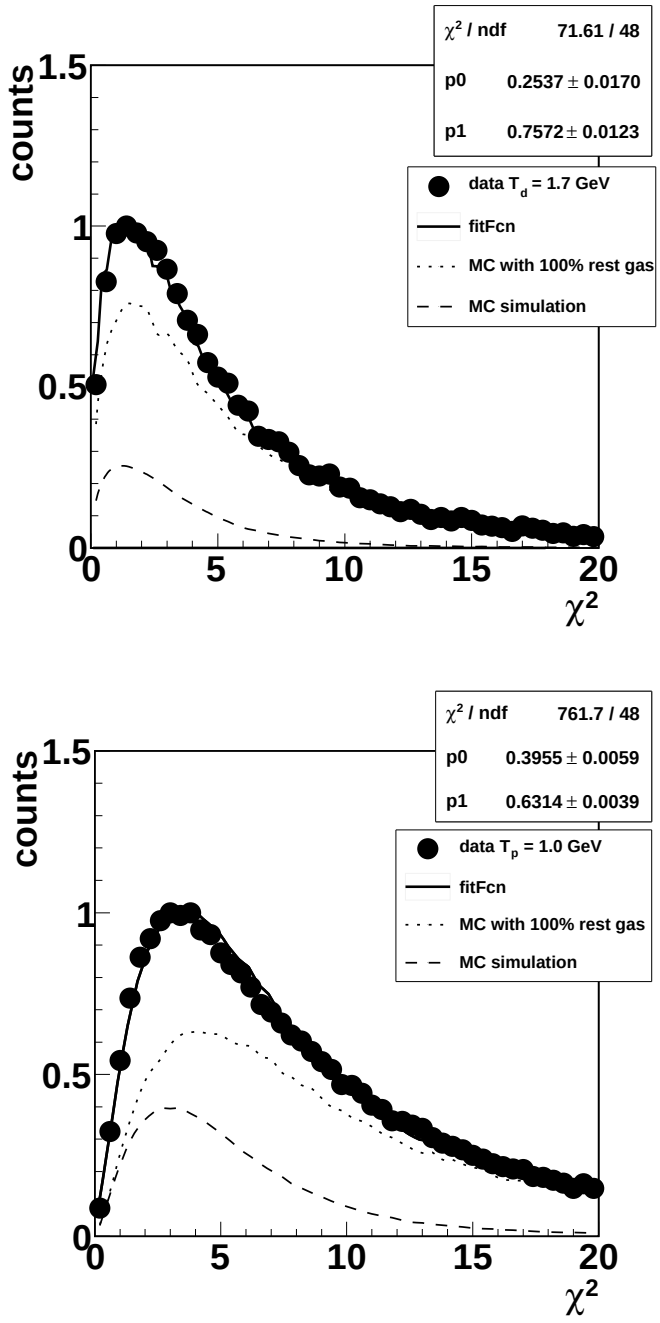

Figure 6.15: Rest gas estimation. **Top**: Experimental χ^2 distribution for the reaction $dd \rightarrow {}^3\mathrm{He}\pi^0\pi^0(n^{beam}_{spect})$ (black solid circles). **Bottom**: Experimental χ^2 distribution for $pd \rightarrow {}^3\mathrm{He}\pi^0\pi^0$. The dashed line shows the fit described in eq. (6.6)

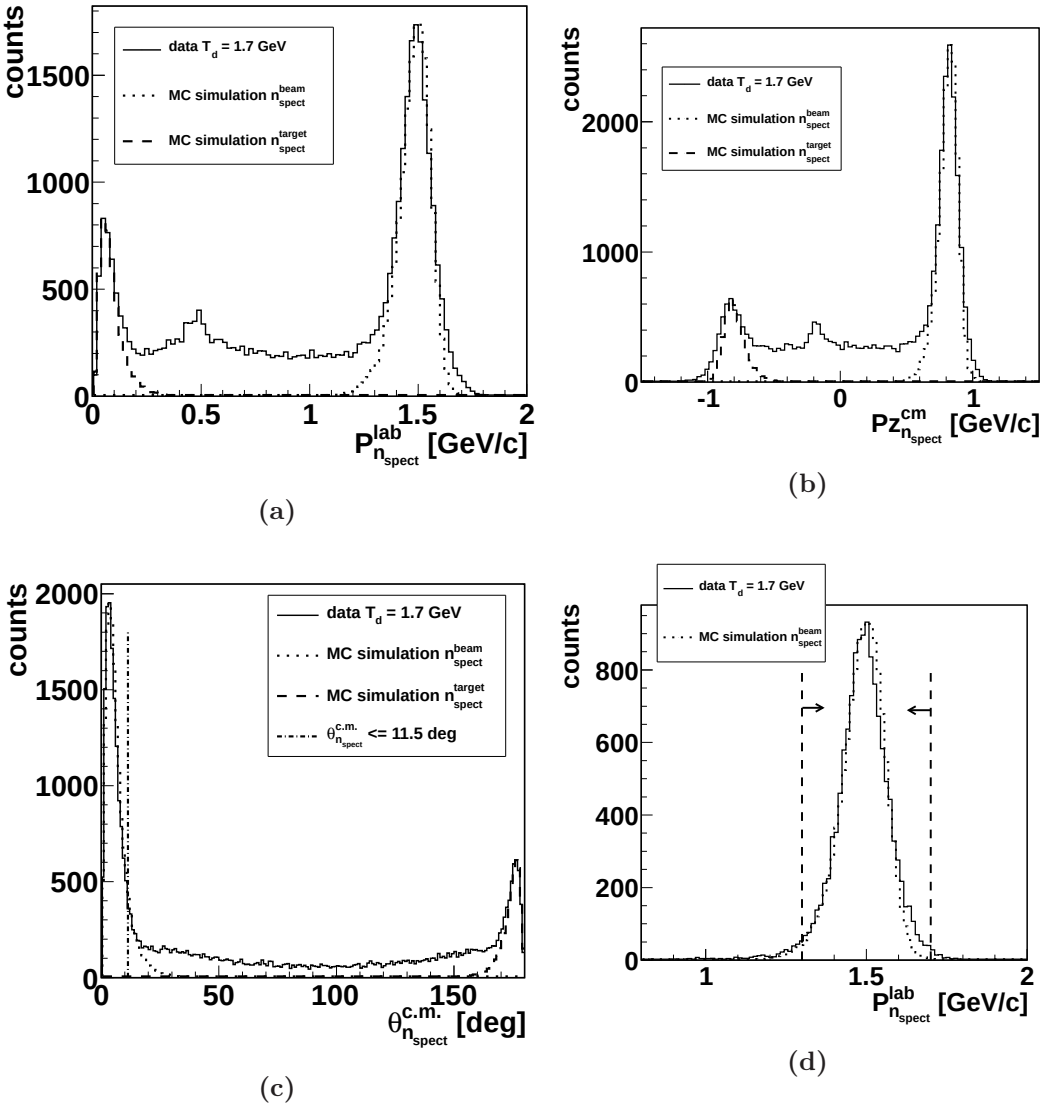

Figure 6.16: Top left: Momentum of the reconstructed neutron in the laboratory frame. **Top right**: Z-component of the momentum of the reconstructed neutron in the c.m. frame. **Bottom left**: Polar angle of the reconstructed neutron in the c.m. frame. **Bottom right**:Selection on the momentum of the reconstructed neutron. The vertical lines correspond to the different demands applied to the data. Arrows show the accepted region. In the plots we see data (solid line) and MC simulations for the neutron originating from the target (dashed line) and from the beam (dotted line).

Because of the spectator nature of the neutron a first selection can be applied on the angular distribution of the neutron. In the center of mass frame both spectator cases are opposite in direction. In one case the neutron scatters in forward direction with a very small angle and in the other it is emitted in the opposite direction with an angle close to 180°. In Fig. 6.16c we can see the scattering angle in the c.m. frame for the reconstructed neutron compared to that one from the MC simulations. Based on this simulation, the angle is required to be less than 11.5°. The remaining contribution from the coherent reaction is considered almost negligible.

A further demand on the momentum in the laboratory frame is done. Only events with 1.3 GeV/c $\leq P_{n_{spect}} \leq$ 1.7 GeV/c are accepted to assure that only data from the reaction $(n^{beam}_{spect})pd \rightarrow {}^3\mathrm{He}\pi^0\pi^0(n^{beam}_{spect})$ are taken. Fig. 6.16d shows this condition after the selection made on the scattering angle.

6.6 Efficiency and Acceptance Correction

Next the results are to be corrected for acceptance of the detector and the efficiency of the analysis. This is done in a single step by doing a one-dimensional correction of the histograms: each data bin of the measured histograms is divided by the efficiency-acceptance correction factor which is obtained as the ratio of the number of reconstructed over generated Monte Carlo events per bin:

$$\epsilon_{eff,acc} = \frac{MC_{reconstructed}}{MC_{simulated}} \tag{6.7}$$

When the full reaction phase space is covered by the detector, the corrections, done this way, are model independent. If this is not the case then the model needs to be as accurate as possible in describing the data. The correction done this way is considered a source of systematic uncertainties.

6.7 Normalization Reaction: $pd \rightarrow {}^3He\pi^0$

For the absolute cross section a normalization relative to the reaction $pd \rightarrow {}^3\mathrm{He}\pi^0$ has been chosen. The reaction is easy to select in both quasi-free and direct reactions

within the same analysis used for two-pion production[3], and there are reliable differential cross-sections available in the energy region of interest [75, 76]. The reaction is measured with the same settings as the main reaction of this work, and thus the relative normalization is straight forward.

The integrated cross section of a reaction can be obtained from the expression:

$$N_{exp} = \sigma \cdot L_{int} \cdot \epsilon_{eff,acc} \tag{6.8}$$

where N_{exp} is the number of reconstructed events after the analysis, σ is the total cross-section integrated over 4π, L_{int} the integrated luminosity and $\epsilon_{eff,acc}$ corresponds to the detection and reconstruction efficiency. When both reactions are measured simultaneously, as in our case, the luminosity is the same and nearly all inefficiencies cancel out. Then we can use the expression:

$$\frac{N_{corr}(pd \rightarrow {}^3\mathrm{He}\pi^0\pi^0)}{N_{corr}(pd \rightarrow {}^3\mathrm{He}\pi^0)} = \frac{\sigma(pd \rightarrow {}^3\mathrm{He}\pi^0\pi^0)}{\sigma(pd \rightarrow {}^3\mathrm{He}\pi^0)} \tag{6.9}$$

where $N_{corr} = N_{exp}/\epsilon_{eff,acc}$ as explained in the section before.

6.7.1 Cross-section calculation

From the measurements in Ref. [75] we know the differential cross-sections at different ^{3}He scattering angles in c.m. Since the measurements of these works were done for dp collisions, the scattering angles in the center of mass system are just mirrored compared to those of this work. The differential cross sections over the range of energies we are interested in are shown in Fig. 6.17a. There we can observe the dependence over the kinetic energy of the beam for 0° and 180° scattering angles of the ^{3}He ions in the center of mass frame. To the error bars in the figure an error of the 8% has to be added in quadrature due to the overall normalization.

This angular dependence can be also seen in the differential angular distributions of the Helium ions in center of mass frame, e.g. in the Fig. 6.17b from Ref. [76]. Knowing the differential cross sections, and by comparison to the angular distributions at $\theta_{^3\mathrm{He}^{c.m.}} = 0°$ from our analysis, see Fig. 6.18, the total cross section of the reaction $pd \rightarrow {}^3\mathrm{He}\pi^0\pi^0$ can be estimated.

[3] the CD selection is then limited to single pion events.

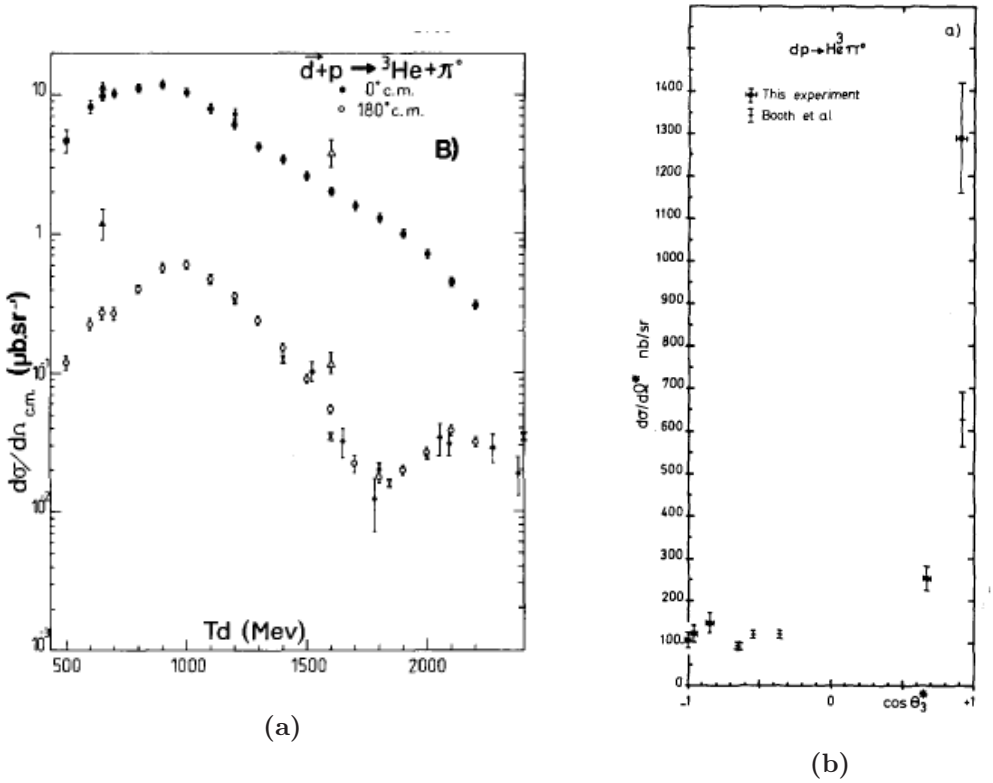

(a) (b)

Figure 6.17: Left:Differential cross-section from Ref. [75] at $\theta^{c.m.}_{^3\mathrm{He}} = 0°$ (solid symbols) and $\theta^{c.m.}_{^3\mathrm{He}} = 180°$ (open symbols) vs. the kinetic energy of the beam (note the logarithmic scale). **Right**: Angular distribution of the ^{3}He ions in the c.m. frame for $\sqrt{s} = 3.28GeV$ ($T_d = 1.5GeV$) from Ref. [76]

Assuming the flat angular trend we observe in Fig. 6.17b, the value at $\theta^{c.m.}_{^3\mathrm{He}} = 180°$ ($\theta^{c.m.}_{^3\mathrm{He}} = 0°$ in pd collisions) can be extended to the half hemisphere of the solid angle (i.e., $\theta_{^3\mathrm{He}^{c.m.}} \leq 90°$ in this work). The result is used to calculate the differential cross section for $\theta^{cm}_{^3\mathrm{He}} \leq 90°$ for $pd \rightarrow {}^3\mathrm{He}\pi^0\pi^0$ and thus the total cross section by extrapolating to the whole θ range.

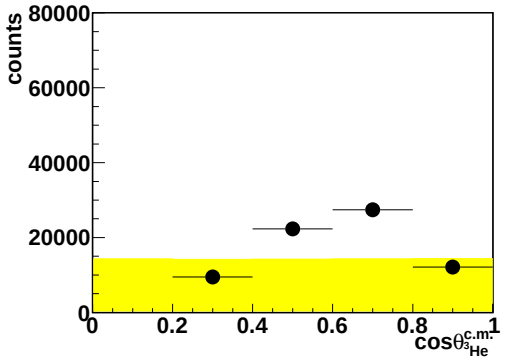

Figure 6.18: Differential cross section as a function of the scattering angle of ^{3}He in c.m. frame for $pd \rightarrow {}^3\mathrm{He}\pi^0$ at $\sqrt{s} = 3.416$ GeV measured in pd collisions at $T_p = 1.0$ GeV

To create the MC simulations for the $pd \rightarrow {}^3\mathrm{He}\pi^0$ reaction, the data from Ref. [75] were fitted to a polynomial of 5th order, see Fig. 6.19. The values of the fit parameters can be found in Tab. 6.2. The simulation reproduces only the differential cross section $\frac{d\sigma}{d\Omega}|^{c.m.}_{\theta=0°}$ but no other distributions.

Parameter	Value	Error
p_0	367.3	$5.877{\cdot}10^{-3}$
p_1	-151.3	$1.805{\cdot}10^{-3}$
p_2	-24.82	$5.423{\cdot}10^{-4}$
p_3	7.424	$1.598{\cdot}10^{-4}$
p_4	3.728	$4.622{\cdot}10^{-5}$
p_5	-0.783	$1.309{\cdot}10^{-5}$

Table 6.2: The values and errors of the parameters from the 5th order polynomial fit shown in Fig. 6.19

The selection of the $pd \rightarrow {}^3\mathrm{He}\pi^0$ reaction is very similar to the case of the double-pionic fusion. All basic cuts (see Appendix 9.1) are applied, with only a more demand-

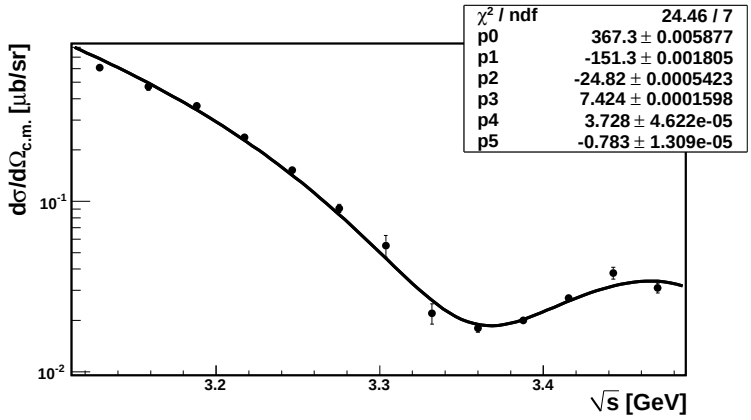

Figure 6.19: Parametrization of the differential cross section $\frac{d\sigma}{d\Omega}|^{c.m.}_{\theta=0^\circ}$ for $pd \to {}^3\mathrm{He}\pi^0$ in the energy range of the present work. Data have been taken from Ref. [75].

ing request: only two photons are selected in the CD.

Following the basic selection still a large background is left as can be clearly seen in the invariant mass of the two photons recombined to a pion, see Fig. 6.20. The origin of this large background contribution has two sources. One is our reaction of interest, the two pion production, which is responsible for the excess of events for small invariant-mass values, and of course the combinatorial background from the recombination to a pion, which smears the Gaussian distributions.

Reduction of the background was obtained by demanding the Helium ions and the recombined pion track to be coplanar, this is, the absolute difference in the ϕ angles of Helium and pion in the laboratory frame was demanded to be close to 180°. Fig. 6.21 shows the co-planarity selection and the resulting pion mass spectra.

The limited statistics in the case of the experimental data from the quasi-free reaction together with the lack of a fully consistent simulation motivated the decision of using the pd data at $T_p = 1.0$ GeV for the absolute normalization and then do a relative normalization of the quasi-free reaction to this single energy. The analysis of $dd \to {}^3He\pi^0(n_{spect})$ in the quasi-free regime was used as verification of the selection and analysis done in the single energy case.

As in the case of the main reaction, a kinematic fit was performed. In this case a single over-constraint was applied to demand the photon pair to form a pion.

For $\sqrt{s} = 3.416$ GeV ($T_p = 1.0$ GeV) a value of $\frac{d\sigma}{d\Omega}|^{c.m.}_{\theta=0^\circ} = 0.027 \pm 0.001$ μb/sr is

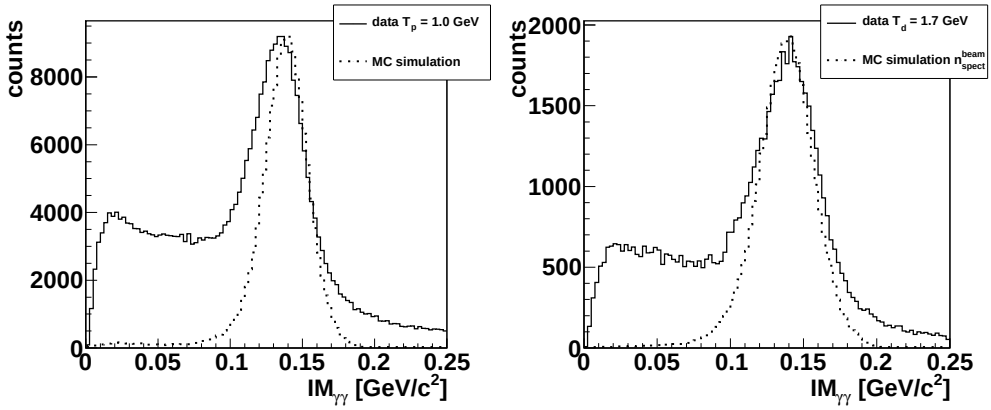

Figure 6.20: invariant mass of the gamma pair for single pion production. **Left**: The invariant mass of the gamma pair in the *pd* reaction at $T_p = 1.0$ GeV. **Right**: Invariant mass spectra for the quasi-free measurement at $T_d = 1.7$ GeV. The solid line corresponds to experimental data and dotted line to MC simulation.

taken. This leads to a total cross section value of $\sigma(^3\mathrm{He}\pi^0\pi^0) = 2.28 \pm 0.04$ (stat) $\pm$ 0.40 (sys) μb where the 8% error in the determination of the cross section in Ref. [75] has been included.

From the assumptions on the $^3\mathrm{He}\pi^0$ differential distributions and the method itself to calculate the cross section a 30% overall uncertainty has been estimated. This systematic uncertainty is not included in the presented values.

6.8 Uncertainty Estimation

The error of the cross section is given in terms of statistical and systematic uncertainties.

6.8.1 Statistical Uncertainty

The statistical errors are mainly due to statistical fluctuations of the count rate. The statistical absolute error of a variable X is given by:

$$\delta^{stat} X = \frac{X}{\sqrt{X}} = \sqrt{X} \tag{6.10}$$

All statistical errors are calculated according to the usual error propagation.

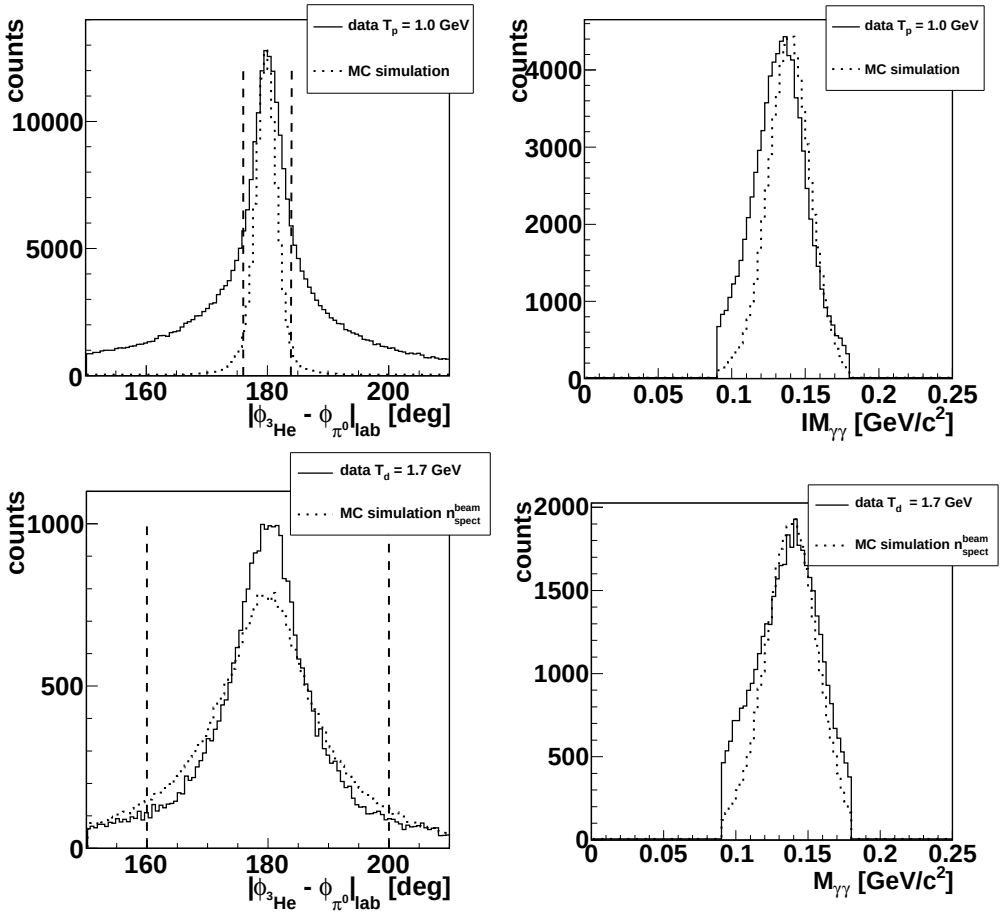

Figure 6.21: Left: Planarity cut for ^{3}He$-\pi^0$. The dashed vertical lines show the selection condition. **Right**: Invariant mass spectra after the planarity condition has been applied. The solid line corresponds to experimental data and dotted line to the MC simulation. The **upper** figures correspond to pd collisions at $T_p = 1.0$ GeV and the **bottom** figures to dd at $T_d = 1.7$ GeV.

6.8.2 Systematic Uncertainties

The main source of uncertainties corresponds to the different errors introduced by systematic effects. In the cross section calculation these errors have been estimated for the most influential sources. The most notable ones are: the cut on the probability density of the kinematic fit procedure, the influence of the acceptance and efficiency correction and the rest gas contribution.

In the case of the acceptance and efficiency correction (δ^{sys}_{MC}), the uncertainty is, quantitatively, the most influential in the total cross section value. This is due to the low acceptance for the backward going Helium in the c.m. system. By kinematics this situation corresponds to forward going pion pairs in c.m. The WASA acceptance is very low in this case because of the high probability of one of the photons from the pion decay being emitted in forward direction, where it cannot be detected. The systematic uncertainty from the acceptance and efficiency correction has been calculated to be as big as 15%.[4].

The condition on the kinematic fit probability also introduces an uncertainty (δ^{sys}_{χ}). Several cuts have been tested and the difference between the largest and lowest values of the cross section have been used to estimate a contribution of 4%.

As has been noted in previous sections, the rest gas contribution has been roughly estimated for this work, resulting in values highly deviating from other experiments with WASA-at-COSY. For this reason, a contribution of about 20% was taken as a good estimate for the simulations and included this effect as a source of uncertainties (δ^{sys}_{RS}). MC simulations were prepared to investigate the errors introduced by the rest gas estimation. Contributions ranging from no rest gas at all up to an improbable contribution of 60% were checked and the deviation between the most extreme cases taken as estimate for this uncertainty. The resulting systematic error is of about 7.5%.

The total systematic error is calculated by adding all these uncertainties in quadrature. To this the systematic uncertainty ($\delta^{sys}_{\sigma(\pi^0)}$) from Ref. [75] is included:

$$\delta^{sys}(\sigma) = \sqrt{(\delta^{sys}_{RS})^2 + (\delta^{sys}_{MC})^2 + (\delta^{sys}_{\chi})^2 + (\delta^{sys}_{\sigma(\pi^0)})^2} \tag{6.11}$$

[4]Numbers given in this section are for pd data at $T_p = 1.0GeV$. For the quasi-free measurement the values are discussed in Sect. 7.4.

7

Results

This chapter shows the results of the analysis of the reaction $pd \to {}^3\mathrm{He}\pi^0\pi^0$ via pd and dd collisions. The energy dependence of the total cross section as well as of the differential distributions will be presented and discussed in comparison with theoretical models.

7.1 ABC Resonance Model in $pn \to d\pi^0\pi^0$

Based on the previous results on the ABC effect with CELSIUS/WASA [26] and especially from the study of the basic reaction $pn \to d\pi^0\pi^0$ [10] with WASA-at-COSY a theoretical model was developed.

The model introduces a s-channel resonance (see Sect. 2.2), which decays into two Δs and subsequently into two nucleons and pion pairs. The two nucleons then fuse to a deuteron giving the following reaction scenario: $pn \to d^* \to \Delta\Delta \to d\pi^0\pi^0$. In this case the differential cross section is defined as:

$$d\sigma = \frac{(2\pi)^4}{4p_i\sqrt{s}}|M|^2 d\phi_3 \tag{7.1}$$

where $d\phi_3$ denotes the 3-body phase space, p_i the initial momentum of the beam and $\sqrt{s}$ the c.m. energy.

In a complete description of the process the d^* resonance amplitude is added to the amplitudes corresponding to the conventional t-channel production of the Roper resonance $N^*(1440)$ and the $\Delta\Delta$ system. But for the present reaction, $pd \to {}^3\mathrm{He}\pi^0\pi^0$, the Roper resonance was omitted, since it influences only the threshold region, which

is not fully covered by the present work. Furthermore, its amplitude is expected to be small when compared to the other components of the model, see Ref. [10]. Therefore, in the model description of the present work we will consider only the t-channel $\Delta\Delta$ process in addition to the d^* process. Thus, the differential cross section is described as follows:

$$d\sigma = \frac{(2\pi)^4}{4p_i\sqrt{s}}(|\tau_{I=0}\rho_{\Delta\Delta}M^{I=0}_{\Delta\Delta} + \rho_{d^*}M_{d^*}|^2 + |\tau_{I=1}\rho_{\Delta\Delta}M^{I=1}_{\Delta\Delta}|^2)\Theta(\theta)d\phi_3 \tag{7.2}$$

where $\rho_{\Delta\Delta}$ and ρ_{d^*} are the strength parameters of the t-channel $\Delta\Delta$ and the d^* contributions, respectively, which include all constant factors like coupling constants, etc. The constant τ_I parameters account for the isospin and spin Clebsch-Gordan coefficients and their calculation can be found in Appendix 9.3. The $\Theta(\theta)$ term describes the angular dependence and $M_{\Delta\Delta}$ and M_{d^*} are the matrix elements of the t-channel $\Delta\Delta$ and the s-channel d^* resonance, respectively.

The t-channel $\Delta\Delta$ Contribution

The t-channel $\Delta\Delta$ matrix element $M_{\Delta\Delta}$ is given by [22]:

$$M_{\Delta\Delta} = c\frac{e^{i\phi_{\Delta\Delta}}}{q^2 - m_\pi^2}m_\Delta\sqrt{\frac{\Gamma_{\Delta_1}\Gamma_{\Delta_2}}{q_{\pi_1}^{N_1\pi^1}q_{\pi_2}^{N_2\pi^2}}}D_{\Delta_1}D_{\Delta_2} \tag{7.3}$$

with c being an effective coupling constant, $\phi_{\Delta\Delta}$ the phase of the matrix element, $q_\pi^{N\pi}$ denotes the decay momentum of the pion in the Δ system and $m_\Delta = 1.23GeV$. The angular distribution of the Δ is described by the term $(1 + 3cos^2(\theta_{\pi_1}^{N_1\pi_1}))$ where the angle $\theta_\pi^{N\pi}$ refers to the angle of the pion in the Δ's frame. For two Δs the angular dependence gives a common factor in Eq. (7.2):

$$\Theta(\theta) = (1 + 3cos^2(\theta_{\pi_1}^{N_1\pi_1}))(1 + 3cos^2(\theta_{\pi_2}^{N_2\pi_2})) \tag{7.4}$$

The Δ propagators are given by:

$$D_\Delta = \frac{\sqrt{m_\Delta\Gamma_\Delta}/q_\pi^{N\pi}}{M^2_{N\pi} - m^2_\Delta + im_\Delta\Gamma_\Delta} \tag{7.5}$$

The width of the Δ is momentum dependent and given by:

$$\Gamma_\Delta(q_\pi^{N\pi}) = \gamma(q_\pi^{N\pi})^3 \frac{R^2}{1 + R^2(q_\pi^{N\pi})^2} \tag{7.6}$$

From Ref. [22] we have: $R = 6.3\ (\mathrm{GeV/c})^{-1}$ and $\gamma = 0.74$, leading to $\Gamma_\Delta \approx 110$ MeV at pole position.

The d^* Contribution

The s-channel resonance contribution M_{d^*}, as described in Ref. [28, 77]:

$$M_{d^*} = D_{d^*} D_{\Delta_1} D_{\Delta_2} \tag{7.7}$$

and the resonance propagator:

$$D_{d^*} = \frac{m_{d^*}\sqrt{f\Gamma_i\Gamma_{\Delta\Delta}}}{s - m_{d^*}^2 + i m_{d^*}\Gamma_{d^*}} \tag{7.8}$$

The factor

$$f = \frac{s}{p_i p_f} \frac{2J+1}{(2s_p+1)(2s_n+1)} \tag{7.9}$$

is the flux factor of the Breit-Wigner resonance. In the equation p_i is the momentum in the initial pn channel, $p_f = q_{\Delta\Delta}$ is the momentum of each Δ in the $\Delta\Delta$ system, into which the resonance decays, and s_p and s_n are the nucleon spins in the initial channel.

The widths Γ_i and $\Gamma_{\Delta\Delta}$ correspond to the partial widths of formation and decay respectively and are proportional to the respective coupling constants g_{pn} and $g_{\Delta\Delta}$. Since the total angular momentum of the resonance is $J = 3$, the formation width will be:

$$\Gamma_i = g_{np}^2 p_i^5 F(p_i) \approx const \tag{7.10}$$

where a form factor $F(p_i)$ is introduced. The width is constant to good approximation, since far away from the pn threshold the momentum dependence over the region of the resonance is small and can be neglected.

In the exit channel the resonance decays into two Δs and with a relative s-wave between the two Δs and we have:

$$\Gamma_{\Delta\Delta} = g_{\Delta\Delta}^2 q_{\Delta\Delta} F(q_{\Delta\Delta})^2 \tag{7.11}$$

where the monopole form factor,

$$F(q_{\Delta\Delta}) = \frac{\Lambda^2}{\Lambda^2 + q_{\Delta\Delta}^2} \tag{7.12}$$

introduces a $1/q_{\Delta\Delta}$ dependence in the width of the resonance. The cutoff parameter Λ is fitted to the experimental data in the $M_{\pi\pi}$ spectrum for best reproduction of the data and causes the ABC effect by suppression of the high-mass region.

The total width of the resonance, Γ_{d^*} is described by:

$$\Gamma_{d^*} = \Gamma_i + \sum \Gamma_f \approx \Gamma_0 + \gamma_{d^*} \int q_{\Delta\Delta} F(q_{\Delta\Delta})^2 |D_{\Delta_1}(m_1^2) D_{\Delta_2}(m_2^2)|^2 \tag{7.13}$$

where the sums runs over all possible $q_{\Delta\Delta}$, m_1 and m_2 where m_i denotes the invariant mass of the $N\pi$ subsystems forming the Δs. The width Γ_0 accounts for the sum of the decay widths into NN and $NN\pi$ channels. The width can be estimated to have a value of 7 MeV [28, 77].

The term γ_{d^*} contains the coupling constant $g_{\Delta\Delta}$ and the strength of the decays into unbound channels, the value is fitted to yield a total width of $\Gamma_{d^*}(s = M_{d^*}^2) = 70$ MeV in the basic $pn \to d\pi^0\pi^0$ reaction.

A more detailed description of the basic pn reaction model can be found in Ref. [77]. Also, in Refs. [10, 28] the model described here can be found along with the experimental results for $pn \to d\pi^0\pi^0$ and $dd \to {}^4\mathrm{He}\pi^0\pi^0$ respectively, proving to be a very good description of the ABC resonance for both cross section and differential distributions.

7.2 ABC Resonance Model in $pd \to {}^3\mathrm{He}\pi^0\pi^0$

The ABC Resonance Model assumes the reaction to take place via the basic fusion process leading to a deuteron plus a spectator which fuses with the deuteron to form ^{3}He. We simplify the calculations by assuming that each of the nucleons inside the ^{3}He have a third of the total momentum of the Helium and the two of them which fuse to deuteron have, in addition, the corresponding Fermi momenta calculated as in Eq. (6.1). An analog approach was already shown to successfully describe the reaction $dd \to {}^4\mathrm{He}\pi^0\pi^0$, see Ref. [28].

The remaining components of the model are obtained by a fit to the experimental data. As was shown in the ^{4}He case [28], the width of the resonance might be different from those for the basic case due to collision broadening, thus they need to be also

deduced from the fit. The rest of the parameters to be fitted correspond to the phase $\phi_{\Delta\Delta}$ and the strength constants, $\rho_{\Delta\Delta}$ and ρ_{d^*}, of the matrix elements. The strengths ρ includes all constant factors like coupling constants etc. The phase $\phi_{\Delta\Delta}$ and strength $\rho_{\Delta\Delta}$ are given with respect to the resonance phase and strength (assigned to be $\rho_{d^*} = 1$ in the fit).

Different isospin contributions from the $\Delta\Delta$ t-channel are taken into account, $\sigma(NN \rightarrow \Delta\Delta) = \sigma(I_{NN} = 0) + \sigma(I_{NN} = 1)$. The isoscalar part interferes with the resonance d^*, while the isovector part is added incoherently. The relation between both contributions is deduced from isospin relations and is calculated to be, see Appendix 9.3:

$$\frac{\sigma(I_{NN} = 1)}{\sigma(I_{NN} = 0)} = \frac{5}{9(3 - 2\sqrt{2})} \approx 3.2 \tag{7.14}$$

The model parameters extracted from the fit to total cross section and the differential distributions are given in Tab. 7.1. All data presented here are corrected for acceptance and efficiency with MC simulations for the ABC model with these parameters. Variations of them are used to establish the systematic error associated to this correction.

Parameter		$pn \rightarrow d\pi^0\pi^0$ [10, 27]	**pd** $\rightarrow$**^{3}He$\pi^0\pi^0$**	$dd \rightarrow {}^4\mathrm{He}\pi^0\pi^0$ [29]
d^* *Resonance*	M_{d^*}	2.37 ± 0.01 GeV	**2.37 ± 0.01 GeV**	2.37 ± 0.01 GeV
	$\Gamma^{eff}_{d^*}$	70 MeV	**85 MeV**	124 MeV
	Λ	0.15 – 0.2 GeV/c	**0.25 GeV/c**	0.3 GeV/c
	ρ_{d^*}		**1**	
t-channel $\Delta\Delta$	$\rho_{\Delta\Delta}$		**0.37**	
	$\phi_{\Delta\Delta}$		**0°**	

Table 7.1: Fit parameters for the ABC model for the reaction $pd \rightarrow {}^3\mathrm{He}\pi^0\pi^0$. The results from the $pn \rightarrow d\pi^0\pi^0$ [10, 27] and $dd \rightarrow {}^4\mathrm{He}\pi^0\pi^0$ [29] reactions are given for comparison.

7.3 Fermi Correction

Investigation of the quasi-free $pd \rightarrow {}^3\mathrm{He}\pi^0\pi^0$ reaction measured in dd collisions offers the advantage that instead of one single energy, we obtain simultaneously a range of energies due to the motion of nucleons inside the deuteron. The Fermi momentum

of the nucleons within the deuteron produces a spread of the effective c.m. energies, $\sqrt{s}$. To obtain the energy dependence of the cross section the experimental data must be divided on event-by-event basis by the c.m. energy distribution, see Fig. 7.1, from the generated MC simulation based on the Hulthén wavefunction given by Eq. (6.1). After the correction is applied the data are binned in intervals of 20 MeV in $\sqrt{s}$. The price to pay is, of course, a splitting of the available statistics.

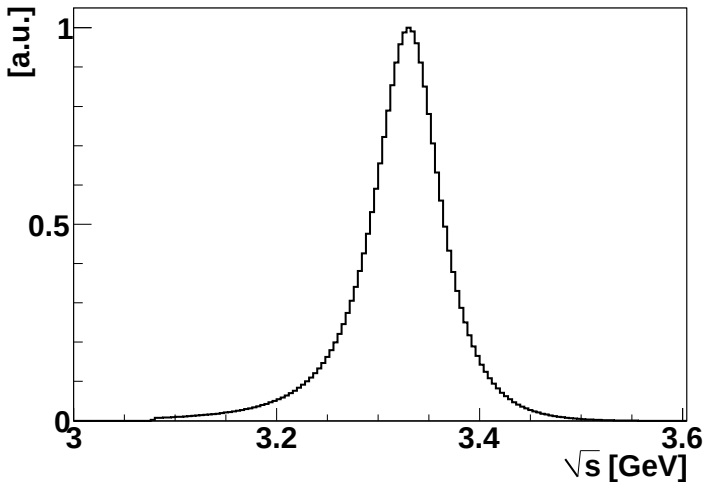

Figure 7.1: Distribution of the effective c.m. collision energies for the quasi-free reaction $dd \rightarrow {}^3\mathrm{He}\pi^0\pi^0(n_{spect})$ with $T_d = 1.7$ GeV.

7.4 Total Cross Section

A main result from the analysis, the total cross sections for the quasi-free and single-energy measurements are presented and discussed in this section. The Fig. 7.2 shows to the total cross section versus the center of mass energy. The solid black points correspond to the quasi-free measurement from the $dd \rightarrow^3 \mathrm{He}\pi^0\pi^0(n_{spect})$ reaction at $T_d = 1.7$ GeV, the solid green triangle is from the single-energy measurement of $pd \rightarrow^3 \mathrm{He}\pi^0\pi^0$ at $T_p = 1.0$ GeV[1].

[1]As explained in Sect. 6.7, the cross sections from the quasi-free reaction have been normalized to the single-energy measurement.

In the plot, the open red squared data point corresponds to the previous CELSIUS/WASA measurement from Ref. [26]. This point has been renormalized. In Ref. [78], the normalization of the cross section was done assuming that the differential cross section of $pd \rightarrow {}^3\mathrm{He}\pi^0$ did not follow the parameterization presented in Sect. 6.7.1 (Fig. 6.19). Instead, a value of 100 nb/sr was assumed at $\sqrt{s} = 3.357$ GeV. This is a factor of about 1.5 larger than the value from Ref. [75]. This factor has been taken into account in Fig. 7.2.

The open black data point belongs to a previous measurement close the $\pi^0\pi^0$ threshold, carried out by a Stockholm-Uppsala group at CELSIUS, see Ref. [25].

Along with the statistical errors (error bars at the data points) the systematic errors are shown as a shaded area below the curves. Substantial sources to the systematic uncertainties are the rest gas contribution, the efficiency-acceptance correction and the demand on the χ^2 distribution of the kinematic fit. The efficiency-acceptance correction has the larger impact at the edges of the cross section distribution, where the estimated errors amount to a systematic effect as large as 15%. At the peak position it is almost negligible, being only of about 2%. In this region the systematic error from the normalization to the single-energy measurement is the dominant one.

The curves in the plot show the calculation for the ABC resonance model described at the beginning of this chapter (solid line) as well as the t-channel $\Delta\Delta$ (dashed line), which includes both isospin I = 0 and I = 1 parts, and d^* (dotted line) contributions to it.

As in the other double-pionic fusion reactions ([10, 28]) the total cross section exhibits a strong energy dependence with a peak at approximately $\sqrt{s} = 3.40$ GeV.

The main contribution to the peak in Fig. 7.2 is from the t-channel $\Delta\Delta$ (dashed line) due to the isospin I = 1 contribution in this reaction, see Sect. 7.1. The I = 1 part, which does not interfere with the s-channel d^* resonance, is added incoherently in the total cross section described by Eq. (7.2). According to the isospin decomposition of the t-channel $\Delta\Delta$ (see Appendix 9.3) it is also a larger contribution than the I = 0 part. The d^* resonance (dotted line), which interferes with the I = 0 contribution from the t-channel $\Delta\Delta$, is thus substantially less influential at the maximum. In Eq. (7.2) this isospin contribution is added coherently to that of the s-channel resonance. This explains the rapid changes in the differential distributions at c.m. energies $\sqrt{s}$ right before the maximum, once the total cross section becomes dominated by the $\Delta\Delta$ contribution.

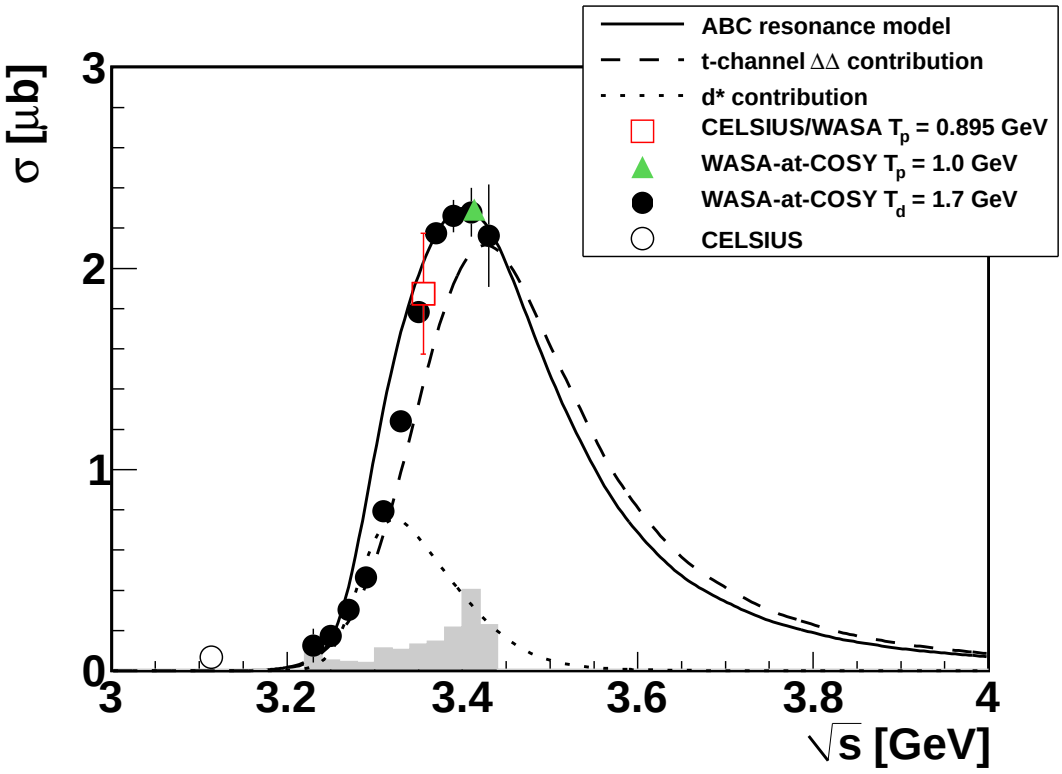

Figure 7.2: Energy dependence of the total cross section for the reaction $pd \rightarrow {}^3\mathrm{He}\pi^0\pi^0$. The solid circles correspond to the quasi-free measurement in this work. The solid green triangle represents the single-energy measurement in this work at $T_p = 1.0$ GeV. The open red square is the CELSIUS/WASA measurement from Ref. [26] properly renormalized. The open black circle corresponds to the CELSIUS measurement from Ref. [25]. The shaded area denotes the estimated systematic errors. The solid line represents the ABC resonance model and dashed and dotted lines are the t-channel $\Delta\Delta$ and d^* contributions, respectively. The relative contributions of d^* and $\Delta\Delta$ are properly normalized to the total cross sections. Model parameters are fitted to the data, see Sect. 7.1

Since the ABC effect in the invariant mass $M_{\pi^0\pi^0}$ is generated by the d^* resonance, the maximum of the ABC effect does not take place at exactly the maximum of the resonance structure in Fig. 7.2 but slightly before at a c.m. energy of $\sqrt{s} \approx 3.35$ GeV. This observation agrees with the previous measurement at CELSIUS/WASA [26, 78], which was measured at a c.m. energy of $\sqrt{s} = 3.357 GeV$, where the ABC effect exhibits the largest enhancement in $M_{\pi^0\pi^0}$ but, as seen in Fig. 7.2, below the maximum of the resonance structure in the energy dependence of the total cross section.

Altogether, the ABC resonance model describes very well the new experimental data, which is also in good agreement with the previous measurement.

7.5 Differential Distributions

To get to know more about the reaction, the differential distributions of the various observables are very useful. In the quasi-free reaction, the center of mass energy was subdivided in intervals of 20 MeV and observables were obtained for each of them. The data can be then also compared to the previous experiment at CELSIUS/WASA, Ref. [26], and to the results from the single-energy measurement studied in this work.

7.5.1 Invariant Mass Distributions

The invariant mass of a system is defined as the square of the four-vectors of the respective system: $M = \sqrt{E_{tot}^2 - \vec{\mathbf{p}}^2}$. It is a Lorentz-invariant quantity. For a three body reaction there are three possible invariant mass distributions: $M_{\pi\pi}$, $M_{^3\mathrm{He}\pi_1}$ and $M_{^3\mathrm{He}\pi_2}$. For neutral pions, since they are indistinguishable, the number of possible invariant mass distributions are reduced to two.

In Fig. 7.3 the two invariant mass distributions are shown for the energy where the ABC effect exhibits its maximum, i.e. $\sqrt{s} \approx$3.35 GeV.

In the $\pi^0\pi^0$-system the low-mass enhancement is the dominant feature. As observed in the previous exclusive experiments with CELSIUS/WASA [26], the ABC effect is well pronounced but not as strong as, e.g., in the double-pionic fusion to ^{4}He [28, 29]. The conventional t-channel $\Delta\Delta$ process contributes mostly in the high-mass region. The lines represent the ABC resonance model calculation (solid line) along with the two contributions corresponding to the t-channel $\Delta\Delta$ process (dashed line) and the d^* resonance (dotted line).

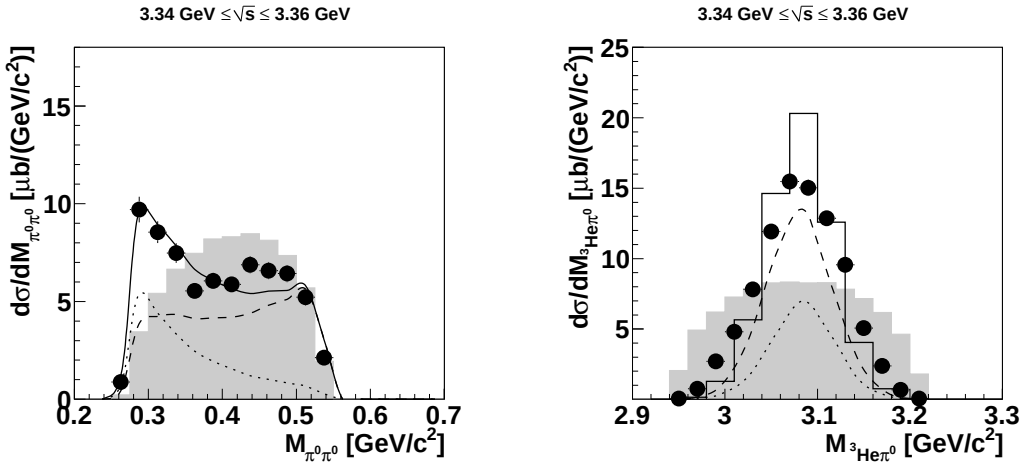

Figure 7.3: Invariant mass distributions at the maximum of the ABC effect. The data result from the quasi-free measurement. The lines show the calculations for the ABC resonance model (solid line), the t-channel $\Delta\Delta$ contribution (dashed line) and the d^* contribution (dotted line). The shadowed area corresponds to phase space.

In the case of the invariant mass distribution for ^{3}Heπ^0 we can observe a strong Δ excitation, predicted by both processes. The Δs decay in nucleon-π^0 pairs, since the nucleons fuse to Helium the Δ excitations can be observed in the invariant mass of the ^{3}Heπ^0 subsystem at approximately $2m_N + m_\Delta$.

Exploring the behavior of the ABC effect in dependence of the center-of-mass energy (see Fig. 7.4) we can observe how the enhancement at low $M_{\pi^0\pi^0}$ starts to increase with increasing energy, as in the other reactions investigated with WASA-at-COSY ([10, 28]). This low-mass enhancement is related to the excitation of the d^* s-channel resonance, see e.g. dotted line in Fig. 7.4, and it increases along with the amplitude of the resonance contribution. Once the maximum is reached the ABC effect fades away, at the same time as the t-channel $\Delta\Delta$ becomes more important. The vanishing of the ABC enhancement is very rapid once it reaches the maximum. This is understood from the strong contribution of the conventional t-channel $\Delta\Delta$ amplitude (see Sect. 7.1 and 7.4).

The results from the quasi-free measurement can be compared with the single-energy measurement at $T_p = 1.0$ GeV ($\sqrt{s} = 3.416$ GeV), see Fig. 7.5, and with the previous experiment at CELSIUS/WASA, see Fig. 7.6. In the first case one has a small

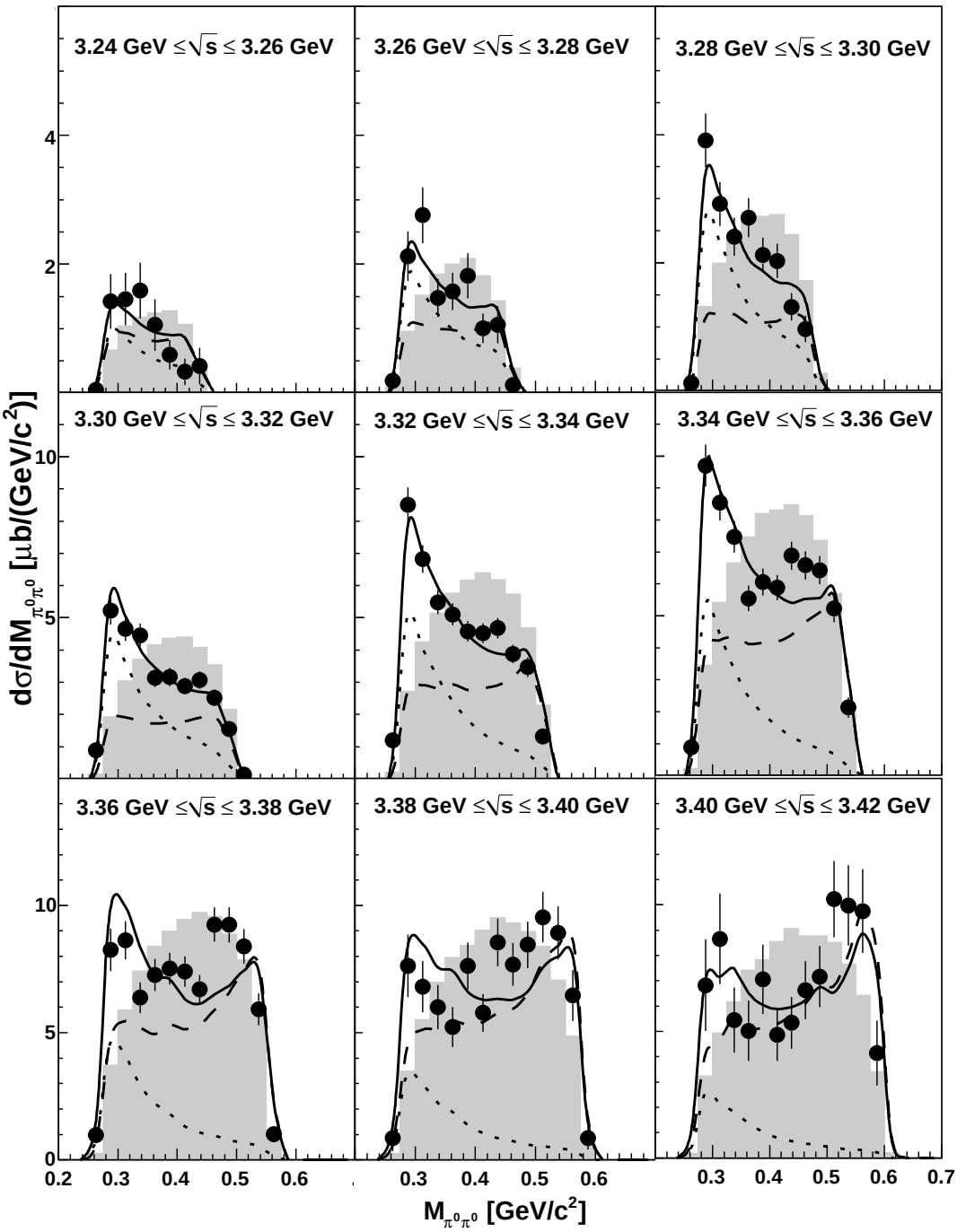

Figure 7.4: Invariant mass distributions for the $\pi^0\pi^0$ subsystem in dependence of $\sqrt{s}$. The data correspond to the quasi-free measurement. The solid lines correspond to the ABC resonance model, the dashed lines to the conventional t-channel contribution and dotted lines to the d^* contribution. The distributions are plotted in 20 MeV intervals of the c.m. energy $\sqrt{s}$. The shadowed areas represent phase space.

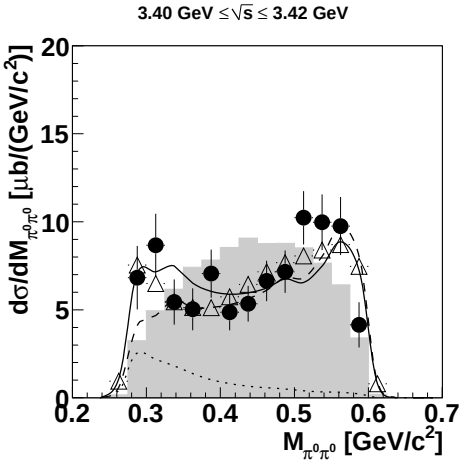

Figure 7.5: Comparison of invariant mass distributions for the $\pi^0\pi^0$ subsystem. The solid circles correspond to the experiment measured in quasi-free kinematics at 3.40 GeV $\leq \sqrt{s} \leq$ 3.42 GeV. Open triangles are from the single-energy measurement at $T_p = 1.0$ GeV ($\sqrt{s} = 3.416$). The solid line corresponds to the model calculation for the ABC resonance model. The dashed line represents the t-channel $\Delta\Delta$ contribution and the dotted line the d^* contribution. The shadowed area corresponds to phase space.

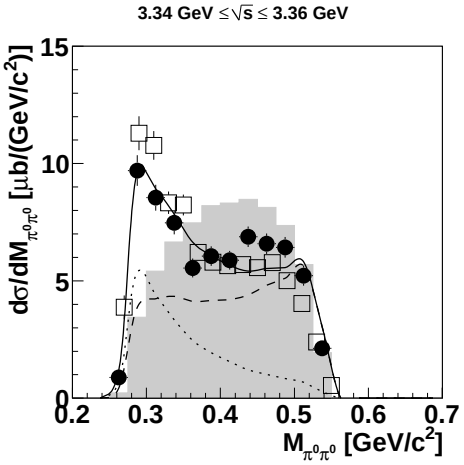

Figure 7.6: Comparison of the CELSIUS/WASA and the WASA-at-COSY invariant mass distributions for the $\pi^0\pi^0$ subsystem. The solid circles correspond to the present experiment measured in quasi-free kinematics at 3.34 GeV $\leq \sqrt{s} \leq$ 3.36 GeV. Open squared are from the CELSIUS/WASA measurement at $T_p = 0.895$ GeV ($\sqrt{s} = 3.357$) normalized to the present experiment area. The solid line corresponds to the model calculation for the ABC resonance model. The dashed line represents the t-channel $\Delta\Delta$ contribution and the dotted line the d^* contribution. The shadowed area corresponds to phase space.

ABC effect almost vanishing compared to the contribution from the $\Delta\Delta$ t-channel, which is the main amplitude at high energies. The open triangles correspond to the single-energy measurement.

Equally interesting is the comparison to the CELSIUS/WASA result. Both distributions are qualitatively similar. The comparison must be done taking into account that the quasi-free measurement distributions are taken in intervals of 20 MeV of $\sqrt{s}$. Because of the rapid increase of the total cross sections in this region ($\sqrt{s}\approx$3.35 GeV), the interval size is relevant when comparing these two distributions. From the model a change of the cross section within the bin size of about 20% has been estimated for this c.m. energy. Thus, the CELSIUS/WASA distribution is conveniently normalized to the area obtained in the quasi-free experiment for a qualitative comparison.

In the case of the $M_{^3\mathrm{He}\pi^0}$ distribution, the energy dependence is shown in Fig. 7.7. Along with the conventional t-channel we also expect the d^* s-channel resonance to decay into two Δs, thus, the invariant mass of the $^3\mathrm{He}\pi^0$ subsystem will exhibit a clear narrow peak over the whole $\sqrt{s}$ region studied.

Also, we may compare the quasi-free result to the single-energy measurements at T_p = 1.0 GeV, see Fig. 7.8, and at T_p = 0.895 GeV from CELSIUS/WASA, where the latter is normalized to the area of the quasi-free data, Fig. 7.9. In both cases the distributions from the two different kinematic measurements agree within the statistical errors.

7.5.2 Dalitz Plot

To investigate the various reaction mechanisms in a three-body reaction, a very useful tool is the Dalitz plot. This represents the distribution of the invariant mass squared of one system of decay particles versus another. In the case of the three body reaction $pd \rightarrow {}^3\mathrm{He}\pi^0\pi^0$ this will correspond to the two invariant masses described in the previous subsection. If a reaction follows the phase space expectation the Dalitz plot is uniform. When a resonance process takes place it will appear as a band in case of the two body system, see Fig. 7.10. This means that for three-body reactions with resonances, the Dalitz plot will be non-uniform, giving clues about the different decay channels.

Fig. 7.12 shows the Dalitz distributions in 20 MeV c.m. energy bins. One can clearly recognize the low-mass enhancement in $\pi^0\pi^0$ strongly marked as a peak whereas the $\Delta\Delta$

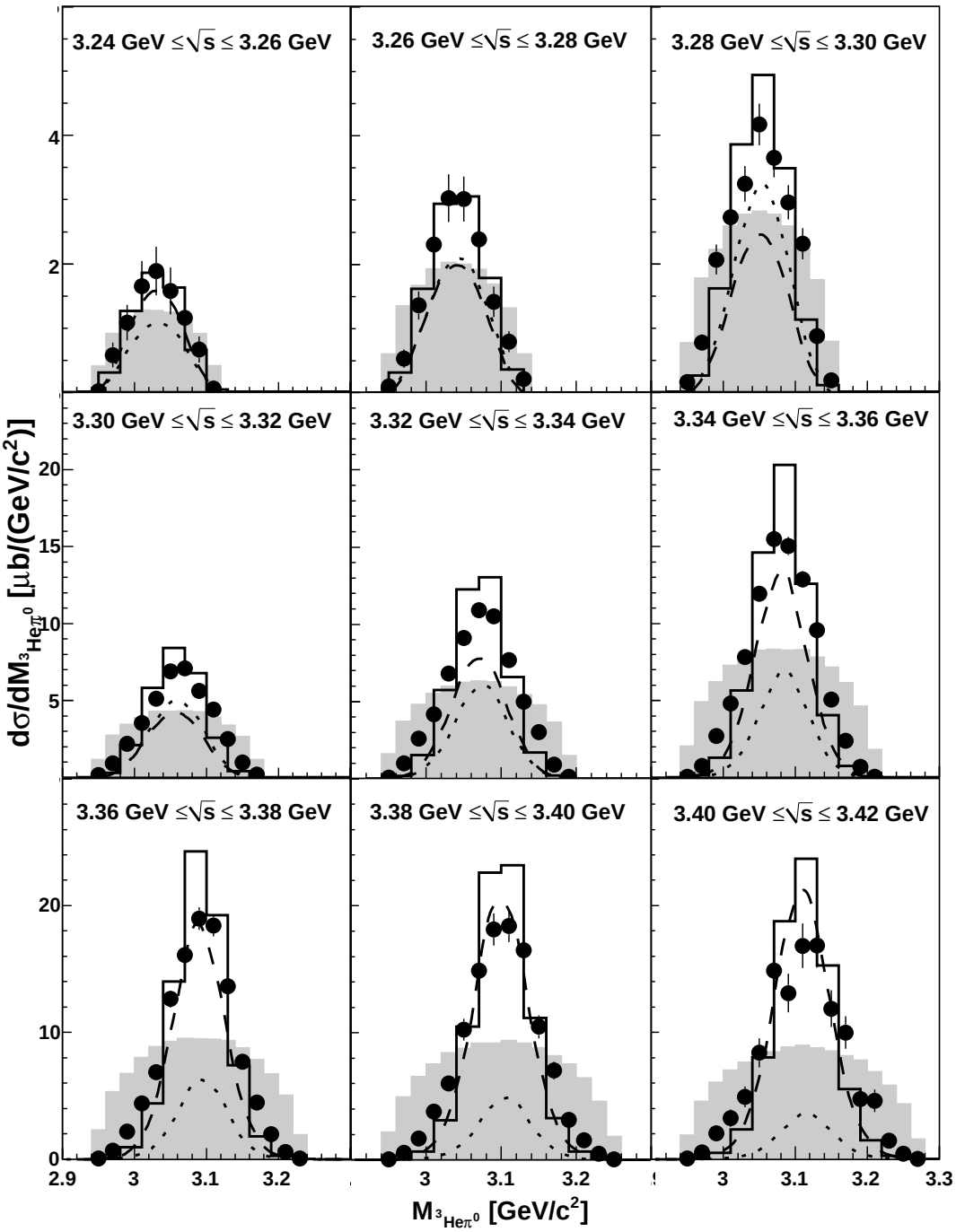

Figure 7.7: Invariant mass distributions for ^{3}Heπ^0 in dependence with the c.m. energy. The data correspond to the quasi-free measurement. The solid line corresponds to the ABC resonance model, dashed to the conventional t-channel contribution and dotted line to the d^* contribution. The distributions are plotted in 20 MeV intervals of the c.m. energy. The shadowed areas correspond to phase space.

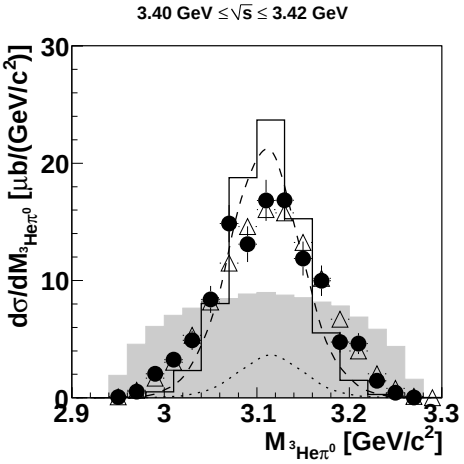

Figure 7.8: Comparison of the invariant mass distributions for the ^{3}Heπ^0 subsystem. The solid circles correspond to the present experiment measured in quasi-free kinematics at 3.40 GeV $\leq \sqrt{s} \leq$ 3.42 GeV. Open triangles are from the single-energy measurement at $T_p = 1.0$ GeV ($\sqrt{s} = 3.416$). The solid line corresponds to the model calculation for the ABC resonance model. The dashed line represents the t-channel $\Delta\Delta$ contribution and the dotted line the d^* contribution. The shadowed area corresponds to phase space.

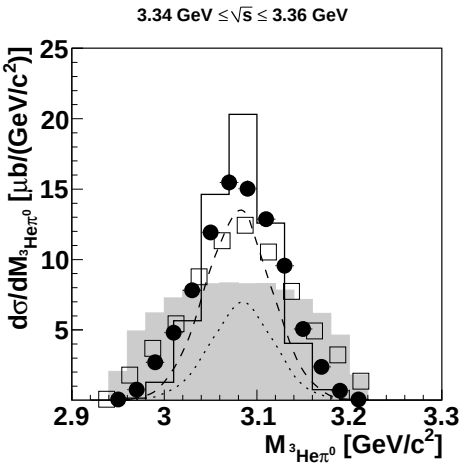

Figure 7.9: Comparison of the CELSIUS/WASA and the WASA-at-COSY invariant mass distributions for the ^{3}Heπ^0 subsystem. The solid circles correspond to the present experiment measured in quasi-free kinematics at 3.34 GeV $\leq \sqrt{s} \leq$ 3.36 GeV. Open squares are from the single-energy measurement at $T_p = 0.895$ GeV ($\sqrt{s} = 3.357$), normalized to the area of the black data points. The solid line corresponds to the model calculation for the ABC resonance model. The dashed line represents the t-channel $\Delta\Delta$ contribution and the dotted line the d^* contribution. The shadowed area corresponds to phase space.

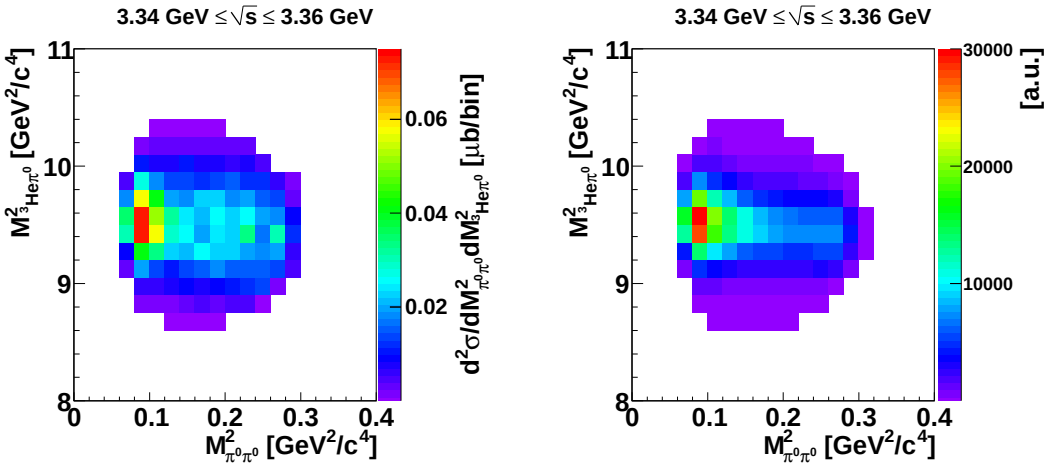

Figure 7.10: Dalitz plot $M^2_{^3\mathrm{He}\pi^0}$ versus $M^2_{\pi^0\pi^0}$ at the ABC maximum (3.34 GeV $\leq \sqrt{s} \leq$ 3.36 GeV). **Left**: Experimental data from the quasi-free measurement. **Right**: MC simulation with the ABC resonance model. The experimental data exhibit a strong peak from the ABC effect and a horizontal band, which corresponds to the $\Delta\Delta$ excitation in $^3\mathrm{He}\pi^0$-system.

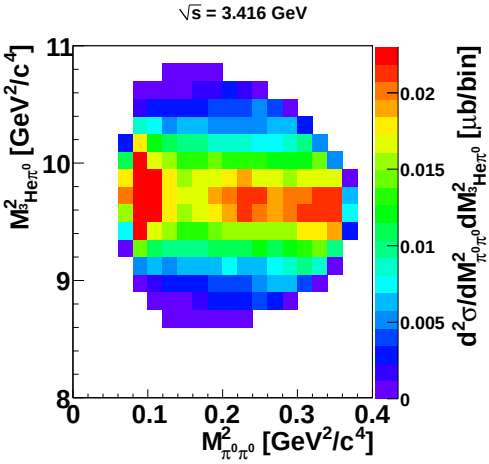

Figure 7.11: Dalitz plot of $M^2_{^3\mathrm{He}\pi^0}$ versus $M^2_{\pi^0\pi^0}$ from the single-energy experiment at $T_p = 1.0$ GeV ($\sqrt{s} = 3.416$ GeV). The $\Delta\Delta$ contribution is dominant in this region, thus, the plot exhibits two maxima.

excitation shows up as a band along the x-axis with center in the y-axis at approximately $(2m_N + m_\Delta)^2$. The ABC effect dominates at the energies $\sqrt{s} \lesssim 3.35$ GeV. Thereafter, in the region where the Delta excitation becomes more relevant, it develops into a two-hump structure. This is better seen in the single-energy measurement, for which the statistics are larger than in the quasi-free case. In Fig. 7.11 the Dalitz plot for the single-energy measurement at $T_p = 1.0$ GeV is shown. The two humped structure, caused by the t-channel $\Delta\Delta$ contribution, which is dominant in this region, is clearly seen.

7.5.3 Angular Distributions

The angular distributions are also of great interest. For each particle system and reference frame we can deduce important information about the reaction process. The most relevant combinations are shown here along with the model calculations.

To illustrate the different angular distributions discussed in this section, Fig. 7.13 sketches the various angles in the c.m. frame for three particles in the final state: p1, p2 and p3. In the spherical coordinate system (p, θ, ϕ), the polar angle θ is the scattering angle between the z-axis, which corresponds to the beam axis, and the particle track momentum, $\mathbf{p} = (p_x, p_y, p_z)$. In the two-particle rest frame the scattering angle is defined between the beam axis and the sum vector of the two particles, resulting in this particular case in two interesting scattering angle distributions: $\theta^{c.m.}_{\pi^0\pi^0}$ and $\theta^{c.m.}_{^3\mathrm{He}\pi^0}$. The opening angle between two particles, δ_{p1p2}, is calculated according to:

$$cos(\delta) = \frac{\overrightarrow{p_1} \cdot \overrightarrow{p_2}}{\mathbf{p_1} \cdot \mathbf{p_2}} \tag{7.15}$$

- $\delta^{cm}_{\pi^0\pi^0}$: is the opening angle between the two pions. It is related to the invariant mass in the $\pi\pi$-system. This means that small angles correspond to low relative momenta between the two pions, which corresponds to low invariant masses.

  In Fig. 7.14 the opening angle distributions for different intervals of the c.m. energy from the quasi-free measurement are shown. We can see how they peak at small angles as expected from the low-mass enhancement in the two pion system. Also the influence of the t-channel $\Delta\Delta$ process, where the pions are expected to have relative high momenta, affects the distributions at large angles, being dominant at the higher values of the center of mass energy.

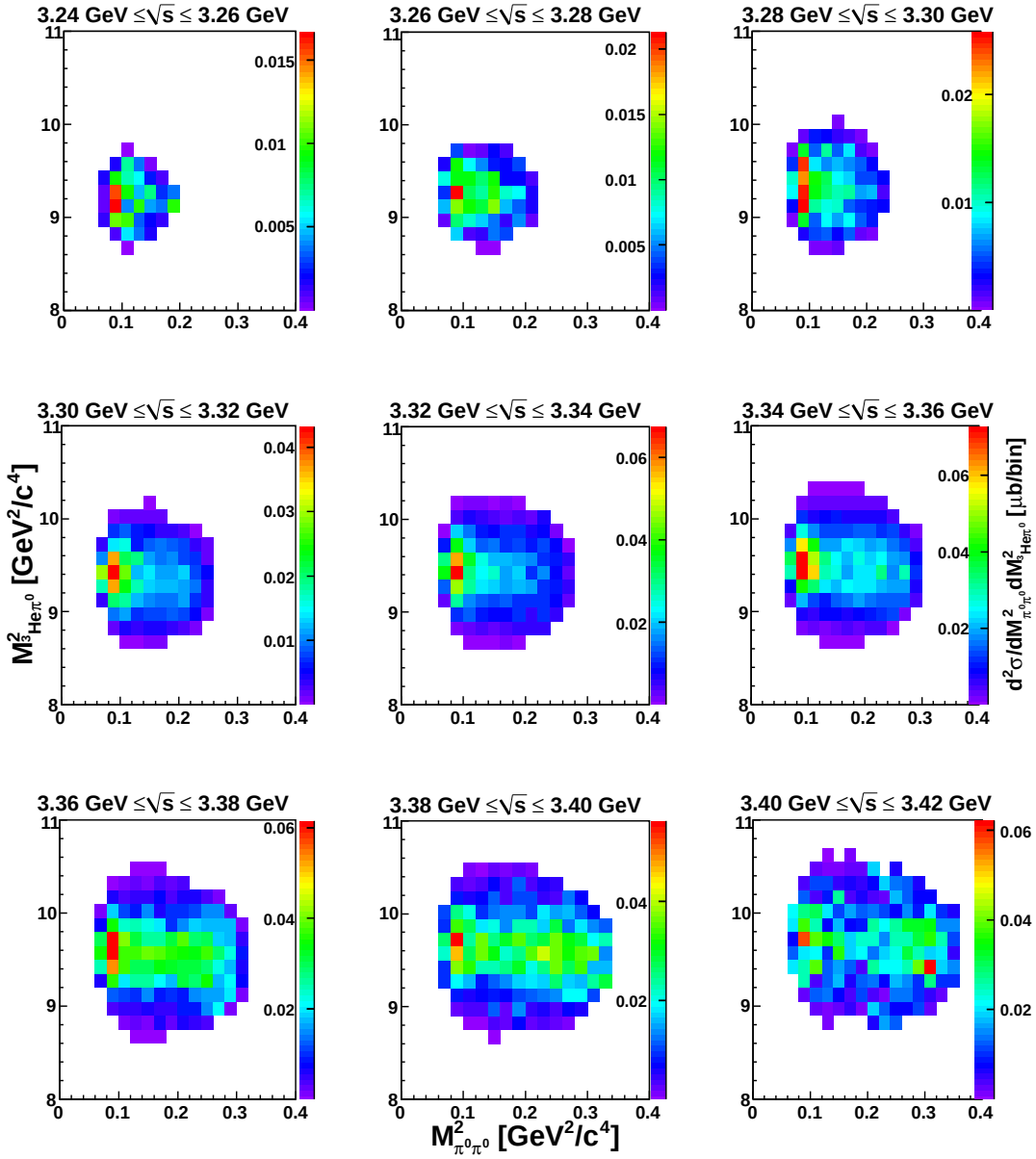

Figure 7.12: Dalitz plot of $M^2_{^3\mathrm{He}\pi^0}$ versus $M^2_{\pi^0\pi^0}$ from experiment in 20 MeV c.m. energy $\sqrt{s}$ bins.

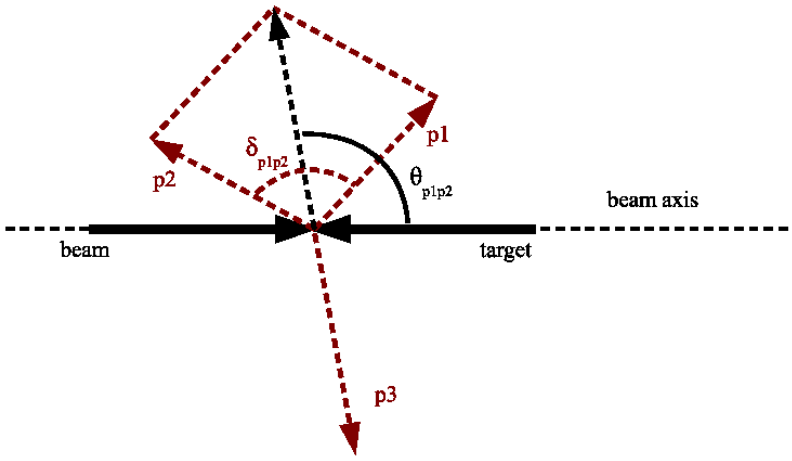

Figure 7.13: Definition of angles in the c.m. frame for three particles, p1, p2 and p3. In the drawing: the scattering angle of two particles (sum vector), θ_{p1p2} where p1 and p2 refer to two π^0 or ^{3}He and π^0 and the opening angle, δ_{p1p2} between two particles.

- $\theta^{\mathbf{cm}}_{\pi^0\pi^0}$: is the scattering angle of the $\pi^0\pi^0$ subsystem in the c.m. system. Kinematically this corresponds to the mirrored distribution of the ^{3}He polar angle distribution. This distribution is characterized by a "*smiling face*", a convex shape being the consequence of the angular distribution from the Δ excitation, present in both contributions. As already mentioned in Sect. 6.8, the acceptance of the WASA detector is lower for the forward going pion pairs in the c.m. system. For this reason the distributions are mainly populated for large scattering angles, see Fig. 7.15.

  In contrast to the double-pionic fusion to deuteron and ^{4}He, the angular distribution of the t-channel $\Delta\Delta$ contribution is not perfectly symmetric, as can be observed in the Figs. 7.15 and 7.16. Unlike the other double-pionic fusion reactions, in the case of ^{3}He the *pd* and the *pn* initial systems have different directions in the c.m. system. The t-channel $\Delta\Delta$ process is then influenced by this difference via the meson exchange between the Δs, giving rise to the observed asymmetry in the angular distribution in the c.m. system, while the s-channel resonance, d^*, remains symmetric.

- $\theta^{\mathbf{cm}}_{^3\mathrm{He}\pi^0}$: is the scattering angle of the $^3\mathrm{He}\pi^0$ subsystem, which is complementary to the single π^0 distribution in c.m. system. Here, as in the case of the pion pair, the shape is derived from the angular distribution of the Δs, giving rise to the "*smiling face*" mentioned before. As in the previous distribution, the meson exchange in the t-channel $\Delta\Delta$ gives rise to an asymmetry in the angular distributions.

In the case of the single-energy measurements at $T_p = 1.0$ GeV from this work and at $T_p = 0.895$ GeV from CELSIUS/WASA, the angular distributions also follow the same trends. In Figs. 7.18 the angular distributions from the single-energy measurements are compared to the quasi-free measurement at the same c.m. energy. For comparison the CELSIUS/WASA data, Fig. 7.17, are scaled to the area of the quasi-free measurement. The data essentially agree within uncertainties.

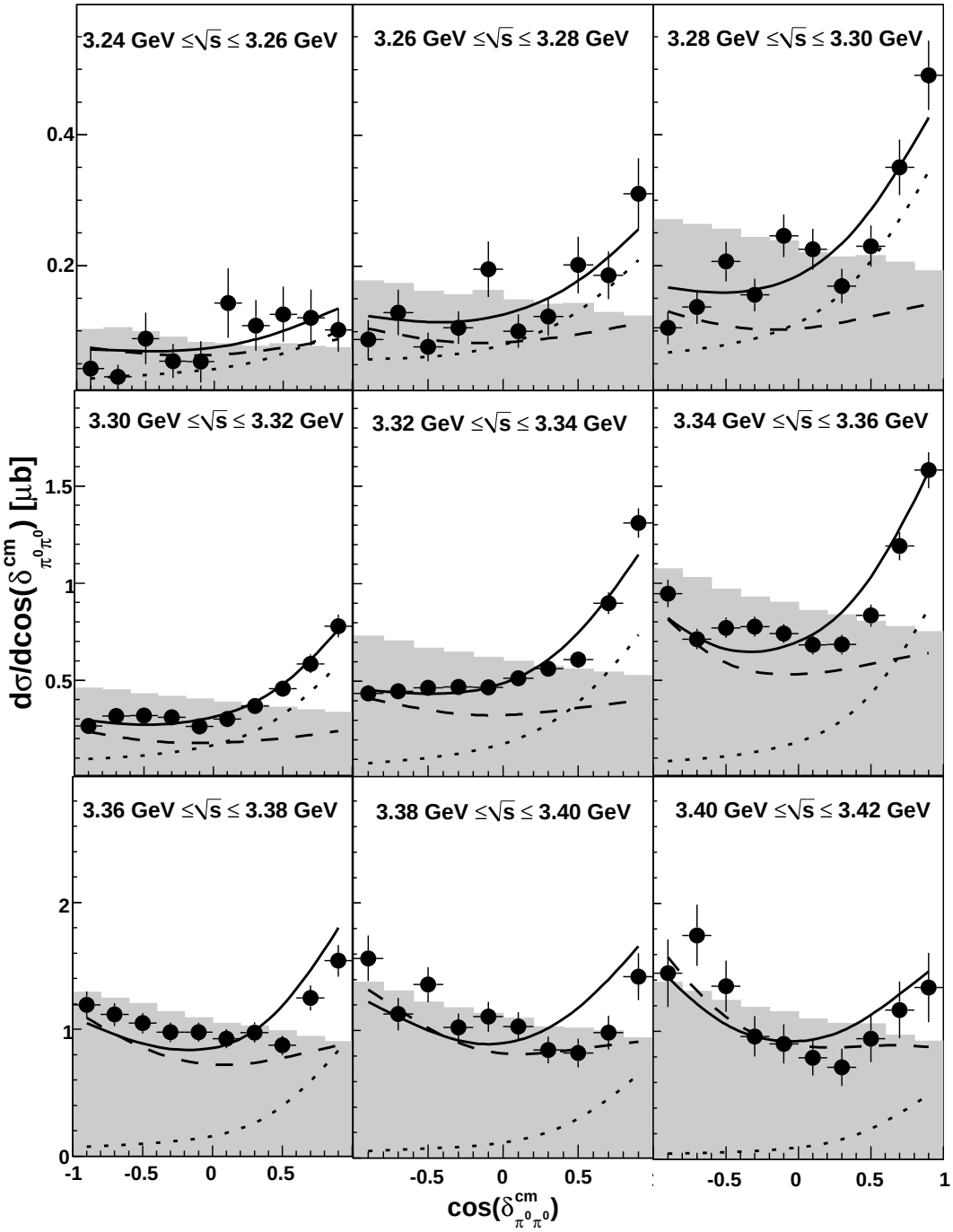

Figure 7.14: Opening angle distribution between pions in the c.m. system. Data correspond to the quasi-free measurement in intervals of 20 MeV of the c.m. energy. Solid lines denote the ABC resonance model. Dashed and dotted lines correspond to the contributions from the t-channel $\Delta\Delta$ and the d^* resonance, respectively. Shadowed areas correspond to phase space.

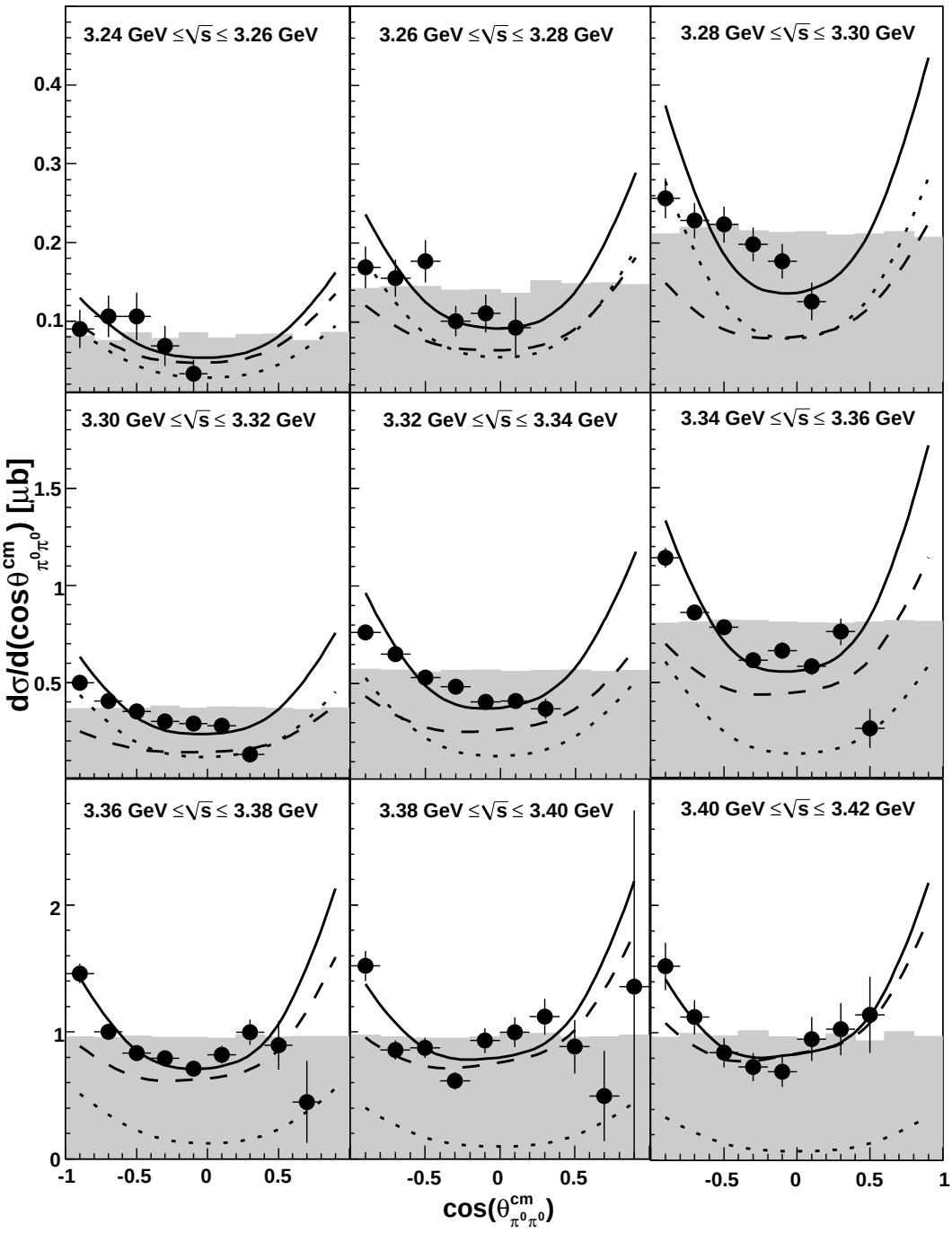

Figure 7.15: Scattering angle distributions of the $\pi^0\pi^0$ subsystem in the c.m. rest frame. Data correspond to the quasi-free measurement in intervals of 20 MeV of the c.m. energy. Solid lines denote the ABC resonance model. Dashed and dotted lines correspond to the contributions from the t-channel $\Delta\Delta$ and the d^* resonance, respectively. Shadowed areas correspond to phase space.

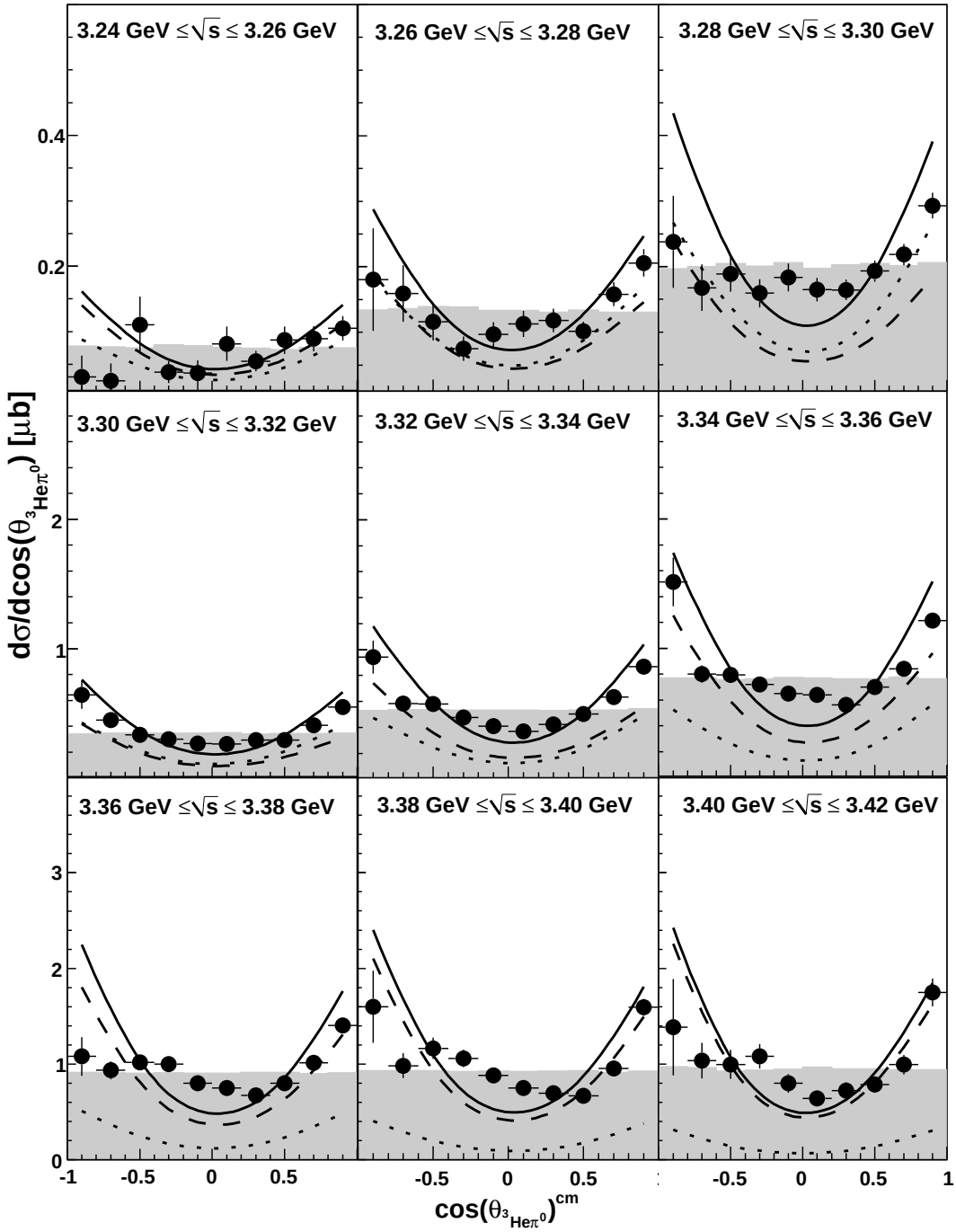

Figure 7.16: Scattering angle distributions of the ^{3}Heπ^0 subsystem in the c.m. rest frame. Data correspond to the quasi-free measurement in intervals of 20 MeV of the c.m. energy. Solid lines denote the ABC resonance model. Dashed and dotted lines correspond to the contributions from the t-channel $\Delta\Delta$ and the d^* resonance, respectively. Shadowed areas correspond to phase space.

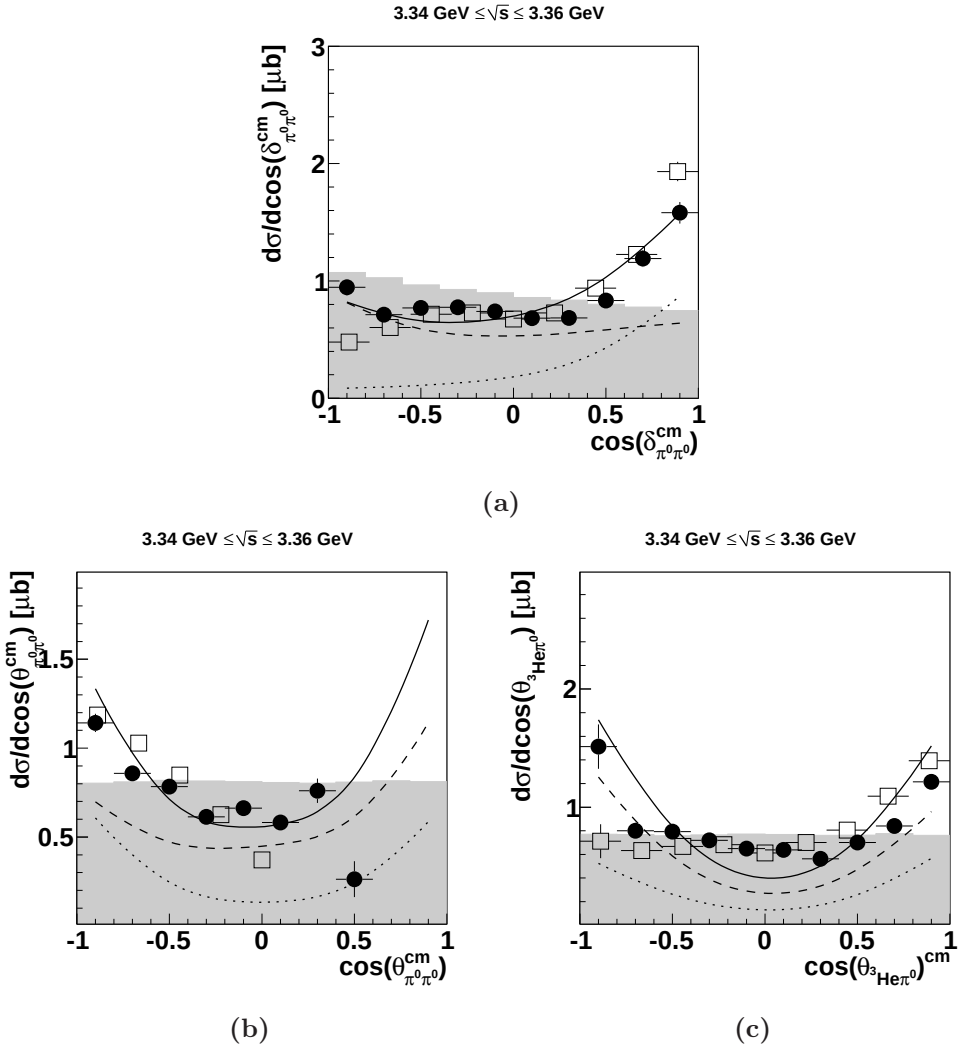

Figure 7.17: Angular distributions from single-energy measurement at $T_p = 0.895$ GeV from CELSIUS/WASA (open squares) compared to the quasi-free data (solid circles). The CELSIUS/WASA data are normalized in area to the quasi-free measurement. **Top**: Opening angle between the pions in the c.m. system. **Bottom right**: Scattering angle of the $\pi^0\pi^0$ subsystem in the c.m. rest frame. **Bottom left**: Scattering angle of the ^{3}Heπ^0 subsystem in the c.m. rest frame. Solid lines denote the ABC resonance model. Dashed and dotted lines correspond to the contributions from the t-channel $\Delta\Delta$ and the d^* resonance. Shadowed area corresponds to phase space.

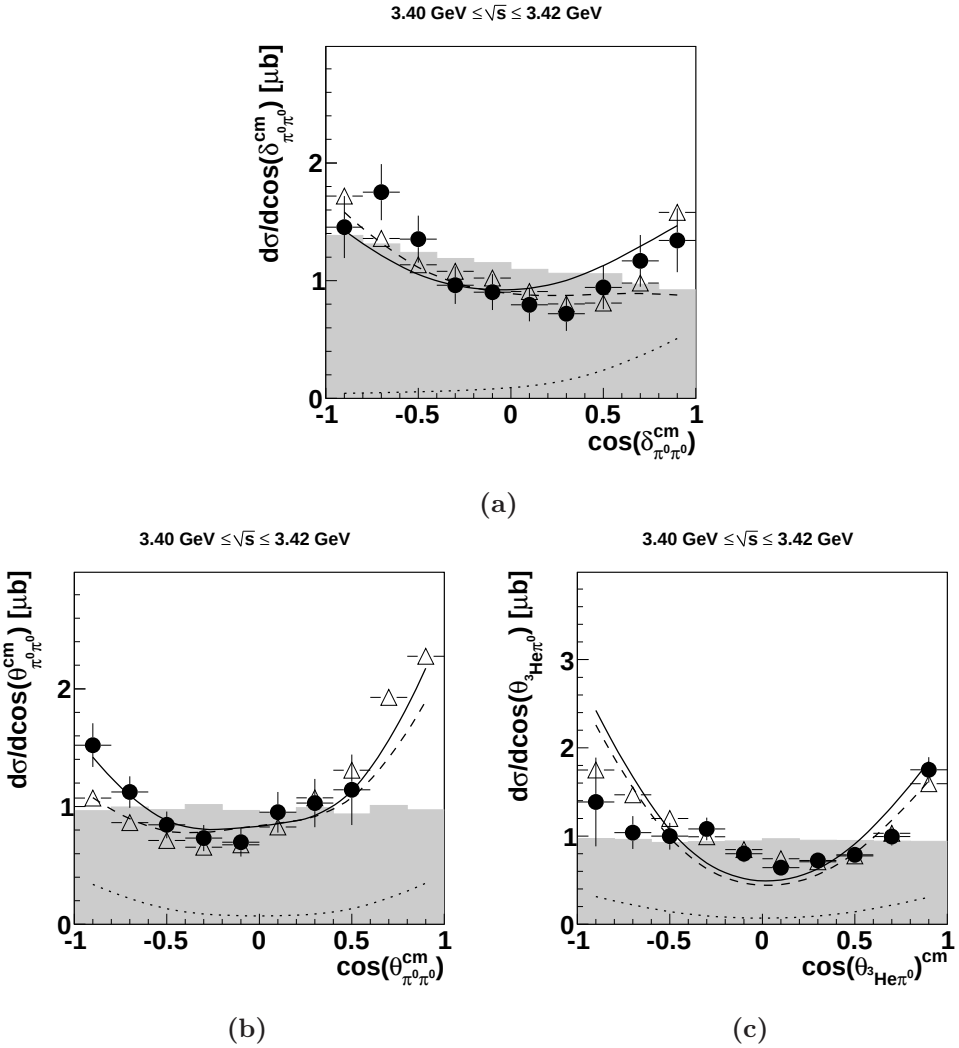

Figure 7.18: Angular distributions from single-energy measurement at $T_p = 1.0$ GeV (open triangles) compared to the quasi-free data (solid circles). **Top**: Opening angle between the pions in the c.m. system. **Bottom right**: Scattering angle of the $\pi^0\pi^0$ subsystem in the c.m. rest frame. **Bottom left**: Scattering angle of the ^{3}Heπ^0 subsystem in the c.m. rest frame. Solid lines denote the ABC resonance model. Dashed and dotted lines correspond to the contributions from the t-channel $\Delta\Delta$ and the d^* resonance. Shadowed area corresponds to phase space.

8

Summary and Outlook

The energy dependence of the double-pionic fusion to ^{3}He has been studied over the energy region, where the ABC effect takes place for the first time by exclusive and kinematically complete experiments more than 50 years after the first observation of the ABC effect in the inclusive $pd \to {}^3\mathrm{He}X$ reaction [9]. The measurement was done with the WASA facility at COSY in two different kinematic regimes by quasi-free and single-energy measurements. For the single-energy measurement experimental runs dedicated to η production in pd collisions at a beam energy of $T_p = 1.0$ GeV were used. In the case of the quasi-free measurement dd collisions at a deuteron beam energy of $T_d = 1.7$ GeV were studied. The quasi-free measurement uses the Fermi smearing of the proton inside the deuteron to obtain an effective range of c.m. energies, which allow to scan a broad energy region.

The results represent the first kinematically complete and exclusive measurements of the $pd \to {}^3\mathrm{He}\pi^0\pi^0$ reaction.

The data presented in this work show a pronounced $M_{\pi^0\pi^0}$ low-mass enhancement, the ABC effect, which reaches its maximum at about $\sqrt{s} \approx 3.35$ GeV. In the invariant-mass distribution of the $^3\mathrm{He}\pi^0$-system a narrow distribution corresponding to the Δ excitation is seen.

In the energy dependence of the total cross section a narrow resonance in the pn system, the d^* resonance, similarly to the double-pionic fusion to deuteron and ^{4}He, is observed. The resonance, which has been used for the description of the double-pionic fusion to d and ^{4}He, Ref. [28, 77], describes also both total cross section and differential distributions in the ^{3}He case. Due to the large contribution from the t-channel $\Delta\Delta$,

the double-pionic fusion to ^{3}He exhibits a maximum in the energy dependence of the cross-section above the maximum of the d^* resonance contribution. This also influences the invariant mass distributions of the $\pi\pi$-system, where the ABC effect fades away rapidly in the region where the t-channel $\Delta\Delta$ becomes dominant.

The extracted mass for the d^* resonance in the double-pionic fusion to ^{3}He is $M_{d^*}(^3\mathrm{He}) \approx 2.37$ GeV and its effective width of $\Gamma^{eff}_{d^*}(^3\mathrm{He}) \approx 85$ MeV, is a bit broader than in the double-pionic fusion to deuteron. It appears plausible to associate the increased effective width to collision damping. This effect is even larger in the ^{4}He case, where the effective width of the d^* resonance is $\Gamma^{eff}_{d^*}(^4\mathrm{He}) \approx 124$ MeV.

The width of the resonance structure in the energy dependence of the total cross-section might also be modified due to the Fermi motion of the nucleons in initial and final nuclei. This effect, once again, is more drastic in the ^{4}He case, where the Fermi momentum of the nucleons is larger compared to the ^{3}He case, thus enlarging the visible width of the structure.

The d^* resonance presents an obvious candidate for an exotic dibaryonic resonance. To further establish this conjecture, investigations for a better understanding are carried out at present. Of special interest is the study of elastic np collisions with polarized deuteron beam for which the analyzing power has been measured over the energy region of the d^* resonance. Inclusion of these data into the SAID partial wave analysis, indeed, produces a pole in $^3D_3$-$^3G_3$ partial waves in agreement with the d^* hypothesis, see Ref. [35].

Fusion experiments to heavier nuclei than He have been suggested as the next step in the study of the ABC effect and the d^* resonance, in order to see whether both can be observed in general in the nuclear medium. Since the next heavier nuclei are not stable or do not have the proper spin and isospin, the next suitable candidate reaction appears to be $d^{14}\mathrm{N} \rightarrow {}^{16}\mathrm{O}\pi\pi$ or in inverse kinematics ${}^{14}\mathrm{N}d \rightarrow {}^{16}\mathrm{O}\pi\pi$. However, such measurements would require very dedicated detector setups and/or accelerators. Another possibility to search for the ABC effect and the d^* resonance might be given by high resolution measurements of heavy ion reactions.

In addition to the ABC measurements the design and testing of a DIRC detector has been presented. The results from the tests are in agreement with the expectations from the simulations. The DIRC prototype was designed to increase the energy resolution of the Forward Detector of WASA. The building of this demonstrator and its subsequent

tests are very valuable for the future detector facility PANDA, which will include DIRC detectors.

9

Appendix

9.1 Selection Criteria for the Reaction $pd \rightarrow^3 He\,\pi^0\pi^0$

- **Conditions for all events:**

  Number of forward tracks ≥ 1

- **For CD tracks:**

  only neutral tracks

  Number of neutral central tracks = 4

  0.002 GeV $\leq$ Ekin $\leq$ 0.8 GeV

  $20^\circ \leq \theta \leq 169^\circ$

- **For FD tracks:**

  $2^\circ \leq \theta \leq 18^\circ$

  0. GeV $\leq$ Edep(FWC1) $\leq$ 0.04 GeV && 0. GeV $\leq$ Edep(FWC2) $\leq$ 0.04 GeV && 0. GeV $\leq$ Edep(FTH1) $\leq$ 0.04 GeV && 0. GeV $\leq$ Edep(FRH1) $\leq$ 0.4 GeV

  – if there is a hit in the previous layer:

    0. GeV $\leq$ Edep(FRH2) $\leq$ 0.4 GeV

    0. GeV $\leq$ Edep(FRH3) $\leq$ 0.4 GeV

    0. GeV $\leq$ Edep(FRH4) $\leq$ 0.45 GeV

0. GeV $\leq$ Edep(FRH5) $\leq$ 0.45 GeV

Total energy deposited in FRH array 0. GeV $\leq \sum Edep(FRH) \leq$ 1.2 GeV

– **For FD charged tracks:**

* must reach FRH1:

  Depe(FWC1)&& Depe(FWC2) && Depe(FTH1) && Depe(FRH1) $\geq$ 0. GeV

* **stop in FRH1** Edep(FRH2) = 0

* **stop in FRH2** Edep(FRH3) = 0

* **stop in FRH3** Edep(FRH4) = 0

* **stop in FRH4** Edep(FRH5) = 0

9.2 *CorrectStatistics* for Calibration

In the calibration process the extraction of the correction function for non-linearities had an additional obstacle: the limited experimental statistics of ^{3}He events available. As explained in the corresponding chapter (see chapter 6) all combinations of $\Delta E - \Delta E$ plots are fitted simultaneously. For many of the FRH elements the plots are highly nonuniform, e.g. they exhibit a greater concentration of hits for fast Helium ions than for those events stopping in the detector, see Fig. 9.1, and thus, those regions will have a much bigger influence on the result of the fit procedure. Hence, the fit will consider a good result for the parameters, which can describe the fast Helium events, even if the parameters give a result far away from the MC simulations.

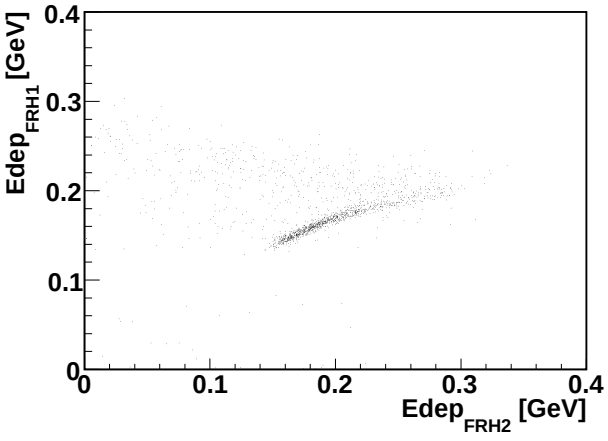

Figure 9.1: $\Delta E - \Delta E$ plot before homogenization of the population of the events.

To compensate for this effect, an additional algorithm, named *CorrectStatistics*, has been applied. It is called before the main fitting procedure. Its goal is to provide an homogeneous density of the ^{3}He events conserving, at the same time, the original shape of the Helium event distribution. The algorithm works as follows: first, starting from the two dimensional plots of the ADC(FRHX) versus ADC(FRHY) been X and Y two consecutive layers in the FRH (similarly as in the $\Delta E - \Delta E$ plots), we create the projection on the vertical axis. Next, the bin with the maximum content is found, $content_{max}$. In the next step, the scaling factors for consecutive Y bins are defined as:

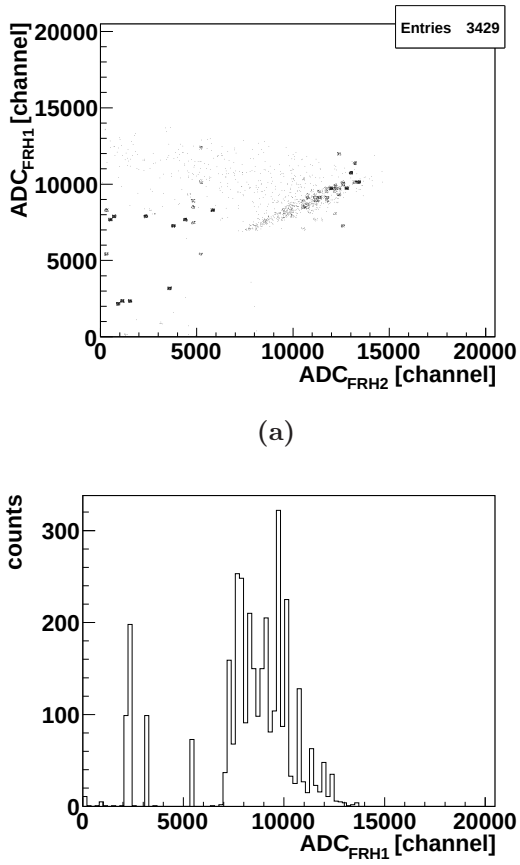

Figure 9.2: Two dimensional plots of ADC values. **Top**: ADC values from FRH1 vs ADC from FRH2. **Bottom**:Projection of the two dimensional plot onto the Y-axis.

$$sF_i = \frac{content_{max}}{content_i} \tag{9.1}$$

The scaling factors sF_i correspond to the i^{th} row of the two dimensional plot. For each row, the content of every bin is then multiplied by the corresponding scaling factors. E.g. for the k^{th} bin in the j^{th} row, it will correspond to:

$$content_k = sF_j \cdot content_k = \frac{content_{max}}{content_j} \cdot content_k \tag{9.2}$$

In Fig. 9.2 a two dimensional plot with ADC values and its corresponding vertical projection are shown. The result of this procedure in that case is shown in 9.3, and the

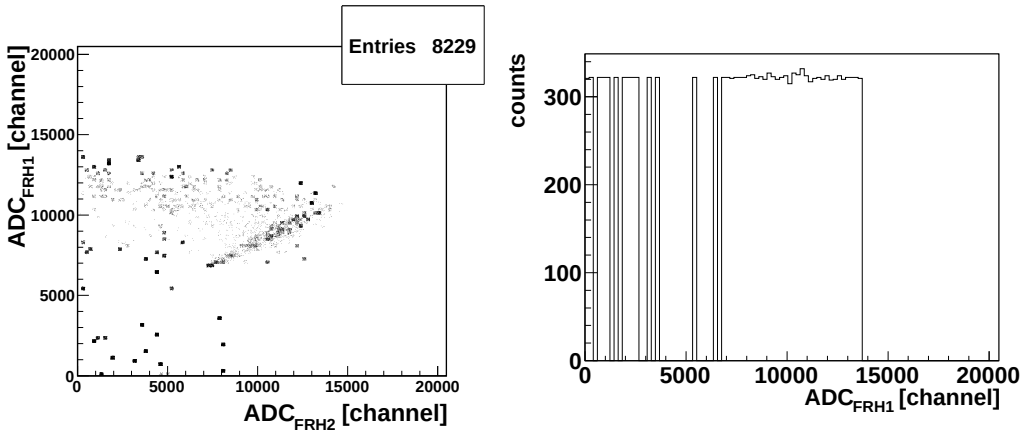

(a) (b)

Figure 9.3: Correction of the two dimensional plots of ADC values. **Left**: ADC values from FRH1 vs ADC from FRH2 after applying *CorrectStatistics*. **Right**:Projection of the two dimensional plot onto the Y-axis.

resulting $\Delta E - \Delta E$ plot in Fig. 9.4.

.

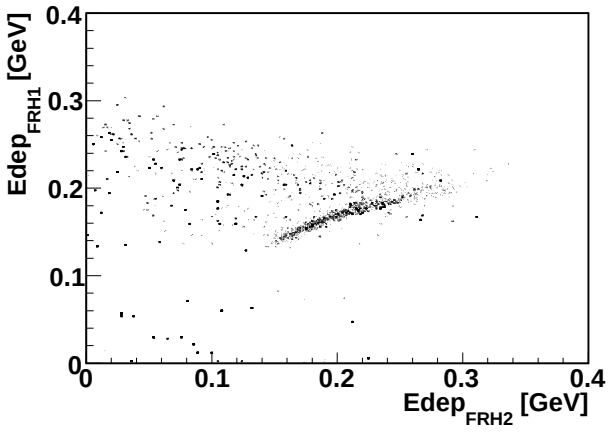

Figure 9.4: $\Delta E - \Delta E$ plot after homogenization of the population of the events.

9.3 Isospin Decomposition for the t-channel ΔΔ Contributions

In the Sect. 7.1, the isospin relation was used to calculate the different ΔΔ contributions to the ABC resonance model. The importance of knowing the strength of each contribution comes from the fact that, unlike in the double-pionic fusion reactions to d and ^{4}He, in the ^{3}He case the two Δs may have total isospin I = 0 or I = 1. This means that one may express the total cross section in the case of the t-channel ΔΔ as $\sigma(NN \to \Delta\Delta) = \sigma(I = 0) + \sigma(I = 1)$. Then,the s-channel resonance interferes only with the isoscalar (I = 0) contribution and the isovector one is added incoherently in amplitude in the model. For this reason, a detailed calculation of the total cross section relations for both channels have been done.

The cross sections can be estimated from the scattering amplitude:

$$\sigma \approx \sum_{I_{NN},m} |f_{I_{NN},m}|^2 = |\tau_I|^2 \tag{9.3}$$

where the sum runs over all possible isospin of the initial nucleon-nucleon system, I_{NN}, and z-projections of the spin, m.

According to Wigner-Eckart theorem we can always express the scattering amplitude in terms of Clebsch-Gordan coefficients and the reduced matrix elements, which in our case will be:

$$\begin{aligned} f_{I_{NN},m} = \sum_{I_{NN},m_{NN}} & < I^{NN}, I_z^{NN}; i^N, i_z^N | I, I_z > \\ \times & < S^{NN}, m^{NN}; s^N, m^N | s, m > C_{I_{NN} I_z} M_{I_{NN} I_{\pi^0 \pi^0} I_{\Delta\Delta}} \end{aligned} \tag{9.4}$$

Here the terms $< I^{NN}, I_z^{NN}; i^N, i_z^N | I, I_z >$ and $< S^{NN}, m^{NN}; s^N, m^N | s, m >$ correspond to the isospin and spin coefficients for the nucleons within the ^{3}He, with I_{NN} referring to isospin of the nucleon pair which excites to the ΔΔ pair, i^N the isospin of the remaining nucleon and I that one of the Helium. The subscript z is used for the z-projections. In the case of the spin coefficients a similar nomenclature is used, S_{NN} for the nucleon pair and s^N for the extra nucleon and s for ^{3}He, the z-projections of the spin are denoted by m. The coefficients $C_{I_{NN} I_z}$ correspond to the nucleon-nucleon

free case and $M_{I_{NN}I_{\pi\pi}I_{\Delta\Delta}}$ are the reduced matrix elements, which can be found in Refs. [79, 80].

Now we look at our reaction $pd \to {}^3\mathrm{He}\pi^0\pi^0$. We know the isospin of the reaction:

$$\begin{array}{cccccc} p & d & \to & {}^3\mathrm{He} & (\pi^0\pi^0) \\ I_p & I_d & \to & I_{^3\mathrm{He}} & I_{\pi\pi} \\ \frac{1}{2} & 0 & \to & \frac{1}{2} & 0 \end{array} \tag{9.5}$$

And for the $NN \to \Delta\Delta$ we have then two possibilities, $pp \to \Delta\Delta$ and $pn \to \Delta\Delta$, this means, for the isospin coefficients, from the configuration of the nucleons within Helium, the following:

$$\begin{aligned} &< I^{pp}, I_z^{pp}; i^n, i_z^n | I, I_z >: \\ &\qquad < 1,1; \tfrac{1}{2}, -\tfrac{1}{2} | \tfrac{1}{2}, +\tfrac{1}{2} >= \sqrt{\tfrac{2}{3}} \\ &< I^{pn}, I_z^{pn}; i^p, i_z^p | I, I_z >: \\ &\qquad < 1,0; \tfrac{1}{2}, +\tfrac{1}{2} | \tfrac{1}{2}, +\tfrac{1}{2} >= -\sqrt{\tfrac{1}{3}} \\ &\qquad < 0,0; \tfrac{1}{2}, +\tfrac{1}{2} | \tfrac{1}{2}, +\tfrac{1}{2} >= 1 \end{aligned}$$

For the spin coefficients we know the spin of the proton and the ^{3}He to be 1/2, but the z-projection of the spin is not fixed so we need to account for all possibilities. The coefficients are then:

$< S^{pp}, m^{pp}; s^n, m^n | s, m >$:

$$< 0,0; \tfrac{1}{2}, m^n | \tfrac{1}{2}, m >= 1$$

$< S^{pn}, m^{pn}; s^p, m^p | sm >$:

$$< 0,0; \tfrac{1}{2}, m^n | \tfrac{1}{2}, m >= 1$$

$$< 1, m^{pn}; \tfrac{1}{2}, m^n | \tfrac{1}{2}, m >:$$

$m = \frac{1}{2}$:

$$< 1,1; \frac{1}{2}, -\frac{1}{2} | \frac{1}{2}, +\frac{1}{2} >= \sqrt{\frac{2}{3}}$$

$$< 1,0; \frac{1}{2}, +\frac{1}{2} | \frac{1}{2}, +\frac{1}{2} >= -\sqrt{\frac{1}{3}}$$

$m = -\frac{1}{2}$:

$$< 1,0; \frac{1}{2}, -\frac{1}{2} | \frac{1}{2}, -\frac{1}{2} >= \sqrt{\frac{1}{3}}$$

$$< 1,-1; \frac{1}{2}, +\frac{1}{2} | \frac{1}{2}, -\frac{1}{2} >= -\sqrt{\frac{2}{3}}$$

The coefficients for the nucleon-nucleon free case $C_{I_{NN} I_z}$ are then taken from Refs. [79, 80]:

$C_{I_{pp} I_z}$:

$$C_{1,1} = \tfrac{1}{\sqrt{12}}$$

$C_{I_{pp} I_z}$:

$$C_{1,0} = \tfrac{1}{\sqrt{24}}$$

$$C_{0,0} = \tfrac{1}{\sqrt{24}}$$

thus the scattering amplitudes will be, replacing all coefficients in (9.4):

$$I_{NN} = 0: \qquad f_{0,m} = 1 \cdot (\sqrt{\frac{2}{3}} - \sqrt{\frac{1}{3}}) \frac{1}{\sqrt{24}} M_{000}$$

$$I_{NN} = 1: \qquad f_{1,m} = (\sqrt{\frac{2}{3}} \cdot 1 \cdot \frac{1}{\sqrt{12}} - \sqrt{\frac{1}{3}} \cdot 1 \cdot \frac{1}{\sqrt{24}}) M_{101}$$

For a specific process the reduced matrix elements are related by the 9j-symbol for isospin re-coupling, which in case of the t-channel $\Delta\Delta$ are [27]:

$$M_{I_{NN}I_{\pi\pi}I_{\Delta\Delta}} = M_{\Delta_1} M_{\Delta_2}$$

$$\times < (I_{N_1} I_{\pi_1}) I_{\Delta_1}, (I_{N_2} I_{\pi_2}) I_{\Delta_2}, I_{\Delta\Delta} m | (I_{N_1} I_{N_2}) I_{NN}, (I_{\pi_1} I_{\pi_2}) I_{\pi\pi}, I_{\Delta\Delta} m >=$$

$$= M_{\Delta_1} M_{\Delta_2} \sqrt{(2I_{\Delta_1}+1)(2I_{\Delta_2}+1)(2I_{NN}+1)(2I_{\pi\pi}+1)} \begin{Bmatrix} I_{N_1} & I_{\pi_1} & I_{\Delta_1} \\ I_{N_2} & I_{\pi_2} & I_{\Delta_2} \\ I_{NN} & I_{\pi\pi} & I_{\Delta\Delta} \end{Bmatrix} \tag{9.6}$$

From where we obtain:

$$\begin{aligned} M_{111} &= 0 \\ M_{000} &= -3M_{121} \\ M_{101} &= -\sqrt{5} M_{121} \\ M_{011} &= \sqrt{\frac{15}{2}} M_{121} \\ M_{110} &= \frac{3}{\sqrt{2}} M_{121} \end{aligned} \tag{9.7}$$

From the Eq. (9.7) it can be seen that:

$$M_{000} = \frac{3}{\sqrt{5}} M_{101} \tag{9.8}$$

Then the total cross sections, taking the squared amplitudes, are related by:

$$\frac{\sigma(I_{NN}=1)}{\sigma(I_{NN}=0)} = \frac{|\tau_{I=1}|^2}{|\tau_{I=0}|^2} = \frac{5}{9(3-2\sqrt{2})} \approx 3.2 \tag{9.9}$$

Bibliography

The blue numbers along the references link to the page where they have been cited.

[1] F. J. Dyson and N.-H Xuong. **Y=2 States in Su(6) Theory**. *Phys. Rev. Lett.*, **13**:815, December 1964. 1

[2] R. L. Jaffe. **Perhaps a Stable Dihyperon**. *Phys. Rev. Lett.*, **38**:195–198, January 1977. 1

[3] T. Goldman, K. Maltman, G. J. Stephenson, K. E. Schmidt, and Fan Wang. **"Inevitable" nonstrange dibaryon**. *Phys. Rev. C*, **39**:18891895, May 1989. 2, 11

[4] S. R. Beane et al. **Deuteron and exotic two-body bound states from lattice QCD**. *Phys. Rev. D*, **85**:054511, March 2012. 2

[5] S. R. Beane et al. **Light nuclei and hypernuclei from quantum chromodynamics in the limit of SU(3) flavor symmetry**. *Phys. Rev. D*, **87**:034506, February 2013. 2

[6] T. Inoue et al. **Two-baryon potentials and H-dibaryon from 3-flavor lattice QCD simulations**. *Nucl. Phys. A*, **881**:28–43, May 2012. 2

[7] T. Yamazaki et al. **Two-nucleon bound states in quenched lattice QCD**. *Phys. Rev. D*, **84**:054506, September 2011. 2

[8] T. Yamazaki et al. **Helium nuclei, deuteron, and dineutron in 2+1 flavor lattice QCD**. *Phys. Rev. D*, **86**:074514, October 2012. 2

[9] Alexander Abashian, Norman E. Booth, and Kenneth M. Crowe. **Possible Anomaly in Meson Production in p+d Collisions**. *Phys. Rev. Lett.*, **5**:258–260, August 1960. 2, 3, 4, 109

[10] P. Adlarson et al. **Abashian-Booth-Crowe Effect in Basic Double-Pionic Fusion: A New Resonance?** *Phys. Rev. Lett.*, **106**:202302, June 2011. 2, 7, 8, 9, 83, 84, 86, 87, 89, 92

[11] P. Adlarson et al. **Measurement of the $pn \to pp\pi^0\pi^-$ Reaction in Search for the Recently Observed Resonance Structure in $d\pi^0\pi^0$ and $d\pi^+\pi^-$ systems**. *Phys. Rev. C*, **88**:055208, November 2013. 2

[12] J.H. Hall, T.A. Murray, and L. Riddiford. **Evidence for a low-energy S-wave - interaction and a possible doubly charged dibaryon enhancement**. *Nucl. Phys. B*, **12**:573–585, September 1969. 3

[13] J. Banaigs et al. **Observation de l'effet "ABC" et d'une structure a 450 MeV dans des spectres de masse manquante mesonique**. *Nucl. Phys. B*, **28**:509–527, May 1971. 3

[14] J. Banaigs et al. **"ABC" and "DEF" effects in the reaction $d + p \to \mathrm{He}^3 + (mm)^0$: Position, width, isospin, angular and energy distributions**. *Nucl. Phys. B*, **67**:1–36, December 1973. 3

[15] J. Banaigs et al. **A study of the inclusive reaction $d + d \to {}^4\mathrm{He}X$, the ABC effect, and I = 0 meson resonances**. *Nucl. Phys. B*, **105**:52–76, March 1976. 3, 12

[16] F. Plouin et al. **Observation of the ABC effect in the reaction $n + p \to d + (mm)^0$ with A 1.88 GeV/c neutron beam**. *Nucl. Phys. A*, **302**:413–422, June 1978. 3, 5

[17] Norman E. Booth, Alexander Abashian, and Kenneth M. Crowe. **Anomaly in Meson Production in $p + d$ Collisions**. *Phys. Rev. Lett.*, **7**:35–39, June 1961. 4

[18] L. Rosselet et al. **Experimental study of 30 000 K_{e4} decays**. *Phys. Rev. D*, **15**:574, February 1977. 4

[19] C. D. Froggat and J. L. Petersen. **Phase-shift analysis of $\pi^+\pi$ scattering between 1.0 and 1.8 GeV based on fixed momentum transfer analyticity (II)**. *Nucl. Phys. B*, **129**:89–110, October 1977. 4

[20] S. Pislak et al. **A new measurement of $K^+_{(e4)}$ decay and the s-wave $\pi\pi$-scattering length a^0_0**. *Phys. Rev. Lett.*, **87**:221801, November 2001. 4

[21] NA48/2 Collaboration, J. R. Batley, et al. **Observation of a cusp-like structure in the $\pi^0\pi^0$ invariant mass distribution from $K^\pm \to \pi^\pm\pi^0\pi^0$ decay and determination of the $\pi\pi$ scattering lengths**. *Phys. Lett. B*, **633**:173–182, February 2006. 4

[22] T. Risser and M. D. Shuster. **Anomalous enhancements in multiple-pion production with deuterons**. *Phys. Lett. B*, **43**:68–72, January 1973. 4, 5, 6, 84, 85

[23] F. Plouin, P. Fleury, and C. Wilkin. **Identification and analysis of the $np \to d\eta$ cross section near threshold**. *Phys. Rev. Lett.*, **65**:690–693, August 1990. 6

[24] F. Belleman et al. **Pion-pion p-wave dominance in the $pd \to {}^3\mathrm{He}\pi^+\pi^-$ reaction near threshold**. *Phys. Rev. C*, **60**:061002, November 1999. 6

[25] M. Andersson et al. **Isospin resolved double pion production in the reaction $p + d \to {}^3\mathrm{He} + 2\pi$**. *Phys. Lett. B*, **485**:327–333, July 2000. 6, 89, 90

[26] M. Bashkanov et al. **Exclusive Measurements of $pd \to {}^3\mathrm{He}\pi\pi$: the *ABC* Effect Revisited**. *Phys. Lett. B*, **637**:223–228, 2006. 6, 7, 9, 48, 83, 89, 90, 91

[27] M. Bashkanov et al. **Double-Pionic Fusion of Nuclear Systems and the "ABC" Effect: Approaching a Puzzle by Exclusive and Kinematically Complete Measurements**. *Phys. Rev. Lett.*, **102**:052301, February 2009. 7, 87, 120

[28] A. Pricking. *Double Pionic Fusion to ^{4}He. Kinematically Complete Measurements over the Energy Region of the ABC Effect*. PhD thesis, University Tübingen, 2011. 9, 11, 12, 22, 26, 27, 43, 44, 46, 47, 85, 86, 89, 91, 92, 109

[29] P. Adlarson et al. **Abashian-Booth-Crowe resonance structure in the double pionic fusion to ^{4}He**. *Phys. Rev. C*, **86**:032201(R), September 2012. 11, 12, 87, 91

[30] S. Keleta et al. **Exclusive measurement of two-pion production in the $dd \to {}^4\mathrm{He}\pi\pi$ reaction**. *Nucl. Phys. A*, **825**:71–90, June 2009. 12

[31] Chr. Bargholtz et al. **The inclusive reaction $dd \to {}^4\mathrm{He} + X$ 29 MeV above the $2\pi^0$ threshold**. *Phys. Lett. B*, **398**:264–268, April 1997. 12

[32] K.R. Chapman et al. **Observation of the reaction $d + d \to 4He + 2\pi$ at 1.69 GeV/c**. *Phys. Lett.*, **21**:465–467, June 1966. 12

[33] J. L. Ping, H. X. Huang, H. R. Pang, and Fan Wang. **Quark models of dibaryon resonances in nucleon-nucleon scattering**. *Phys. Rev. C*, **79**:024001, February 2009. 11

[34] M. Bashkanov, Stanley J. Brodsky, and H. Clement. **Novel six-quark hidden–color dibaryon states in QCD**. *Phys. Letters B*, **727**:438442, December 2013. 11

[35] P. Adlarson et al. **Evidence for a New Resonance from Polarized Neutron-Proton Scattering**. *Phys. Rev. Lett.*, **112**:202301, May 2014. 11, 110

[36] C.Bargholtz et al. **The WASA Detector Facility at CELSIUS**. *Nucl. Inst. Meth.*, **A594**:339–350, September 2006. 13

[37] H. H. Adams et al. **Proposal for the Wide Angle Shower Apparatus (WASA) at COSY-Juelich - "WASA at COSY"**, November 2004. 13

[38] R. Maier. **Cooler synchrotron COSY - performance and perspectives**. *Nucl. Inst. Meth.*, **A390**:1–8, May 1997. 14, 15

[39] R. Maier et al. **Cooler synchrotron COSY**. *Nucl. Phy.*, **A626**:395c–403c, November 1997. 14

[40] D. Prasuhn et al. **Electron and stochastic cooling at COSY**. *Nucl. Inst. Meth.*, **A441**:167–174, February 2000. 14

[41] H. Stockhorst et al. **Compensation of Mean Energy Loss due to an Internal Target by Application of a Barrier Bucket and Stochastic Momentum Cooling at COSY**, February 2009. In *proceedings of COOL 2009, Lanzhou, China*. 14

[42] F.Bergman et al. **The WASA-at-COSY Pellet Target**, 2008. IKP/COSY Annual Report. 17

[43] T. Trostell. **Vacuum injection of hydrogen micro-sphere beams**. *Nucl. Inst. Meth.*, **A362**:41–52, August 1995. 17

[44] M. Jacewicz. *Measurement of the interaction pp* $\rightarrow$ $\pi^+\pi^-\pi^0$ *with CELSIUS/WASA*. PhD thesis, Uppsala University, 2004. 18, 19, 20

[45] I. Koch. *Multi pion production in Proton-Proton Collisions*. PhD thesis, Uppsala University, 2004. 20, 21

[46] M. Zieliński. *Feasibility study of the eta-prime* $\rightarrow$ *pi+ pi- pi0 decay using WASA-at-COSY apparatus*. Master's thesis, Jagiellonian University, 2008. 23, 27

[47] H. Calén et al. **Detector Setup for a Storage Ring with an Internal Target**. *Nucl. Inst. Meth.*, **A379**:57–75, April 1996. 23

[48] M. Dahmen et al. **A three layer circular scintillator hodoscope**. *Nucl. Instrum. Meth.*, **348**:97–104, August 1994. 24

[49] C. Pauly. *Light Meson Production in pp Reactions at CELSIUS/WASA above the* η *Threshold*. PhD thesis, University Hamburg, 2006. 25, 26

[50] W. Brodowski. *Design und Aufbau einer Vetowand für den WASA/PROMICE-Detektor am CELSIUS Speicherring und erste Messungen der Rektion pp* $\rightarrow$ *pp pi+ pi-*. Diplomarbeit, University Tübingen, 1995. 26, 27

[51] E. Pérez del Río. *Upgrade of the Forward Veto Hodoscopes at WASA*. Diplomarbeit, University Tübingen, 2010. 27, 28

[52] J. Zabierowski and J. Rachowsk. **The Light-Pulser Monitoring System for the WASA detector facility**. *Nucl. Inst. Meth.*, **A606**:411–418, May 2009. 28

[53] V. Hejny et al. **Performance issues of the new DAQ system for WASA at COSY**. *IEEE Trans. Nucl. Sci.*, **55**:261–264, February 2008. 28

[54] K. Zwoll et al. **Flexible data acquisition system for experiments at COSY**. *IEEE Trans. Nucl. Sci.*, **41**:37–44, 1994. 28

[55] C. F. Redmer. *In search of the Box-Anomaly with the WASA facility at COSY*. PhD thesis, University of Wuppertal, 2010. 29, 47

[56] Acam Messelectronic GMBH. *TDC-GPX Datasheet*, 2006. 30

[57] H. Kleines et al. **Development of a High Resolution TDC Module for the WASA Detector System Based on the GPX ASIC**. *EEE Nuclear Science Symposium Conference Record*, **2**:1005–1007, 2006. 30

[58] Acam Messelectronic GMBH. *TDC-F1 Functional description - scientic version.*, 2001. 30

[59] **PANDA Experiment will be one of the key experiments at the Facility for Antiproton and Ion Research (FAIR)**. 33

[60] M. Weigele. *Ein Cherenkov-Detektor für den Nachweis schnellester Teilchen*. Master's thesis, University Tübingen, 2012. 33, 38

[61] I. Tamm. **Radiation Emitted by Uniformly Moving Electrons**. *J. Phys. U.S.S.R*, **1**:439–454, 1939. 34

[62] K. Föhl. Private communication. 34, 40

[63] K. Föhl et al. **The WASA focussing light guide disc DIRC**. *JINST*, **7**:C01002, January 2012. 35, 36, 38

[64] P. Vlasov. *Analysis of the $\eta \to 3\pi^0$ decay in the pp interaction*. PhD thesis, Ruhr-Universität Bochum, 2008. 35

[65] A. Zink. **A DIRC demonstrator experiment at COSY**, December 2013. *31st CANU and 8th JCHP-FFE Workshop*. 40, 41

[66] A. Zink. **Thesis in preparation**. Erlangen University. 40

[67] V. Hejny, M. Hartmann, and A. Mussgiller. **RootSorter: A New Analysis Framework for ANKE**, 2002. IKP/COSY Annual Report Jül-4052. 46

[68] CERN. *Root*. 46

[69] A. Fridman. **The Deuteron as Target in High Energy Reactions**. *Fortschritte der Physik*, **23**:243–315, 1975. 56

[70] R. Machleidt. **High-precision, charge-dependent Bonn nucleon-nucleon potential**. *Phys. Rev. C*, **63**:024001, January 2001. 56

[71] S. Brandt. *Data Analysis*. Springer Verlag, 1999. 63

[72] A. Kupsc. **WASA note on Kinematical Fit.** 63, 68

[73] D. Coderre. *The Branching Ratio and CP-Violating Asymmetry of* $\eta \to \pi^+\pi^-e^+e^-$. PhD thesis, Ruhr-Universität Bochum Wortmarke, 2012. 69, 71

[74] P. Adlarson. *Studies of the Decay* $\eta \to \pi^+\pi^-\pi^0$ *with WASA-at-COSY*. PhD thesis, Uppsala University, 2012. 69

[75] C. Kerboul et al. **Deuteron tensor analysing power for the collinear** $\overrightarrow{d}\,p \to {}^3\mathrm{He}\pi^0$ **at intermediate energies.** *Physic Letters B*, **181**:28–32, November 1986. 75, 76, 77, 78, 79, 81, 89

[76] J. Banaigs et al. **A study of the reactions** $d+p \to \tau+\pi^0$ **and** $p+d \to \tau+\eta^0$. *Physic Letters B*, **45**:394–398, August 1973. 75, 76

[77] H. Clement and M. Bashkanov. **Model description of the** $pn \to R \to \Delta\Delta \to d\pi^0\pi^0$ **Reaction and its Confrontation with WASA-at-COSY Data**, 2010. Internal note. 85, 86, 109

[78] M. Bashkanov. *Double Pionic Fusion: Towards an Understanding of the ABC Puzzle by Exclusive Measurements*. PhD thesis, University Tübingen, 2006. 89, 91

[79] L. G. Dakhno et al. **Measurement of the cross sections for production of pion pairs in nucleon-nucleon collisions at energies below 1 GeV. Isospin analysis**. *Sov. J. Nucl. Phys.*, **37**:590, 1983. 119, 120

[80] J. Bystricky et al. **Energy dependence of nucleon-nucleon inelastic total cross-sections**. *J. Physique*, **48**:1901–1924, November 1987. 119, 120

Acknowledgements

First of all I would like to thank my supervisor, Prof. Dr. Heinz Clement. He gave me a great opportunity by allowing me to participate in this amazing group and by giving me the possibility of writing this thesis work. He has been not only my advisor but a friend and also of great support and help all these years. Thank you very much Heinz.

Also I would like to express my most sincere thanks to Prof. G. J. Wagner. For his help and suggestions, especially at the end stage of this work.

My colleagues from my group always will have a place in my heart. Mikhail Bashkanov, who has had the greatest patience of the world by listening to my never-ending doubts, programming problems and small talk in the many years we have shared the office. He has been a great friend and the best colleague I could have. Tatiana Skorodko, who has helped me through her experience and her invaluable friendship. Evgeny Doroshkevich, for his is the best "Good Morning" salute one can get in Tübingen. And Annette Pricking, a good friend, colleague and marvelous woman, always up for a tea, a discussion about data or a good talk about books and games. You all have made these years the best of my life.

Within the WASA collaboration, my special thanks go to Magnus Wolke, Frank Goldenbaum and Volker Hejny. I am not sure what I would have done if they weren't always ready to help, teach and also take me out during the experiments. I owe them for the interest they have always shown to help me out and give me advice when I needed it. Also many thanks to Pawel Moskal, always helpful, he allowed me to use part of the time dedicated to his own experiment to perform mine.

Anton Lymanets and Evgeny Lavrik, with whom I shared office and jokes. Christoph Sailer, to whom I will always be in doubt for being such an excellent friend. And of course, all the PhD students, professors and colleagues at the Physikalisches Institut. Thank you for the seminars, coffee breaks, talks and walks around the institute when the office grew too small.

Lena Heijkenskjöld, Farha Khan, Florian Bergmann, Kay Demmich and the whole WASA-troop. You make work even funnier than it already is. I cannot get you all here but I hope you understand how much I thank you for all the conversations, jokes, serious discussions about physics (sometimes) and support. Among you all, Lena and Farha you know you will always have my friendship and love.

To finish I would like to thank my family, who has been there for me, even when the distance was so big and the visits so scarce. Thank you for helping me, for your hope and for all your love.